

**Porous $La_xSr_{1-x}Co_yFe_{1-y}O_{3-\delta}$ – Molten
Alkali Metal Carbonate Membranes for CO₂
Permeation**

**Porous $La_xSr_{1-x}Co_yFe_{1-y}O_{3-\delta}$ – Molten
Alkali Metal Carbonate Membranes for CO_2
Permeation**



Hang Qi

A thesis submitted in partial fulfilment of the requirement
of Newcastle University for the degree of

Doctor of Philosophy

Research undertaken in the School of Chemical
Engineering and Advanced Materials
Newcastle University, Newcastle Upon Tyne, UK

May 2016

Abstract

Dual-phase ceramic molten carbonate membranes have the ability to permeate carbon dioxide at high temperatures, with or without oxygen. This project studied the novel process of oxygen-driven carbon dioxide permeation, based on the mechanism of carbon dioxide transportation within the molten carbonate phase. In this process, carbonate ions transported across the membrane in the molten phase are driven by the oxygen partial pressure gradient. In our study, the carbon dioxide can permeate through the membrane without its own partial pressure gradient; to achieve this, oxygen potential gradient against the carbon dioxide is required to overcome the carbon dioxide potential ($p'_{CO_2} \leq p''_{CO_2}$ and $p'_{O_2} > p''_{O_2}$). The carbon dioxide in p'_{CO_2} permeation to p''_{CO_2} is defined as the 'up-hill' permeation process.

This study shows extremely high carbon dioxide permeation with the permeance of the order of 10^{-6} mol m⁻² s⁻¹ Pa⁻¹ during up-hill experimentation, and, at this value of permeability, the order of magnitude for carbon dioxide separation is greater than for other membrane technologies in this field. The project also examined the stability of this dual-phase ceramic-carbonate membrane system consisting of La_{0.6}Sr_{0.4}Co_{0.2}Fe_{0.8} (LSCF) and a eutectic carbonate mixture (Li/Na/K) at about 600 °C. The results showed that this up-hill permeation operating over 200 hours occurred without a dramatic decrease in carbon dioxide permeation.

The most important advantage of this up-hill carbon dioxide separation is that there is no energy penalty during the carbon dioxide separation process. For the carbon dioxide removal process, the energy that the system required from the energy input to remove the carbon dioxide against its own chemical potential was the energy penalty for carbon dioxide separation. However, during carbon dioxide up-hill permeation, the oxygen provides a greater potential difference in the opposite direction to overcome that of the carbon dioxide during permeation. However, thermal energy for heating up the membrane is required; no energy is consumed continuously from the environment to maintain the up-hill permeation process at about 600 °C.

Table of Contents

List of Figures	IV
List of Tables	VIII
Nomenclature	IX
Acknowledgements	XII
Chapter 1 Introduction and aims	1
1.1 Research background.....	1
1.2 CO ₂ separation methods	3
1.3 Energy penalty in the CO ₂ separation process.....	7
1.4 up-hill CO ₂ permeation concept	10
1.5 Purpose of the study	13
1.6 Objectives and tasks	15
Chapter 2 Literature review	17
2.1 Introduction	17
2.2 Carbonate ceramic dual-phase membrane technology for CO ₂ separation.....	17
2.3 Thermodynamics of molten carbonates.....	20
2.3.1 Determining the decomposition rate	20
2.3.2 Thermal stability of alkali metal carbonates.....	22
2.3.3 Equilibrium CO ₂ partial pressure.....	23
2.3.4 Electrochemical stability of oxide species in molten alkali eutectic.....	28
2.3.5 Ternary molten alkali metal carbonates	31
2.4 Oxygen-permeable membranes	32
2.4.1 MIEC membranes.....	32
2.4.2 Perovskite-type LSCF system	35
2.5 Porous membrane fabrication	38
2.6 Membrane sealing at high temperatures	40
Chapter 3 Methodology	42
3.1 Experimental equipment	42
3.1.1 Reactor	42
3.1.2 Gas cylinders	43
3.1.3 Data analysis	43
Chapter 4 Membrane fabrication and characterisation	46

4.1 Introduction	46
4.2 Model for pore size estimation.....	46
4.2.1 Surface tension	46
4.2.2 Pore size estimation.....	47
4.3 Partially sintered membrane fabrication and characterisation.....	51
4.3.1 General preparation of porous host MIEC membranes	51
4.3.2 Carbonate salt infiltration	51
4.3.3 Characterisation of results and discussion	52
4.4 Fully sintered membrane fabrication and characterisation	56
4.4.1 Porous structure sintering and infiltration test	56
4.4.2 Carbon black and graphite	57
4.4.3 Cornstarch.....	58
4.4.4 Infiltration test and pore volume estimation	60
4.4.5 The typical LSCF membrane preparation and porosity used in the project	62
4.5 Conclusion.....	64
Chapter 5 High temperature sealing development.....	65
5.1 Introduction	65
5.2 Experiment 1: Glass-based sealant	66
5.2.1 Membrane preparation	66
5.2.2 Membrane sealing	67
5.2.3 Experimental setup	67
5.2.4 Results and discussion	67
5.2.5 Summary	70
5.3 Experiment 2: Ceramic sealant	71
5.3.1 Summary	74
5.4 Experiment 3: Silver paste sealant.....	74
5.4.1 Membrane fabrication	74
5.4.2 Membrane sealing	75
5.4.3 Experimental equipment	76
5.5 Results and discussion	76
5.6 Conclusion.....	80
Chapter 6 Kinetics and the limiting step for CO₂ permeation	82
6.1 Introduction	82
6.2 Experiment.....	84
6.2.1 Host membrane fabrication.....	84

6.2.2 Carbonate infiltration for sintered LSCF host membranes	84
6.2.3 Sealing of prepared membranes.....	84
6.2.4 Experimental setup and reactor system	85
6.3 Results analysis	87
Experiment 1: CO ₂ permeation as a function of O ₂ partial pressure in the feed side	87
Experiment 2: CO ₂ permeation as a function of CO ₂ partial pressure in the feed side	92
Experiment 3: Limiting step for CO ₂ permeation.....	97
6.4 Discussion.....	98
6.5 Conclusion.....	100
Chapter 7 Up-hill CO₂ permeation.....	102
7.1 Introduction	102
7.2 Experimental equipment	103
7.3 Results and discussion	105
7.3.1 CO ₂ permeation experiments	105
Experiment 1: CO ₂ up-hill permeation from 0.90% to 1.15% at 600°C	105
Experiment 2: 216-hour long-term CO ₂ up-hill permeation	108
Experiment 3: CO ₂ up-hill permeation from about 0.5% to 1% at 600°C.....	110
Experiment 3.1: CO ₂ up-hill permeation from 0.5% to 1% without symmetrical gas switching	112
Experiment 3.2L CO ₂ permeation without O ₂ in the feed side at 600°C	114
Experiment 3.3: O ₂ permeation without CO ₂ in the feed side at 600°C.....	116
7.3.2 Membrane characterisation	117
7.4 Conclusions	119
Chapter 8 Summary and future work	121
8.1 Conclusions and future work	121
8.1.1 Summary of the project	121
8.1.2 Achievement	123
8.1.3 Conclusions	124
8.1.4 Future work.....	125
References	127
Appendix A	132
Appendix B	134
Appendix C	141

List of Figures

Figure 1.1 Global fossil fuel and cement emissions: 9.7 ± 0.5 gigatonnes of carbon (GtC) in 2012, 58% over 1990; 9.9 ± 5 GtC in 2013, 61% over 1990 [5].....	1
Figure 1.2 Different sectors in total anthropogenic GHG emissions in 2004 (in terms of CO ₂ -eq) [10].....	2
Figure 1.3 Pulverised coal post-combustion CO ₂ capture.....	4
Figure 1.4 Gasification CO ₂ capture process.....	4
Figure 1.5 Oxy-fuel combustion process.....	5
Figure 1.6 Scheme for chemical-looping combustion; Me: metal; MeO: metal oxide as an oxygen carrier [17].....	6
Figure 1.7 Conceptual scheme of ceramic-molten carbonate dual-phase membrane consisting of porous solid oxide support and molten phase carbonates.	7
Figure 1.8 The process scheme of CO ₂ separation from flue gas using MEA solvent [22].	9
Figure 1.9 Scheme of CO ₂ permeation mechanism. CO ₂ can permeate across the membrane without chemical potential. Note: the CO ₂ mole fraction will be <1% in the feed side and > 1% in the permeate side during the permeation experiment.	12
Figure 1.10 Carbon dioxide up-hill permeation process with an oxygen removal step for a typical power plant at 1 atmosphere; the oxygen required in the feed side is supplied by air, and this oxygen will permeate with CO ₂ together to the permeate side and be removed by the O ₂ removal unit.....	13
Figure 2.1 Weight change of a carbonate mixture (60 wt% lithium carbonate and 40wt% potassium carbonate) up to the steady-state condition of 620 °C in a calcination furnace [37].....	23
Figure 2.2 Equilibrium CO ₂ partial pressure for potassium carbonate according to expression 2.20 (equilibrium line); Appendix B shows equilibrium CO ₂ for different carbonate eutectic mixtures.	25
Figure 2.3 Experimental reactor tube for heating potassium carbonate powder.	26
Figure 2.4 CO ₂ mol fraction from the outlet gas of the reactor as a function of time.....	28
Figure 2.5 Electrochemical stability range in molten Li ₂ CO ₃ -Na ₂ CO ₃ -K ₂ CO ₃ eutectic [40].	30
Figure 2.6 Schematic graph of oxygen transportation across an MIEC membrane by chemical potential drop [54, 55].	33
Figure 2.7 Crystal structure of an ideal ABO ₃ perovskite oxide [59].....	34
Figure 2.8 Relative weight change of LSCF sample as a function of Sr content (moles) and temperatures under oxygen [73].	36
Figure 2.9 Electrical conductivity of $La_{0.6}Sr_{0.4} - zCo_{0.2}Fe_{0.8}O_{3-\delta}$ measured in air [72]. ...	38
Figure 2.10 Schematic of the sealing of a typical membrane on a ceramic support [26].	40
Figure 3.1 Permeation cell apparatus comprising a gas supply and feed control, membrane module, and furnace.	44
Figure 4.1 External pressure on the curved surface of a liquid. (a) Equilibrium state; (b) cooperating force towards the liquid (downward); (c) cooperating force towards the air (upward) [95].....	48
Figure 4.2 Supplementary pressure from a curved surface	49
Figure 4.3 Height of a liquid column under supplementary pressure. (a) Liquid column tends to go up; (b) liquid column tends to go down.....	50
Figure 4.4 Scheme of a porous membrane with a continuous molten carbonate phase.	51
Figure 4.5 SEM images of fresh porous membrane substrates sintered at 900 °C. (a) Surface an LSCF2882 membrane; (b) surface of an LSCF6482 membrane.	52
Figure 4.6 EDS analysis of carbonates (Li, Na, K in a 42.5:32.5:25 mol ratio) – infiltration on the surface of an LSCF membrane; molten carbonates infiltrated at 520 °C. (a) LSCF 2882 membrane; (b) LSCF 6428 membrane.	54

Figure 4.7 SEM images of LSCF2882 membranes on the surface of molten carbonates' (Li, Na, K in a 42.5:32.5:25 mol ratio) infiltration side. (a) 520 °C carbonate infiltration; (b) 600 °C carbonate infiltration; (c) 700 °C carbonate infiltration; (d) 800 °C carbonate infiltration.	55
Figure 4.8 EDS analysis of a cross section of carbonate-infiltrated LSCF2882 membrane. (a) 700 °C infiltration; (b) 800 °C infiltration.	56
Figure 4.9 SEM images of pore former particles: (a) carbon black; (b) graphite.	57
Figure 4.10 SEM images of sintered LSCF6428 membranes fabricated from mixing with pore formers. (a) Cross section of the membrane formed by using carbon black; (b) cross section of the membrane formed by using graphite.	58
Figure 4.11 SEM images of cornstarch particles.	59
Figure 4.12 SEM results for an LSCF6428 membrane sintered by mixing with cornstarch. (a) Surface area of the membrane; (b) cross section of the membrane.	59
Figure 4.13 Pore volume estimation according to water intrusion for carbon black applied to an LSCF6428 membrane.	61
Figure 4.14 Cumulative porosity as a function of pore size. The mean pore diameter is 667 nm and the corrected porosity is 47.8%. The raw data for Hg injection are presented in Appendix C with parameters.	63
Figure 5.1 Conceptual schematic of the ion-conducting dual-phase membrane.	66
Figure 5.2 Sealing of a dual-phase membrane with a combination of silver and glass-based materials.	67
Figure 5.3 (a) Flux of CO ₂ and leaking N ₂ in the permeate side of the membrane at 850 ° and 780 °C. 50% CO ₂ and 50% N ₂ at 1 atmosphere are provided in the feed side of the membrane at a total inlet flow rate of 10 ml (STP) min ⁻¹ ; (b) the resultant leakage-subtracted CO ₂ permeability.	68
Figure 5.4 CO ₂ permeation over 50 hours. (a) Flux of CO ₂ and leaking N ₂ in the permeate side of membrane at 800 °C; (b) the resultant leak-subtracted CO ₂ permeability.	69
Figure 5.5 (a) Flux of CO ₂ and leaking N ₂ ; (b) the resultant leak-subtracted CO ₂ permeability.	70
Figure 5.6 (a) CO ₂ and N ₂ mole fraction from the downstream side of the membrane according to the temperature; (b) CO ₂ permeation apart from N ₂ leak CO ₂ flow.	72
Figure 5.7 CO ₂ and N ₂ mol fractions from the downstream side of the membrane according to the temperature. (a) Blank test with a dense LSCF2882 membrane; (b), (c), and (d) are CO ₂ permeation results; also indicated is the N ₂ leakage.	74
Figure 5.8 Schematic diagram of a membrane sealing system that includes spring and hook to apply pressure on the silver paste below the membrane; the silver paste was dried in air before pressure was applied.	75
Figure 5.9 The scheme of a membrane sealing system that includes a heavy tube with a semi-closed end to press the membrane.	76
Figure 5.10 Sealing effect of silver paste without a press device.	78
Figure 5.11 Time dependence of permeate carbon dioxide after subtracting leaks.	78
Figure 5.12 Sealing effect using silver paste with a press device.	80
Figure 6.1 Schematic mechanism of ion-conducting (a) and electron-conducting (b) dual-phase membranes for CO ₂ separation.	83
Figure 6.2 Scheme of the membrane reactor setup for the kinetic experiment.	87
Figure 6.3 Mole fraction of N ₂ , CO ₂ , and O ₂ in the permeate side of the membrane. Period a, b, c, d, e, and f correspond to 2%, 4%, 6%, 8%, 10%, and 12% oxygen put into the feed side of the reactor, while the carbon dioxide stayed at 20%.	89
Figure 6.4 The CO ₂ mole fraction in the permeate side corresponds to the O ₂ partial pressure increase in the feed side; 20% CO ₂ is provided in the feed side. The x-axis is the oxygen partial pressure gradient, which is equal to ΔPO_2 ; the y-axis is the permeate (leakage subtracted) CO ₂ mole fraction in the permeate side ($\pm 5\%$ error).	91

Figure 6.5 The ratio of CO ₂ /O ₂ in the permeate side of the membrane from Fig. 6.3; 2% oxygen was introduced to the feed side of the membrane and followed by 4%, 6%, 8%, 10%, and 12% oxygen fed into the feed side of the membrane.	92
Figure 6.6 Mole fractions of N ₂ , CO ₂ , and O ₂ in the permeate side of the membrane.	93
Figure 6.7 Leak-corrected CO ₂ and O ₂ mole fractions in the permeate side of the membrane as the feed CO ₂ decreased from 40% to 5%; time periods a, b, c, d, and e correspond to 40%, 30%, 20%, 10%, and 5% carbon dioxide, respectively, going to the feed side of the membrane with 4% oxygen.	95
Figure 6.8 The CO ₂ mole fraction in the permeate side corresponding to the CO ₂ mole fraction in the feed side; refer to Fig. 6.7 ($\pm 3\%$ error).....	96
Figure 6.9 Ratio of CO ₂ /O ₂ in the permeate side of the membrane when the CO ₂ mole fraction in the feed side changed following Fig. 6.6.	97
Figure 6.10 CO ₂ mole fraction in the permeate side of the membrane with different O ₂ partial pressures in the feed side and the CO ₂ mole fraction in the permeate side with helium replacing O ₂ in the feed side; ■ indicates the permeated CO ₂ ($\pm 7\%$ error) when CO ₂ in the feed side was diluted by O ₂ ; □ indicates the permeated CO ₂ ($\pm 12\%$ error) when CO ₂ in the feed side was diluted by helium.	98
Figure 6.11 The mechanism of CO ₂ and O ₂ co-permeation at 890 °C; the O ₂ in the feed side was found to have the ability to accelerate the CO ₂ permeation rate.	99
Figure 6.12 The mechanism of CO ₂ and O ₂ co-permeation at 600 °C.	100
Figure 7.1 Schematic of the high-temperature CO ₂ permeation setup.	104
Figure 7.2 Mole fractions of gases in both the feed-side and permeate-side outlets for experiment 1. During asymmetrical operation: feed-side inlet: 0.99% CO ₂ /1.03% N ₂ /19.45% O ₂ in Ar, permeate-side inlet: 1.03% CO ₂ in Ar. During symmetrical operation: feed- and permeate-side inlets: 1.03% CO ₂ in Ar. Note that the value for the oxygen mole fraction in the feed-side outlet during asymmetric operation is off scale.	106
Figure 7.3 Mole fractions of gases in both feed-side and permeate-side outlets for experiment 2. (a) During asymmetrical operation: feed-side inlet: 0.99% CO ₂ /1.03% N ₂ /19.45% O ₂ in Ar, permeate-side inlet: 1.03% CO ₂ in Ar. During symmetrical operation: feed- and permeate-side inlets: 1.03% CO ₂ in Ar. A flux of $1.8 \pm 0.3 \times 10^{-4}$ mol m ⁻² s ⁻¹ was determined at time t ₃ . (b) Uphill permeation performed over 216 hours (different timescale used) during asymmetrical operation with no apparent drop in flux or appearance of a trans-membrane leak and (c) return to symmetrical operation. (The value for the oxygen mole fraction in the feed-side outlet during asymmetric operation is off scale).	109
Figure 7.4 Mole fractions of gases in both feed- and permeate-side outlets for experiment 3. During symmetrical operation: feed- and permeate-side inlets: 1.03% CO ₂ in Ar. During asymmetrical operation: feed-side inlet: 0.51% CO ₂ /0.57% N ₂ /19.5% O ₂ in Ar, permeate-side inlet: 1.03% CO ₂ in Ar. A flux of $1.5 \pm 0.3 \times 10^{-4}$ mol m ⁻² s ⁻¹ was determined at time t ₄ . Note that the value for the oxygen mole fraction in the feed-side outlet during asymmetric operation is off scale.	112
Figure 7.5 Mole fractions of gases in both feed- and permeate-side outlets for experiment 3.1. Feed-side inlet: 0.54% CO ₂ /0.56% N ₂ /19.5% O ₂ in Ar, permeate-side inlet: 1.04% CO ₂ in Ar. A flux of $1.4 \pm 0.3 \times 10^{-4}$ mol m ⁻² s ⁻¹ was determined after 10 hours.	114
Figure 7.6 Mole fractions of gases in both feed- and permeate-side outlets for experiment 3.2. During symmetrical operation: feed- and permeate-side: 1.03% CO ₂ in Ar. During asymmetrical operation: feed-side inlet: 1.03% CO ₂ in Ar, permeate-side inlet: approximately 0.6% CO ₂ in Ar	115
Figure 7.7 Mole fractions of gases in both feed- and permeate-side outlets for experiment 3.3. During symmetrical operation: feed- and permeate-side: 1.03% CO ₂ in Ar. During asymmetrical operation: feed-side inlet: 20% O ₂ in Ar, permeate-side inlet: pure Ar. There is a break in the scale of the y-axis for the feed-side graph.	116

Figure 7.8 SEM micrographs of the external surfaces of an LSCF6428 membrane (a) before infiltration with molten carbonate; (b) after infiltration with molten carbonate; and (c) after permeation for 216 h	118
Figure 7.9 XRD diffractograms of the fresh and used membranes. Both diffractograms show a fully developed perovskite-like structure (indicated by ●) and peaks indicative of molten carbonate (indicated by ○). Some additional peaks may be due to the formation of interfacial species (indicated by +).....	119
Figure 7.10 Carbon dioxide permeances as a function of temperature from references. Only the best-performing system is shown.	120
Figure 8.1 The driving force of up-hill CO₂ permeation, chemical potential gradient.	123

List of Tables

Table 2.1 Molar ratios of oxide, peroxide, and superoxide ions in alkali molten carbonates initially contain 3 mole percent oxide ions under pressure of $P(O_2) = 1$ atm [40].....	30
Table 2.2 <i>pKd</i> * values for each molten alkali metal carbonate at different temperatures [43].....	32
Table 2.3 Oxygen content (moles) of LSCF compositions under various conditions [74].....	37
Table 4.1 LSCF6428 membrane with cornstarch applied; green: 2.188 g, sintered: 1.624 g	61
Table 4.2 YSZ membrane with cornstarch applied; green: 2.400 g, sintered: 1.594 g	61
Table 4.3 Hg intrusion data for LSCF6428; refer to Fig. 4.10(b) [using graphite powder (Fig. 4.9(b)) as a pore former for comparison].....	63

Nomenclature

atm	Atmosphere
A_s	Surface area
$a(i)$	Activity of i
CCS	Carbon capture and storage
CLC	Chemical-looping combustion
CO_3^{2-}	Carbonate ion
CSTF	$Ca_{0.8}Sr_{0.2}Ti_{0.7}Fe_{0.3}O_{3-\delta}$
DEA	Diethanolamine
E_a	The primary energy required to separate CO_2 from the flue gas
E_{K_2O}	Activity of K_2O
EDS	Energy-dispersive X-ray spectroscopy
e^-	Electron
$f(CO_2)$	Flux of carbon dioxide ($mol\ min^{-1}$)
f_1	Energy penalty
FTM	Facilitated transport membrane
GHGs	Greenhouse gases
GtC	Gigatonnes of carbon
GDC	Gadolinia doped ceria (GDC; Gd_2O_3 doped CeO_2)
HFCs	Hydrofluorocarbons
$h\cdot$	Electron holes
IPCC	Intergovernmental Panel on Climate Change
IC	Ion-conductive
K^*	Equilibrium constant
K	Absolute temperature
LSCF2882	$La_{0.2}Sr_{0.8}Co_{0.8}Fe_{0.2}O_{3-\delta}$
LSCF6428	$La_{0.6}Sr_{0.4}Co_{0.2}Fe_{0.8}O_{3-\delta}$
MCFCs	Molten carbonate fuel cells

MCOC	Mixed conducting oxide ceramic
Me	Metal
MeO	Metal oxide
MEA	Monoethanolamine
MIEC	Mixed ionic-electronic conducting
MR	Membrane reactor
MWh	Megawatt hour
MSP	Mass spectrometer
$MW(N_2)$	Molecular weight of N_2
m	Weight of sample
O^{2-}	Oxygen ion
O_O^x	Oxygen ion on lattice site, ^x : uncharged
P_{atm}	One atmosphere pressure
P_{CO_2}	Partial pressure of carbon dioxide
ΔP_{CO_2}	Partial gradient of CO_2
PFCs	Perfluorocarbons
PVA	Poly (vinyl alcohol)
PMMA	Polymethylmethacrylate
P_s	Supplementary pressure
Q_{N_2}	Volumetric flow
R_u	Universal gas constant
SOFCs	Solid oxide fuel cells
SF_6	Sulphurhexafluoride
SDC	Samarium-doped ceria
SNDC	Sm^{3+} and Nd^{3+} co-doped ceria
STP	Standard temperature and pressure
T	Temperature
T_c	Critical temperature
μ'_{O_2}	Chemical potential of O_2 in the feed side
V_O''	Oxygen vacancy
V_m	Molecular volume
W_a	Primary work required to separate CO_2
W_c	The output of a power plant

YSZ	Ytria stabilised zirconia $(\text{ZrO}_2)_{0.92}(\text{Y}_2\text{O}_3)_{0.08}$
η_{ideal}	Product of the ideal heat to work conversion efficiency
σ_s	Surface tension
χ	Weight change

Acknowledgements

I would like to thank my supervisor, Prof. Ian Metcalfe, for the precious opportunity to work on this project and for the patient guidance, encouragement, and advice he has provided throughout the last four years of my studies. I also thank my co-supervisor, Dr Evangelos Papaioannou, for his suggestions and guidance on my experimental work in chapter 7.

I thank Dr Alan Thursfield with help in setting up my preliminary experiments in my first- and second-year studies. I thank Jianwei Lu for operating the membrane system during the 216-hour experiment. I thank Dr Zhentao Wu and Professor Kang Li of Imperial College for the BET analysis and Dr Dragos Neagu and Professor John Irvine of St Andrews University for the SEM analysis. The research leading to the results has received funding from the European Research Council under the European Union's Seventh Framework Programme (FP/2007-2013)/ERC Grant Agreement Number 320725 and from the EPSRC via a PLATFORM Grant, EP/G012865/1.

Author contributions to a published paper in the *Journal of Membrane Science*:

'Uphill' permeation of carbon dioxide across a composite molten salt-ceramic membrane
Professor Ian Metcalfe secured the funding, generated the conceptual ideas, and wrote the paper. Dr Evangelos Papaioannou was responsible for the laboratory work. Hang Qi performed the laboratory work.

Note: Jianwei Lu was taught by Hang Qi to operate the 216-hour experiment.

Chapter 1 Introduction and aims

1.1 Research background

Carbon dioxide (CO₂) is the most widely produced flue gas from coal-fired power plant and gas plant combustion processes. It was listed as a greenhouse gas (GHG) in the Kyoto Protocol in 1998, the others being methane (CH₄), nitrous oxide (N₂O), hydrofluorocarbons (HFCs), perfluorocarbons (PFCs), and sulfurhexafluoride(SF₆) [1]. Carbon dioxide itself may not be the greenhouse gas that has the most serious impact on global warming and climate change, bringing a series of disasters to human society; nevertheless, there is no doubt that carbon dioxide is the most important greenhouse gas nowadays, and it is increasingly so because of the huge amount (9.7 gigatonnes in 2012) of carbon dioxide emissions every year, mostly from the combustion of fossil fuels [2, 3]. In America, energy-related carbon dioxide emissions constituted 81.5% of total greenhouse gas emissions by 2009. In other words, carbon dioxide (energy-related) emission contributes the most to greenhouse gas emissions in America [4]. Recent global carbon dioxide emissions caused by fossil fuel combustion are estimated to have reached 36 billion tonnes in 2013 (about 9.8 billion tonnes of carbon), 61% higher than emissions in 1990 (Fig. 1.1) [5].

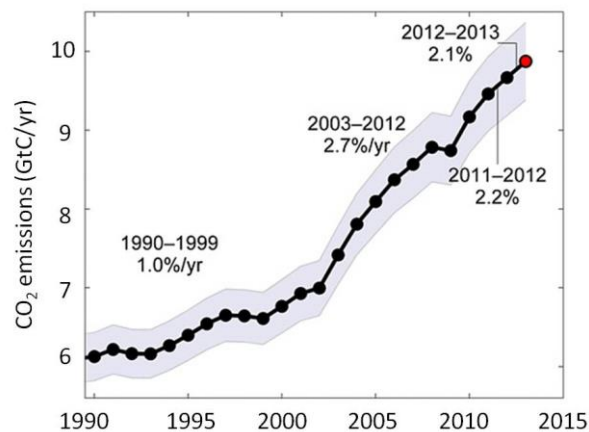


Figure 1.1 Global fossil fuel and cement emissions: 9.7 ± 0.5 gigatonnes of carbon (GtC) in 2012, 58% over 1990; 9.9 ± 0.5 GtC in 2013, 61% over 1990 [5].

Earlier research has shown that the carbon dioxide emitted into the atmosphere will take centuries to be removed or absorbed naturally into the earth, by either photosynthesis or weathering of rocks [6]. In fact, if there is not a major reduction in carbon dioxide emissions in the near future, the risk will be greater that greenhouse gas emissions will

Chapter 1. Introduction and aims

exceed the capacity that the nature can afford, causing serious climate change. As the carbon dioxide accumulated in the atmosphere shortly will be incapable of being absorbed by the earth, this will result in a dramatic growth of carbon dioxide concentration in the air. Previous research has shown that, when three to five gigatonnes of carbon dioxide are emitted into the atmosphere, it leads to a 1 ppm increase in the carbon dioxide concentration in the atmosphere [7]. The Intergovernmental Panel on Climate Change (IPCC) pointed out that an increase in temperature of 2-3 °C is dangerous for the environment, while paleo climate data showed that doubling carbon dioxide concentrations in the atmosphere results in a 3°C climate sensitivity [8, 9].

Fig. 1.2 shows that the main source of carbon dioxide emissions is energy-supplying processes, which contribute 26% of the total carbon dioxide emissions, more than emissions from industry (19%), and forestry (17%), agriculture (14%), transport (13%), residential and commercial buildings (8%), and waste (3%) [10]. The carbon dioxide emission from the energy supply sector refers particularly to fossil fuel combustion power plants, including coal, natural gas, and oil for electricity generation and supply. In particular, coal-fired power plants are relatively low cost compared to gas and oil. In America, about 50% of electricity is supplied by coal-fired power plants, which contribute 40% to the total carbon dioxide emissions per year [3].

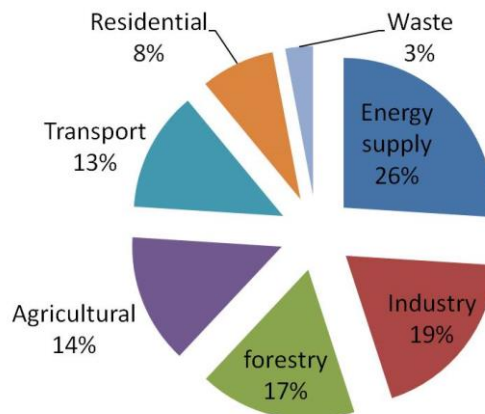


Figure 1.2 Different sectors in total anthropogenic GHG emissions in 2004 (in terms of CO₂-eq) [10].

Typically, 800 to 900 kilograms of carbon dioxide (about 13% CO₂ in hot flue gas) can be produced from a coal-fired power plant for one MWh of electricity generation, while that generated from natural gas can produce 350 to 400 kilograms of carbon dioxide [11, 12]. To reduce carbon dioxide emissions in energy-related processes, especially in coal combustion power plants, many newly designed power plants and renewable energy

have been developed; however, none of these new technologies can replace the traditional power plant that uses fossil fuels and some of them are still in the preliminary stage [3].

1.2 CO₂ separation methods

The existing methods for carbon dioxide removal are based on the following three principles:

- a) Post-combustion removal: CO₂ separation from flue gases after combustion;
- b) Pre-combustion removal: removal of CO₂ from fuel processes, including CO conversion of synthesis gas and removal of CO₂ from H₂ fuels;
- c) Collection of CO₂ from highly concentrated exhaust gases (e.g., oxy-fuel combustion).

The schematic diagrams in Fig. 1.3, 1.4, and 1.5 show these methods of carbon dioxide capture and storage in fossil fuel power plants.

Post-combustion CO₂ capture is the process of separating CO₂ from flue gas containing NO_x and SO_x; Fig. 1.3 shows the process flow diagram. There are two main methods; one is to use chemical absorption, typically monoethanolamine (MEA), and the other uses membrane technology. The chemical absorption method has been used widely since the 1940s and it can produce high-purity CO₂ streams; however, the costs of regenerating the absorber are relatively high, comprising about 10% of the energy produced by the plant [13]. In post-combustion processes such as polymer membrane technologies, the carbon dioxide is diluted in the flue gas and produced at low CO₂ partial pressures (10% mole fraction), which is applicable for most existing coal-fired power plants, but high pressure is required to obtain rich carbon dioxide, and this consumes extra energy.

Post-combustion CO₂ removal

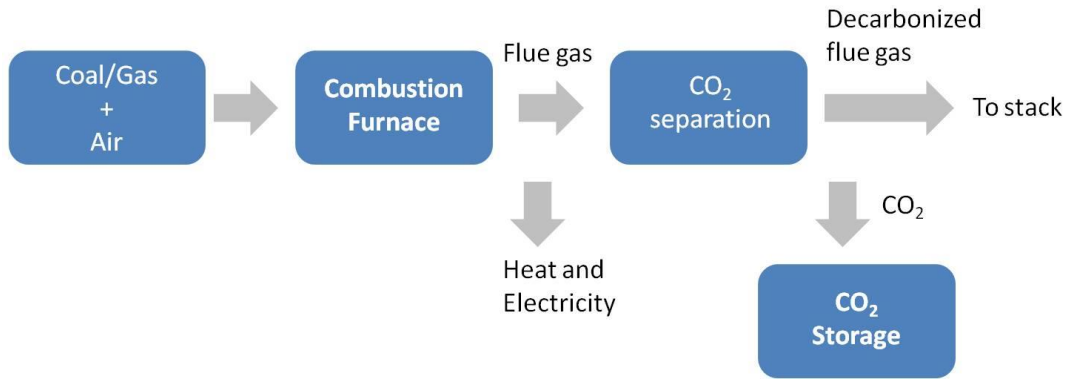


Figure 1.3 Pulverised coal post-combustion CO₂ capture.

Pre-combustion CO₂ capture is also called gasification CO₂ separation; the fuels are converted to a mixture of CO and H₂ by reforming (if natural gas is used as the fuel) or a gasification process (if coal is used as the fuel), followed by a water-shift reaction. CO₂ is separated from conversion products and H₂ is burned out in a gas turbine or gas prospectively. In this way, the carbon dioxide can be removed from the fuel before going to the combustion process, and high pressure also needs to be supplied to increase the driving force for separation. One leading option for CO₂ separation in this stage is the solvent MEA absorption process. However, only a few gasification power plants are currently operating, and the cost of extensive equipment and systems are significant [14]. Fig. 1.4 shows the process flow diagram.

Pre-combustion CO₂ removal

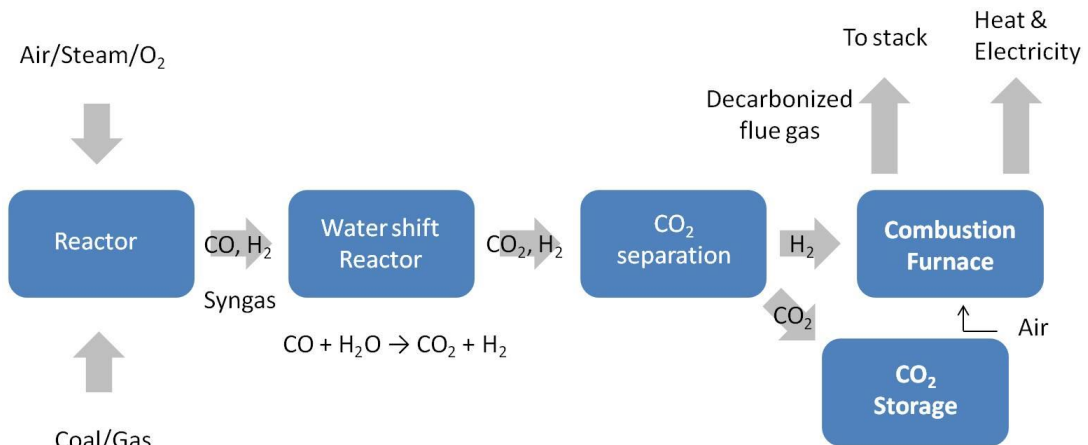


Figure 1.4 Gasification CO₂ capture process.

In the oxy-fuel combustion process (Fig. 1.5), oxygen is separated from air, brought to the energy conversion unit, and mixed with partially recycled flue gas (concentrated CO₂). The combustion occurs in the atmosphere mixture of CO₂/O₂ in such a way that

the exhaust gases are high-purity CO₂ streams [15]. After the SO₂ removal steps, the CO₂ volume fraction in the exhaust gas can reach 90% on a dry basis. The CO₂ can then go directly to storage and no further process is needed. However, this technology is high in capital costs for both operation and maintenance; in particular, the oxygen separation plant costs about 23% to 37% of the total plant energy output [16].

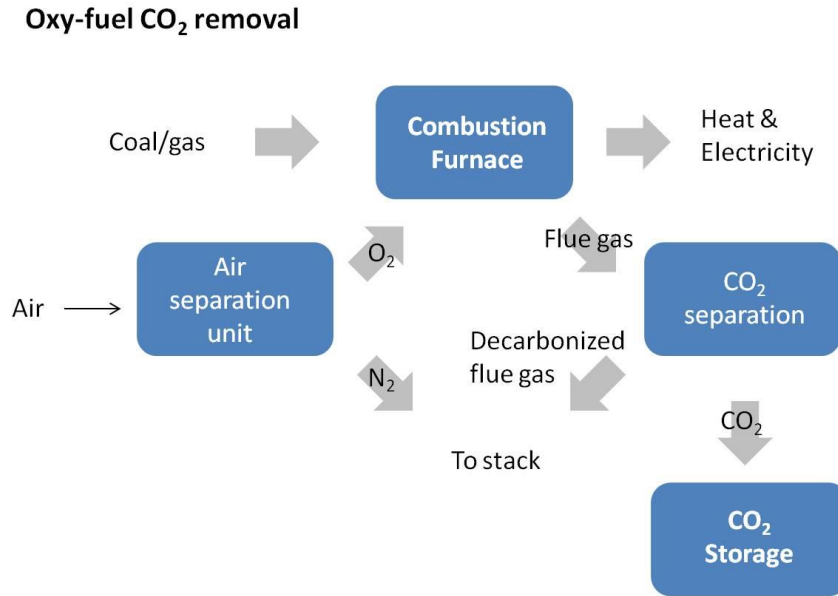
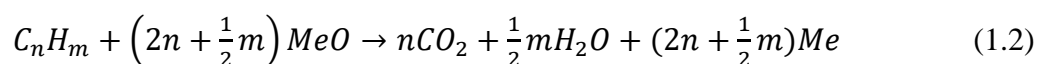


Figure 1.5 Oxy-fuel combustion process.

There is another method called chemical-looping combustion (CLC), which is also referred to as unmixed combustion because there is no direct contact between fuels and air, which can be applied for most combustion processes with air. CLC is a method of carbon capture, as the oxygen carrier is used to capture oxygen from the air and bring it to the fuels in such a way that nitrogen and other gases in the air will not be oxidised, and this reduces pollutant emission. Rich CO₂ and water can be collected after combustion. Oxygen carriers are small particles made from various metal oxides, such as Fe₂O₃, NiO, CuO, or Mn₂O₃.

A simple scheme for a CLC system is presented in Fig. 1.6; there are two reactors in the system, one for metal oxidation by air and the other for fuel combustion. The oxygen carriers can be circulated between the two reactors and oxidised in the air reactor, based on reaction 1.1 below, and the metal oxides are reduced by fuel in the fuel reactor, based on reaction 1.2 [17].



Chapter 1. Introduction and aims

The advantage of the CLC process is mainly a reduction in the emissions of NO_x ; a well-designed CLC system could avoid the formation of NO_x at mid-range temperatures (500-600°C) when the regeneration of the oxygen carrier occurs without a flame (a flame helps NO_x formation). The exhaust gases from the CLC system are CO_2 and H_2O , and CO_2 can be simply separated by a condenser.

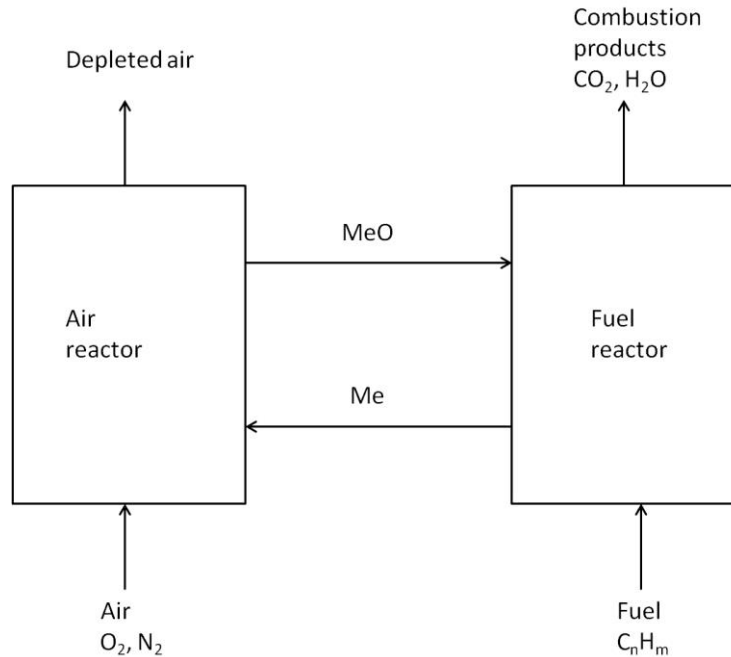


Figure 1.6 Scheme for chemical-looping combustion; Me: metal; MeO: metal oxide as an oxygen carrier [17].

In this project, a novel post-combustion membrane technology is introduced for CO_2 separation; there is a perm-selective (at 800 to 900°C) dual-phase membrane, which has drawn attention in recent years and can collect carbon dioxide continuously at steady-state operation at high temperatures with lower energy requirements compared to the oxy-fuel and pre-combustion method [18, 19]. This membrane can also be used as a membrane reactor for reactions involving carbon dioxide, e.g., a dual-phase tube-shell membrane reactor (MR) for a carbon dioxide-methane reforming reaction with carbon dioxide separation [20].

The concept of this new membrane was originally derived from the molten-carbonate fuel cells (MCFCs) and oxygen-permeable mixed ion-electron conducting membranes (MIEC). It consists of a eutectic mixture of alkali metal salt as a molten phase and a porous ion-conductive (IC) or mixed ion-electron conductive (MIEC) ceramic substrate as a solid phase, each phase having different functions. The molten carbonates, as a liquid phase at high temperatures, provide a path for carbonate ion (CO_3^{2-})

transportation across the membrane continuously, releasing gaseous carbon dioxide on the other side of the membrane. The porous substrate synthesised from solid oxide comprises ion-conducting or mixed ion-electron-conducting materials and can provide mobile oxygen solvated within the oxygen sub-lattice ($V_O^{\prime\prime}$), allowing the feed carbon dioxide to combine with structural oxygen (O^{2-}) to form carbonate ion (CO_3^{2-}) in the molten carbonate. A schematic graph shown in Fig. 1.7 illustrates the concept of this dual-phase membrane and the process of carbon dioxide separation. The dual-phase membrane concept introduced here is the system that was used in this project for CO_2 permeation experiments.

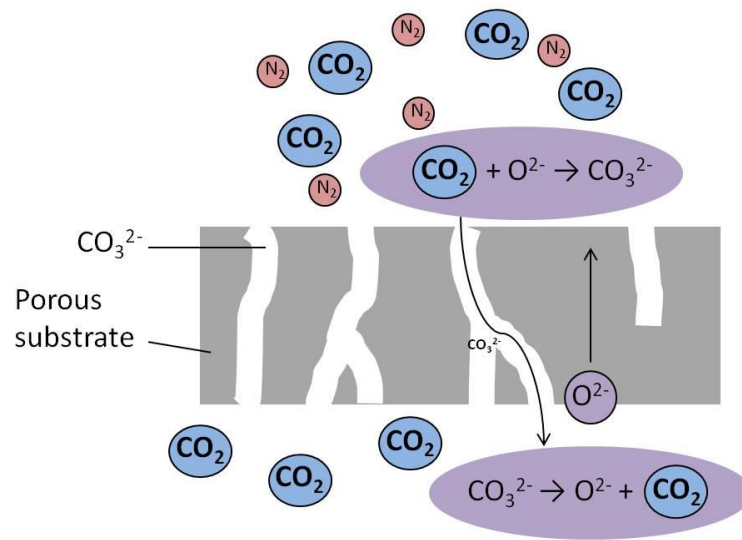


Figure 1.7 Conceptual scheme of ceramic-molten carbonate dual-phase membrane consisting of porous solid oxide support and molten phase carbonates.

1.3 Energy penalty in the CO_2 separation process

The energy penalty in the carbon capture and storage (CCS) process can be defined as part of the fuel that must be dedicated to CCS processes to maintain the amount of work output or the loss of output for constant fuel input. For coal-fired power plants, which contribute the most CO_2 emissions, there is a significant benefit to reducing the energy penalty for saving energy and improving the output efficiency.

Several typical chemical engineering methods can be used in a coal-fired power plant for carbon dioxide capture and storage. One of the comprehensively used technologies is chemical absorption, which is a promising technology that has already been commercialised in many industries, including food production, chemical processing, and ammonia production. However, the high regeneration energy needs to be

Chapter 1. Introduction and aims

considered. For example, regenerating a scrubbing solvent and extra high energy was consumed. The energy penalty for a conventional solvent scrubbing process is about 22% to 29%, which is considered a large value compared to the facilitated membrane technology with its 12.2% energy penalty [21]. Many people have tried to reduce the energy penalty by increasing the available waste heat from the CCS process that can be recovered for use under the second law of thermodynamics separation efficiency.

An example of a well-developed technology for post-combustion CO₂ separation from power plant flue gas is using solvent monothenolamine (MEA) for CO₂ absorption. In the separation system, also called the temperature swing system, as Fig. 1.8 shows, the primary energy required to separate CO₂ from flue gas is E_a . The value of E_a does not equal the enthalpy of desorption because the same amount of heat is generated from exothermic absorption as endothermic desorption. According to the second law of thermodynamics, which limits the efficiency of any heat to work conversion, E_a is determined by W_a (the primary work required to separate CO₂) over the product of the ideal heat to work conversion efficiency (η_{ideal}) and the second law efficiency of the actual separation process (η_{2nd}) [22].

$$E_a = \frac{W_a}{\eta_{ideal} \eta_{2nd}} \quad (1.3)$$

The ideal separation efficiency η_{ideal} for temperature swing separation can be expressed as follows:

$$\eta_{ideal} = 1 - \frac{T_a}{T_s} \quad (1.4)$$

As MEA always works at a low temperature at T_a (about 310 K), the amount of waste heat produced from the CO₂ absorption process can be used together with additional heat T_H , then the primary energy required from additional fuel combustion $E_{(sep)}$ can be expressed as follows:

$$E_{sep} = \frac{W_a}{\eta_{ideal} \eta_{2nd}} - E_w \quad (1.5)$$

E_w is the available waste heat that can be calculated considering the Carnot efficiency of the power plant:

$$\eta_c = 1 - \frac{T_L}{T_H} \quad (1.6)$$

Chapter 1. Introduction and aims

The efficiency of power plant is as follows:

$$\eta_{pp} = 1 - \frac{E_L + E_w'}{E_H} \quad (1.7)$$

where E_w' is the total waste heat from the irreversible process and E_H is the primary energy of the fuel.

According to its definition, energy penalty f_1 can be expressed as follows:

$$f_1 = \frac{E_S}{E_H} \quad (1.8)$$

Assuming that the amount of fuel is constant, the energy penalty is equal to the reduction of the power plant output. The output of power plant will be as follows:

$$W_c = \eta_{pp} E_H (1 - f_1) \quad (1.9)$$

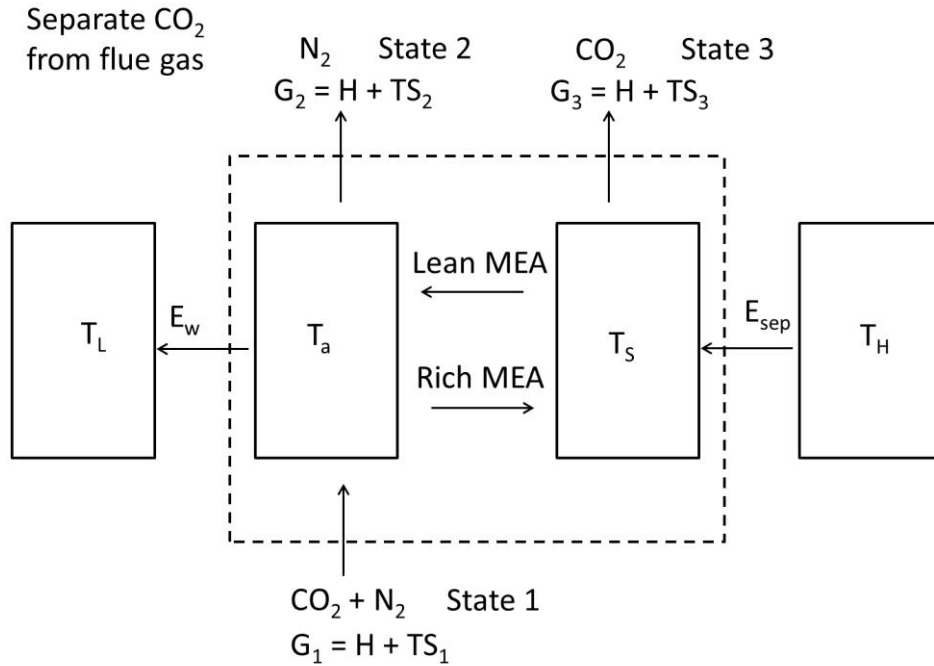


Figure 1.8 The process scheme of CO₂ separation from flue gas using MEA solvent [22].

Dual-phase ceramic-carbonate membrane systems have been reported to exhibit successful carbon dioxide removal application [23], using the carbon dioxide partial pressure gradient as the driving force to separate carbon dioxide from a highly concentrated side to a low-carbon dioxide partial pressure side. However, this membrane technology requires a certain carbon dioxide partial difference (more than 10%

difference) between the feed side and the permeate side of the membrane to provide the driving force to permeate carbon dioxide as ‘down-hill’ permeation according to the carbonate transportation mechanism in dual-phase membranes (Fig. 1.7). This means that membrane technology must solve the thermodynamic problem of separating and removing the carbon dioxide from a low concentration to a highly rich carbon dioxide environment, with equal pressure on both sides of the membrane. To achieve this, extra energy input is required to overcome the partial pressure gradient that is opposite to down-hill CO₂ permeation, such as pressurised feed-side gas, to obtain a high concentration of carbon dioxide in the permeate side if conventional polymer membrane technology was used, and the gases from the permeate side also need pressurisation to obtain equal pressure. The energy that the system requires from energy input to remove the carbon dioxide against its own chemical potential gradient is the energy penalty for carbon dioxide separation. For example, the flue gas from a typical coal-fired power plant contains about 10% to 13% carbon dioxide; if a polymeric membrane is applied, a certain amount of energy input (usually pressurising the gas in the feed side) must be consumed to collect higher concentrated carbon dioxide in the permeate side for storage. Accordingly, the efficiency of the energy output from the power plant will be lower than it would be otherwise.

Based on the current technology, it is difficult but very important to reduce the energy penalty for carbon dioxide enrichment from flue gas and increase the energy efficiency to save the environment, reduce carbon dioxide emissions, and produce highly concentrated carbon dioxide product.

1.4 up-hill CO₂ permeation concept

The current project introduces a novel process to achieve an up-hill permeation of carbon dioxide based on the dual-phase membrane system; in this process, carbonate ions transported across the membrane in the molten phase are driven by an oxygen partial pressure gradient, which is a down-hill process compared to that of carbon dioxide (against a CO₂ partial pressure gradient). Therefore, the carbon dioxide can permeate through the membrane without its own partial pressure gradient, and to achieve this, an oxygen potential gradient against the carbon dioxide is required to overcome that potential of carbon dioxide: $\left| \mu'_{O_2} - \mu''_{O_2} \right| > \left| \mu'_{CO_2} - \mu''_{CO_2} \right|$, where μ'_{CO_2} and μ'_{O_2} are the chemical potential of CO₂ and O₂ in the feed side of the membrane;

μ'_{CO_2} and μ'_{O_2} are the chemical potential of CO₂ and O₂ in the permeate side of the membrane.

The experiment to achieve the CO₂ up-hill permeation is driven by the oxygen partial pressure gradient that is applied against the carbon dioxide chemical potential; the effective oxygen gradient between the feed-side and permeate-side provides the driving force for the carbon dioxide permeation (Fig. 1.9). According to the ion transportation mechanism below, there is no energy penalty for the up-hill carbon dioxide permeation because it is a spontaneous process by which the reaction moves from high potential to low potential ($\mu_{CO_2} + \mu_{O_2} > \mu'_{CO_2} + \mu'_{O_2}$; $CO_2 + \frac{1}{2}O_2 \rightarrow CO_2' + \frac{1}{2}O_2'$ is spontaneous process).

By using this new concept for a dual-phase membrane, a high permeability of carbon dioxide can be achieved at up to 900°C, but our experiments also investigate the high permeation rate using an La_{0.6}Sr_{0.4}Co_{0.2}Fe_{0.8}O_{3-δ} host at 600°C as an electron-conducting membrane substrate. The advantage of using this material rather than stainless steel or another electron-conducting metal material is that it avoids material oxidation at high temperatures with about 20% oxygen partial pressure. Chung et al. [24] studied a stainless steel molten carbonate dual-phase membrane for CO₂ separation, but significant corrosion of iron was found because of the molten phase carbonate; in particular, lithium carbonate reacts with iron. The current project uses LSCF instead of stainless steel as the electron-conducting membrane substrate to perform CO₂ permeation experiments, the new concept of up-hill CO₂ permeation was investigated, and the experiments based on this new concept was successfully performed.

To achieve up-hill carbon dioxide permeation, the oxygen potential difference must provide enough driving force. As the carbon dioxide permeates across the membrane against its own chemical potential difference (another situation is that there is no CO₂ partial pressure gradient), the oxygen needs to provide a greater potential difference that is against ΔP_{CO_2} and overcome the carbon dioxide gradient during permeation. This membrane technology targets flue gas treatment and post-combustion carbon dioxide capture at 500 to 600°C because of the high costs of gas compression and energy requirements from the polymeric membrane that is generally and widely used for CO₂ separation process; the up-hill permeation process is designed to perform at atmospheric pressure.

permeate-side gas will be oxygen free and contain a similar carbon dioxide mole fraction as in the feed-side inlet. Following this process, the carbon dioxide will permeate through the membrane with oxygen removal steps in the downstream; there is no requirement for a carbon dioxide potential difference between the feed side and the permeate side of the membrane. The oxygen removal step can be added and applied in future work.

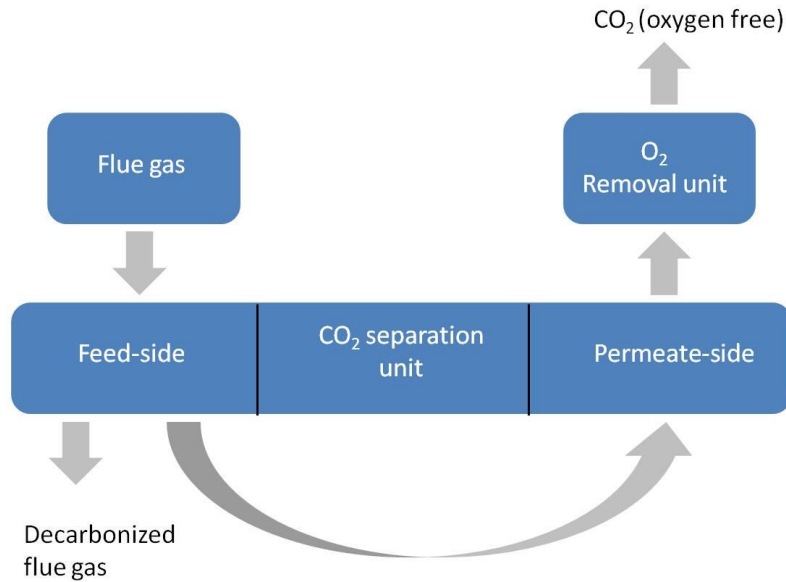


Figure 1.10 Carbon dioxide up-hill permeation process with an oxygen removal step for a typical power plant at 1 atmosphere; the oxygen required in the feed side is supplied by air, and this oxygen will permeate with CO₂ together to the permeate side and be removed by the O₂ removal unit.

1.5 Purpose of the study

Although some early-stage down-hill CO₂ permeation research work using this new concept for a dual-phase membrane has been reported by Anderson and Lin [25], the fabrication technology for the porous structure still needs to be improved by increasing membrane porosity and decreasing pore size, and the long-term operation requires better chemical and physical stability in the membrane. Sealing the dual-phase membrane is important for long-term operation, which is still a problem in the field; for example, Lin's work using glass-ceramic sealant caused the membrane to be blocked by molten glass [26].

More basic work needs to be done on the CO₃²⁻ permeation mechanism using an LSCF dual-phase membrane at lower temperatures than 900°C for wider application, such as flue gas treatment in the temperature range of 500 to 600°C. The current project aims to

Chapter 1. Introduction and aims

verify the feasibility of the new concept for a dual-phase membrane, fabricate a micro-porous structural substrate, improve the carbon dioxide permeation flux, solve existing problems based on established dual-phase membrane reactor systems, and achieve the novel concept of up-hill carbon dioxide permeation via an oxygen driving force that allows carbon dioxide to permeate against its own chemical potential. This carbon capture process is energy penalty free, as Section 1.4 explained.

To prepare the membrane reactor system, a micro-porous structural membrane support needed to be fabricated and prepared for molten carbonate infiltration. In this project, perovskite-type lanthanum strontium cobalt iron oxide (LSCF) was mainly used for membrane fabrication. Concerning the mechanical strength of the membrane materials, the membrane substrate was finally synthesised at 1,250°C instead of the 900°C used by Y.S. Lin [25]. The membrane substrate must be micro-porous because a small pore size provides a large surface area of the interface between the molten carbonate phase and the solid oxide phase, which can obtain a greater carbon dioxide flux. The LSCF pellet synthesised at 900°C showed a micro-porous structure, and it became dense when synthesised at 1,250°C. However, the dense membrane synthesised at 1,250°C showed a better mechanical strength than that synthesised at 900°C. To obtain a ‘strong’ membrane with a micro-porous structure, pore forming materials were used as described in detail in Chapter 4.

The sealing method is most important for the high-temperature membrane reactor. In the literature, many results indicate membrane leakage, but there is little discussion about leak development and how the problem was solved; many of them focus only on improving membrane permeance. In the current project, to perform the experiment successfully, various sealing materials have been tested. The sealing of the dual-phase membrane is complicated because of the ternary system and carbonate phase; the solid oxide phase and sealing material phase were in contact with each other. There is also a different situation before and after the melting temperature of the carbonate. Leaks in the membrane system at high temperatures need to be limited; it will disturb the results and cause misunderstandings. The current project also introduces a way to solve this problem (the details of the sealing method are introduced in Chapter 5).

1.6 Objectives and tasks

Objective 1. Fabricate a micro-porous LSCF membrane substrate with a homogeneous pore network inside. Pore size will be controlled and the pore diameter will be around 1 micron or less.

Task 1. Determine the temperature controlling program for sintering the porous structured membrane substrate.

Task 2. Control membrane porosity and pore size using pore former.

Task 3. Estimate the maximum pore size for carbonate infiltration.

Task 4. Measure the pore diameter and pore size using mercury porosimetry.

Objective 2. Synthesise a membrane which can work at high temperatures (700 to 900°C) without cracking during heating, permeation, and cooling.

Task 1. Fabricate an LSCF membrane substrate at higher temperatures (sintering at 1,200°C) instead of the 900°C used by Lin [25], because the LSCF membrane sintered at 1,200°C showed a dense structure with relatively high mechanical strength compared to that sintered at a lower temperature, but pore former must be applied to create porosity during membrane sintering.

Task 2. Test different temperature ramping rates for sintering the membrane and heating and cooling the reactor.

Task 3. Try to use soft sealant because the thermal expansion of the LSCF membrane and the tube support are different.

Objective 3. Find a method to limit or avoid the cross chamber leak in membrane reactor at high temperatures.

Task 1. Perform molten carbonate infiltration several times to avoid gas leaking from empty pores.

Task 2. Study the mechanism of leak development and design a new device or reactor to limit cross chamber leak.

Chapter 1. Introduction and aims

Objective 4. Find sealing material (soft sealant) and choose the appropriate one for the experiments.

Task 1. Test different sealing materials, such as ceramics, glass, commercial sealants, and metals.

Objective 5. Investigate the parameters that influence the CO₂ permeation rate to determine the limiting step for CO₂ permeation.

Task 1. Perform CO₂ permeation experiments with different parameters (CO₂, O₂ partial pressure, and temperature) to test their influence on CO₂ permeance or permeability.

Objective 6. Test the feasibility of up-hill CO₂ permeation and understand the mechanism.

Task 1. Perform CO₂ – O₂ co-permeation experiments without a CO₂ partial pressure gradient at 600°C.

Task 2. Perform CO₂ – O₂ co-permeation experiments against a CO₂ partial pressure gradient.

Task 3. Use symmetric and asymmetric conditions to study the up-hill process.

Task 4. Perform a CO₂ permeation experiment without P(O₂).

Task 5. Perform a O₂ permeation experiment without P(CO₂).

Chapter 2 Literature review

2.1 Introduction

A review of the literature on CO₂ capture from fossil-fuelled power plants was provided in Chapter 1. In Chapter 2, the focus is on ceramic-carbonate dual-phase membrane technology for CO₂ separation (Section 2.2) and the thermodynamics of molten alkali carbonate eutectics (Section 2.3). The molten alkali metal carbonate eutectic system where the original concept of dual-phase membrane was developed is discussed in detail, and the focus is on the dissociation process. A brief description of an oxygen-permeable membrane system is presented, including mixed ion-electron conducting (MIEC) and oxygen-conducting membranes. The attention is on mixed ion-electron conductive LSCF membrane material and its applications for gas separation membrane reactor systems. The membrane fabrication method and different pore formers applied for synthesising the micro-porous structure are discussed in Section 2.5. A review of high-temperature sealing for membrane systems is described in Section 2.6.

2.2 Carbonate ceramic dual-phase membrane technology for CO₂ separation

The new concept for a dual-phase membrane was studied a few years ago according to the CO₃²⁻ transportation mechanism in MCFCs and the O²⁻ transportation mechanism in SOFCs. However, the published works in the literature are few; some important work has been done by Anderson and Lin [25]. They synthesised a new porous La_{0.6}Sr_{0.4}Co_{0.8}Fe_{0.2}O_{3-δ} (LSCF6482) support infiltrated with a eutectic molten carbonate mixture (Li₂CO₃/Na₂CO₃/K₂CO₃) and showed a maximum CO₂ permeation of 2.01, 3.73, 4.63, and 4.77 × 10⁻⁸ mol m⁻² s⁻¹ Pa⁻¹ at 900°C with membrane thicknesses of 3.0, 1.5, 0.75, and 0.375 mm, respectively [25].

The mechanism of this new conceptual membrane was studied by Rui, Anderson, Lin, and Li [20, 27]. Theoretically, the dual-phase membrane consists of a mixed-conducting ceramic phase that provides oxygen vacancies (V_{O}) and electron holes (h^{\cdot}) for ionic conduction (O²⁻) and a molten carbonate phase for carbonate ion (CO₃²⁻) transportation

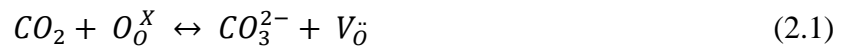
Chapter 2. Literature review

[27]. Rui et al. analysed the modelling of this new membrane concept and found that the dual-phase membrane showed high ionic conductivity and low electronic conductivity in the O₂-containing atmosphere with a permeated O₂/CO₂ mixture, while for pure CO₂ separation without O₂ contained in the feed gas, high electronic conductivity should be the main factor [20].

The mixed-conducting mechanism indicated that CO₂ was transported without O₂ in the feed gas and that solid oxide material (mixed-conducting material) provides an oxygen vacancy ($V_{\ddot{O}}$) for recycling O²⁻ in the membrane. CO₂ was transported by combining with O²⁻ to form CO₃²⁻ in molten carbonate electrolyte across the membrane, driven by the CO₂ partial pressure gradient between the upstream and downstream side of the membrane [25].

Early work done by Chung et al. [24] using porous stainless steel as the membrane substrate with molten carbonate intrusion showed a non-mixed-conducting CO₃²⁻ transportation mechanism at temperatures between 450°C and 650°C. The CO₂ and O₂ mixture was provided as feed gas and formed CO₃²⁻ because there is no oxygen vacancy in stainless steel, but it has an electron conductive property to transport electrons when CO₂ is released to the downstream side (the permeate side of the membrane).

As the membrane was made from two separate ionic conducting phases, mixed-conducting oxide ceramics (MCOC) and molten carbonate (MC), as shown in Fig. 1.7, the O₂ and CO₂ will be converted into charged ions by the following surface reaction:



The oxygen vacancies will be transported from the molten carbonate phase to the ceramic oxide phase. The surface reaction at the steady state can be given by the following:



In the downstream side of the membrane (the permeate side), the carbonate ions will be converted back into CO₂ by a surface reaction:



Oxygen ions into O₂.



The oxygen vacancies and electron holes diffuse in the MCO₃ phase and the ion CO₃²⁻ is transported from upstream to downstream in the molten carbonate phase [27].

Wade [23] used yttria-doped zirconia (YSZ, 8 mol% Y₂O₃) and gadolinia-doped ceria (GDC; Gd₂O₃ doped CeO₂) as the dual-phase membrane support for high-temperature CO₂ separation. The results showed that the YSZ-based substrate reacted with lithium carbonate irreversibly to form lithium zirconate. The permeation of CO₂ decreased with time as the zirconate formation reduced CO₃²⁻ transportation; the maximum permeability was about 0.3 μmol cm⁻² s⁻¹ at 850°C and 1 atm. The author also described the mechanism of CO₂ transport as the interaction between carbonate transport in the molten carbonate phase and oxide ion transport in the solid oxide phase, based on the opposite currents of carbonate and oxygen ions. It was also found by Benamira et al. [28] that a GDC dual-phase membrane has the lowest oxygen ion (O²⁻) conductivity with the highest amount of carbonates (60/40wt%). They believed that, at temperatures lower than the melting point, the solid carbonates may interfere with the mobility of oxygen ions.

Li et al. [29] reviewed applications of a dual-phase membrane for both intermediate-temperature solid oxide fuel cells and high-temperature CO₂ separation. Using samarium-doped ceria (SDC, CeO₂/Gd₂O₃) – Li/Na/K₂CO₃ (43.5/31.5/25 mol %) – the CO₂ permeation flux reached a maximum value of 6.60 × 10⁻² ml cm⁻² min⁻¹ (4.91 × 10⁻⁴ mol m⁻² s⁻¹) at 650°C. A Bi_{1.5}Y_{0.3}Sm_{0.2}O₃ supported dual-phase membrane showed selective permeation of CO₂ at 500-650°C; the CO₂ permeation increased with temperature, and the maximum permeable flux of CO₂ was 0.049 μmol cm⁻² s⁻¹. SDC used as a fuel cell electrolyte with ternary eutectic carbonate (Li/Na/K) infiltration exhibits ternary (O²⁻/H⁺/CO₃²⁻) conductivity because of the activated interface region [30].

A CO₂-absorbing material of lithium silicate were synthesised for CO₂ separation based on the similar mechanism of CO₃²⁻ transport by the carrier Li₂CO₃ and the Li₂SiO₃ interplay with the high-temperature CO₂ absorption material Li₄SiO₄. CO₂ selectivity from a CO₂/N₂ mixture of between 4 and 6 has been found in the temperature range of

523-625°C; the best CO₂ permeation result from the paper was around 0.1 μmol cm⁻² s⁻¹ at 520°C when calculated from 1 atm [31].

Liu et al. [32] investigated a composite electrolyte consisting of Sm³⁺ and Nd³⁺ co-doped ceria (SNDC) used as the membrane substrate and Li₂CO₃-Na₂CO₃ eutectic infiltrated into the membrane as the molten carbonate phase for MCFCs. It seems that the oxygen conductivity was improved by the increase in the number of oxygen transfer routes from the interface between SNDC and binary carbonates. The carbonates melt gradually in the transition temperature and spread into the pores of the interspaces of the dual-phase membrane, which improves pore-free consistency and increases the number of oxygen conduction routes from the interface. It can be concluded that the interface is the critical region for mobile ion transportation in gas permeation dual-phase membranes.

2.3 Thermodynamics of molten carbonates

2.3.1 Determining the decomposition rate

Several researchers have developed rate expressions for decomposition reactions, such as *Alkali metal carbonate(s) ↔ Alkali metal oxide(s) + Carbon dioxide(g)* [33]. Devyatkin et al. [34] initially observed carbonate melts release carbon dioxide generated from the following reaction:



The competition of these two reactions contributes the total weight loss of the carbonate mixture.

Timoshevskii [35] investigated the decomposition process of a single-component alkali metal carbonate, lithium carbonate, with a melting point of 700°C refer to the reaction (2.6). Gas diffusion from the mass sample was observed and the emission gas was impeded by the surface covered by the melting particles with extremely low vapour pressure of CO₂ at the temperature near its melting point. Timoshevskii also suggested that vacuum conditions in the atmosphere could increase carbonate dissociation. Lehman et al. [36] also studied the thermal decomposition of a single-component

Chapter 2. Literature review

substance, potassium carbonate, at its melting temperature of 900°C in equilibrium with $P(CO_2)$ and observed the dissociation of potassium carbonate in reaction 2.7 by heating the sample as a solid phase near the melting point and found the chemical equilibrium expression 2.8, in which the maximum rate of weight loss correlates with the change in Gibbs free energy under the standard conditions [37]. (The presence of CO_2 in atmosphere prevents the further decomposition, the weight loss is because of evaporation of K_2O , the maximum weight loss refer to the total K_2O in the melt, the rate can be determined by slope of weight loss from experiment.)

$$\Delta G^0 = -R_u T \ln \left[\frac{E_{K_2O} P_{CO_2}}{E_{K_2CO_3}} \right] \quad (2.8)$$

In expression 2.8, E_{K_2O} and $E_{K_2CO_3}$ represent the activities of the K_2O and K_2CO_3 in solid phases, respectively, and P_{CO_2} is the partial pressure of carbon dioxide in equilibrium from the decomposition reaction. R_u is the universal gas constant.

In the equilibrium condition, Lehman assumed that $E_{K_2CO_3}$ remains constant because of the appearance of K_2CO_3 in the solid phase, and the mass of this parent material K_2CO_3 is larger than that of decomposed products such as K_2O . The ratio of activity E_{K_2O} to $E_{K_2CO_3}$ can represent the ratio of the weight loss of the produced material (K_2O) to the per unit mass of the initial material K_2CO_3 . Equation 2.8 can be expressed as follows:

$$\Delta G^0 = -R_u T \ln \left[\frac{1}{m_{K_2CO_3}} \cdot \frac{dm_{K_2O}}{dt} \cdot P_{CO_2} \right] \quad (2.9)$$

After conducting a thermal stability experiment, Lee et al. [37] explained that the partial pressure of carbon dioxide can be determined from the calculation expressed in equation 2.10, where it is related to two parameters: the volumetric flow rate of atmosphere gas (Q_{N_2}) into the TGA apparatus and the weight loss rate of the K_2O (χ).

$$P_{CO_2} = \left(\frac{\frac{\chi}{MW_{K_2O}}}{\frac{\chi}{MW_{K_2O}} + \frac{1.16 Q_{N_2}}{10^3 MW_{N_2}}} \right) \cdot P_{atm} \quad (2.10)$$

Substitution of P_{CO_2} into equation 2.9 can yield equation 2.11, where the maximum rate of weight loss χ can be determined once the change of Gibbs free energy is given.

$$\Delta G^0 = -R_u T \ln \left[\frac{\chi}{m_{0,K_2CO_3}} \cdot \left(\frac{\frac{\chi}{MW_{K_2O}}}{\frac{\chi}{MW_{K_2O}} + \frac{1.16 Q_{N_2}}{10^3 MW_{N_2}}} \right) \cdot P_{atm} \right] \quad (2.11)$$

A similar calculation can be applied to other components, such as lithium carbonate, in the carbonate mixture.

Lehman et al. [36] indicated that the presence of CO₂ in the atmosphere can effectively decrease the decomposition of potassium carbonate and that the weight loss of potassium carbonate depends on the temperature and the CO₂ partial pressure.

According to Lee et al [37], the carbonate mixture's decomposition is a single-step reaction that occurs in series or simultaneously. Therefore, the total weight loss of the carbonate mixture is a sum of that of single components in the mixture, such as lithium and potassium carbonate. The rate of total weight loss can be expressed as follows:

$$x_{total} = \sum_{k=1}^2 x_k = \frac{dm_{K_2O}}{dt} + \frac{dm_{Li_2O}}{dt} \quad (2.12)$$

2.3.2 Thermal stability of alkali metal carbonates

The rate of weight loss of carbonate mixtures (Li:K=3:2) was measured by Lee et al. [37] using TGA. This test was performed at the heating rate of 10°C/min, and during the heating and the following stabilised period at 620°C, CO₂ gas was continuously fed into the system at a volumetric flow rate of 100 ml/min. Then, it was switched to a nitrogen atmosphere to monitor the rate of weight change of the carbonate mixture before the gas was finally switched back to CO₂. During the steady-state condition at the temperature of 620°C, the weight value became constant only in a CO₂ atmosphere and kept decreasing in an N₂ atmosphere (Fig. 2.1). It is interesting that the post sample formed a different structure in which carbonate particles were fused together, while the initial melt sample had an individual fine particle appearance. The authors explained that this was due to the diffusion of the grain boundary after CO₂ was released from the surface or pores.

Olivares et al. [38] also tested the thermal stability of an Li-Na-K carbonate eutectic mixture in various ratios of Li/Na/K and concluded that the Li-Na-K carbonate is significantly influenced by the gas atmosphere under which it is measured. In a CO₂ atmosphere, the molten Li-Na-K carbonate is stable up to at least 1,000°C; in argon or air, the stability is much lower.

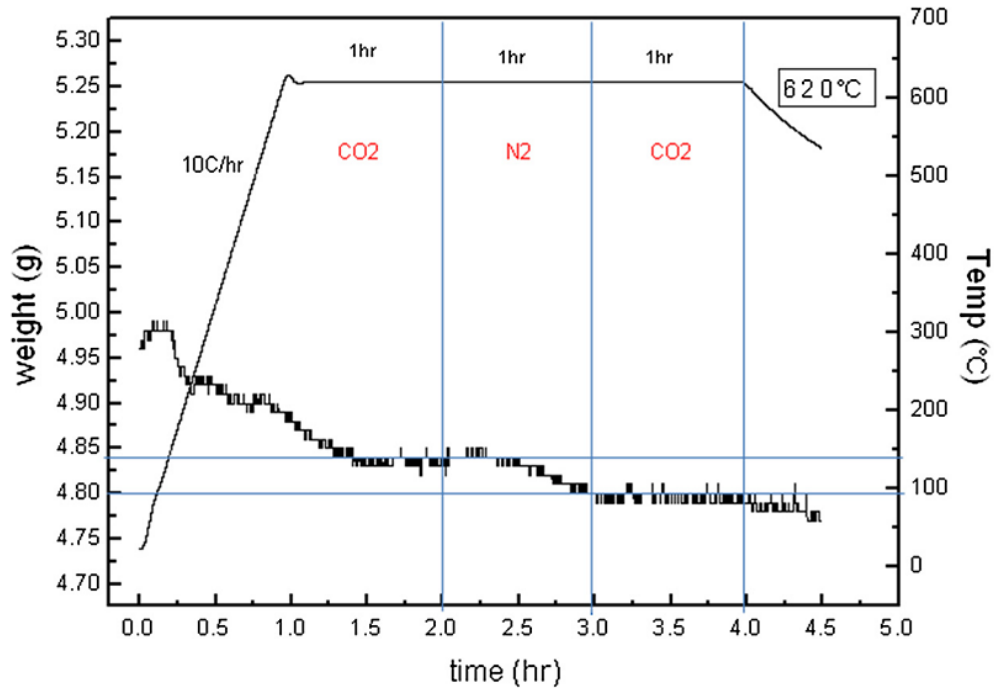


Figure 2.1 Weight change of a carbonate mixture (60 wt% lithium carbonate and 40wt% potassium carbonate) up to the steady-state condition of 620°C in a calcination furnace [37].

2.3.3 Equilibrium CO₂ partial pressure

The stability of molten phase carbonates at high temperatures over their melting point is important for dual-phase membrane and CO₂ permeation experiments; a eutectic alkali metal lithium/sodium/potassium carbonate mixture is used in the current project, and its chemical stability was studied by calculating ΔG for decomposition reactions and finding the equilibrium line of CO₂ partial pressure at different temperatures. The detailed calculations are presented in **Appendix B**. One example study of the chemical stability of potassium carbonate is shown below, and a powder heating experiment follows the thermodynamic calculations.

Several impurities exist in potassium carbonate, e.g., K₂HCO₃, KOH, and K₂O, because of the H₂O and CO₂ partial pressure in the atmosphere. Mainly, in air, some K₂CO₃ powder will absorb water and CO₂ to form K₂HCO₃, but it will decompose rapidly at high temperatures [36]. The carbonate decomposes at high temperatures according to the reaction as follows:



$$\Delta_r G^0(298 \text{ K}) = \Delta_f G^0(\text{products}) - \Delta_f G^0(\text{reactants}) \quad (2.14)$$

Chapter 2. Literature review

The $\Delta_r G^0$ for different temperatures other than 298K was calculated by Eq. 2.15:

$$\Delta G = \Delta H - T\Delta S \quad (2.15)$$

That is,

$$\Delta_r G^0(T) = \Delta_r G^0(298 \text{ K}) + \int_{298\text{K}}^T \Delta C_p dT' - T \int_{298\text{K}}^T \frac{\Delta C_p}{T'} dT' \quad (2.16)$$

where ΔC_p is calculated from the heat capacities of the products and reactants.

The simplified method to obtain ΔG was given by the following expression for convenience:

$$\Delta_r G^0(T) = a + bT + cT(\ln T - 1) \quad (2.17)$$

The coefficients a, b, and c, were provided by the literature [39].

In practice, the pressure of the reaction system was considered one atmosphere; the relation between the Gibbs free energy of the reaction and the standard Gibbs free energy of the reaction was given as follows:

$$\Delta_r G(T) = \Delta_r G^0(T) + RT \ln \frac{P_{\text{CO}_2}}{P_{\text{atm}}} \quad (2.18)$$

According to Eq. 2.17 and Eq. 2.18, the $\Delta_r G(T)$ can be expressed as follows:

$$\Delta_r G(T) = a + bT + cT(\ln T - 1) + RT \ln \frac{P_{\text{CO}_2}}{P_{\text{atm}}} \quad (2.19)$$

That is,

$$\Delta_r G(T) = 386670 + 8.38T - 30.12T(\ln T - 1) + 8.314T \left(\ln \frac{P_{\text{CO}_2}}{P_{\text{atm}}} \right)$$

For $\Delta G < 0$, the reaction $\text{K}_2\text{CO}_3 \rightleftharpoons \text{K}_2\text{O} + \text{CO}_2$ will carry forward from the left side to the right side to produce CO_2 ; while $\Delta G > 0$, the reaction will consume K_2O and CO_2 to form K_2CO_3 . To obtain the equilibrium line of the relation between the CO_2 partial pressure and the temperature, assuming the $\Delta_r G(T) = 0$.

$$\text{That is, } 386670 + 8.38T - 30.12T(\ln T - 1) + 8.314T \left(\ln \frac{P_{\text{CO}_2}}{P_{\text{atm}}} \right) = 0.$$

$\ln \frac{P_{\text{CO}_2}}{P_{\text{atm}}}$ can be obtained by the following:

$$\ln \frac{P_{\text{CO}_2}}{P_{\text{atm}}} = \frac{30.12T(\ln(T)-1) - 386670 - 8.38T}{8.314T} \quad (2.20)$$

Expression 2.20 is the relation between temperature and CO₂ partial pressure for reaction 2.13; the graph according to the equilibrium equation is shown in Fig. 2.2.

According to the literature [36], the data for K₂O are not valid at temperatures higher than 880°C for expression 2.20, so the thermodynamic calculations for reaction 2.13 were limited to temperatures < 880°C. At 880°C (1,153k), $\frac{P_{\text{CO}_2}}{P_{\text{atm}}} = 3.658 \times 10^{-9}$; theoretically, the potassium carbonate was stable according to thermodynamic calculations at temperatures < 880°C.

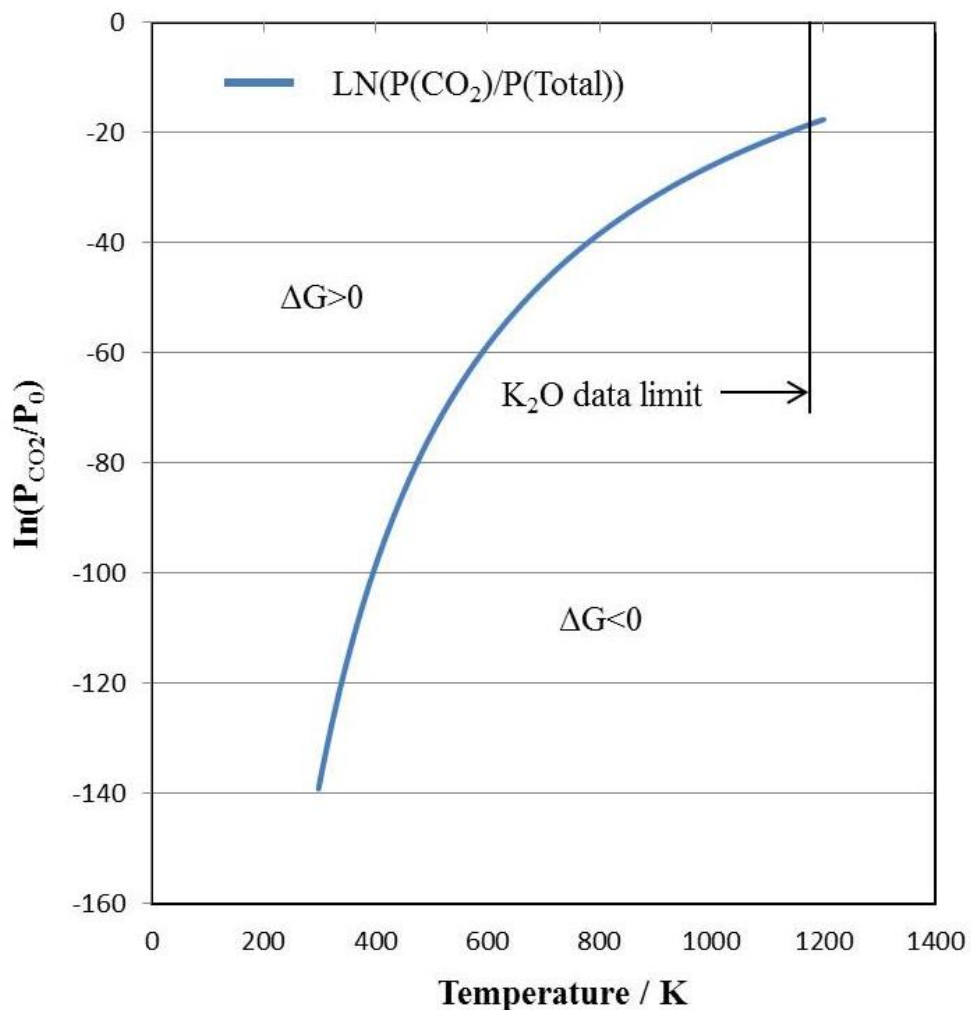


Figure 2.2 Equilibrium CO₂ partial pressure for potassium carbonate according to expression 2.20 (equilibrium line); Appendix B shows equilibrium CO₂ for different carbonate eutectic mixtures.

Thermal decomposition of potassium carbonate in a helium environment:

A potassium carbonate decomposition test was carried out to analyse the thermal stability of potassium carbonate, which is one of the alkali metal salts used for the

fabrication of dual-phase membranes. As the melting point of potassium carbonate is 891°C in air, a decomposition test was undertaken. A simple quartz tube reactor (Fig. 2.3) was set up to heat 1 gram of potassium carbonate powder at 900°C at the ramp rate of 1°C min⁻¹; 10 ml min⁻¹ helium was fed into the quartz tube reactor as a carrier gas, and the outlet gas composition was analysed by GC. Helium was fed to the reactor tube before heating the powder to flush the air from the tube. This test is not a typical permeation experiment, and further study on different compositions of alkali metal carbonate mixtures is required in future work.

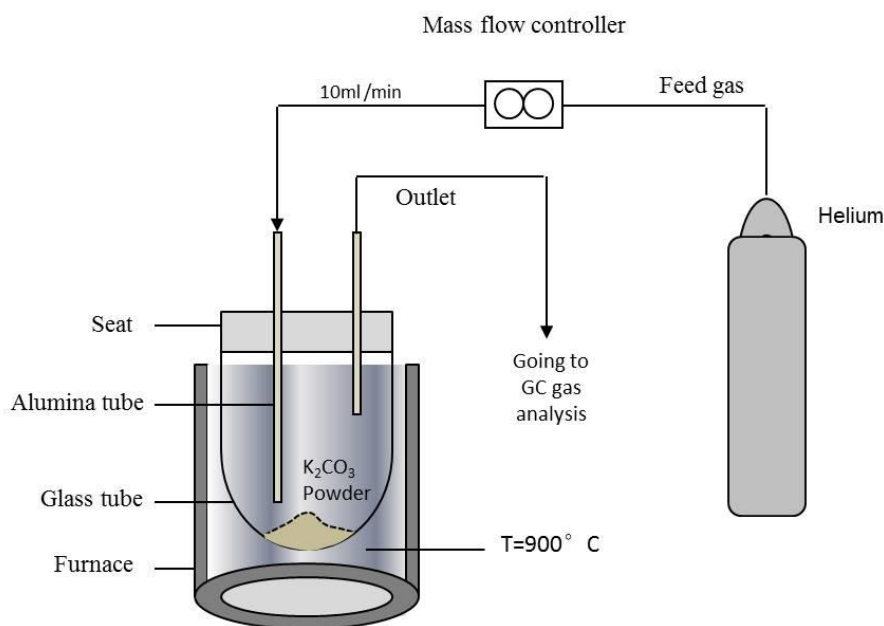


Figure 2.3 Experimental reactor tube for heating potassium carbonate powder.

The test was carried out under a dry helium atmosphere to measure the content of the outlet gas by heating 1 g of potassium carbonate powder to 900°C (Fig. 2.3). The CO₂ mole fraction in the outlet gas from the reactor tube increased gradually as the temperature increased. The maximum CO₂ mole fraction, which is 0.68% with a helium flow rate of 10 ml min⁻¹, was obtained at 900°C. Fig. 2.4 shows the CO₂ percentage as a function of time at a constant temperature of 900°C. It can be seen that the CO₂ mole fraction decreased and became stable after about 100 minutes with fluctuations.

The time required for the release of CO₂ from 1 gram of potassium carbonate can be calculated as follows. The molecular weight of K₂CO₃ is 138.2 g mol⁻¹; the mole value of 1 g of K₂CO₃ powder is $M = \frac{1}{138.19}$ mol. The CO₂ mole fraction increased from 0 to 0.68 mol% as the temperature increased from 25°C to 900°C; assuming the average CO₂ emission rate of the mole fraction is 0.5 mol% min⁻¹ (the maximum is about 6.8 mol%

Chapter 2. Literature review

min⁻¹) during heating of the reactor and including the time period for maintaining the system at 900°C for two hours.

The average flow rate of CO₂ is expressed as follows:

$$f(\text{CO}_2) = \frac{0.005 \times 10 \text{ ml/min}}{22400 \text{ ml/mol}} = \frac{5}{2240000} \text{ mol min}^{-1}$$

The estimated time for all CO₂ release from CO₃²⁻ to helium is calculated by the following:

$$T = \frac{M}{f_{\text{CO}_2}} = \frac{2240000}{138 \times 5} \approx 3246 \text{ minutes} > 50 \text{ hours}$$

It takes more than 50 hours for 1 gram of potassium carbonate to release CO₂ according to the calculation; it is shown in Fig. 2.4 that the CO₂ content decreased from 0.68 mol% min⁻¹ to less than 0.1 mol% min⁻¹ and become stable after two hours at 900°C in a pure helium atmosphere. The CO₂ became stable after two hours, indicating that the high content of CO₂ at the beginning at 900°C was a result of the calcination of impurities.

After 100 minutes, CO₂ mol% decreased to less than 0.1% from the maximum of 0.68% and became stable; the CO₂ flow rate can be given by the following:

$$\text{Release (CO}_2\text{)}_{\text{stable}} = \frac{0.001 \times 10 \text{ ml/min}}{22400 \text{ ml/mol} \times 60 \text{ s} \times 0.5 \text{ cm}^2} \times 10^6 = 0.0149 \mu \text{ mol cm}^{-2} \text{ s}^{-1}$$

It can be determined that the flow rate of CO₂ release from 1 gram of potassium carbonate is lower than the CO₂ permeation rate (an average of 0.368 μ mol cm⁻² s⁻¹; more than one hour) in the down-hill permeation experiment with similar conditions as shown in Fig. 5.6 in Chapter 5. The hypothesis is that the CO₂ permeation rate is greater than the CO₂ release rate from molten phase carbonate above its melting point in a pure helium atmosphere. The partial pressure of CO₂ in the permeate side is above the equilibrium CO₂ partial pressure during permeation experiments, and this prevents the decomposition of the carbonate. The CO₂ moles that permeated across the membrane are much greater in number than the moles of carbonate ion in the molten carbonate phase (this can be determined by the long-term permeation experiment described in Chapter 7).

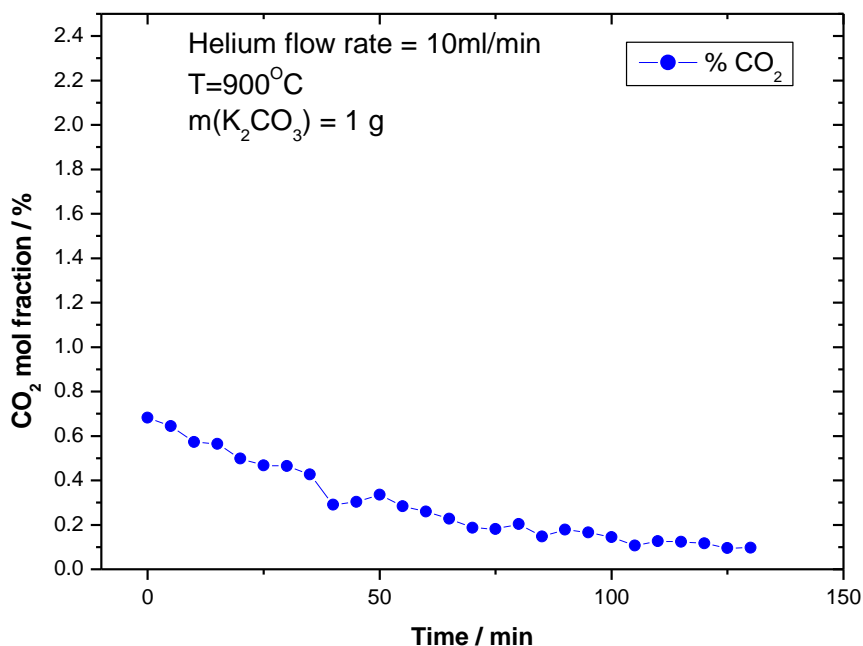


Figure 2.4 CO₂ mol fraction from the outlet gas of the reactor as a function of time.

2.3.4 Electrochemical stability of oxide species in molten alkali eutectic

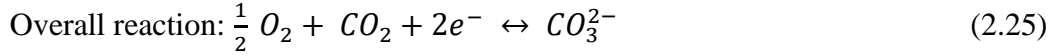
The chemical and electrical properties of molten alkali metal carbonate have been studied for 20 years, and the difficulty lies in explaining the complex oxygen reduction mechanism in acidic media (high CO₂ partial pressure, P_{CO_2} from 0.1 to 0.9 atm) or basic media (very low CO₂ partial pressure or high oxygen ion content in the melt) [40].

Appleby and Nicholson [41] analysed the oxygen reduction reaction in molten carbonates in 1972 and observed that the oxygen reacted with carbonate ions and formed superoxide O_2^- and peroxide O_2^{2-} ions. They found that the concentration of these oxide species depends on the cation in the melt. In a Li-rich melt or pure Li₂CO₃, peroxide species are dominant; in a K-rich melt, superoxide species are dominant. For a pure lithium carbonate melt, the following oxygen reduction mechanism was proposed by Appleby and Nicholson:





where O^- is a transient species.



Appleby and Nicholson explained that the charge – transfer step in reaction 2.22 is the rate-determining step for immersed electrodes. By examining the oxygen reduction in binary (Li:K=47:53, Na:K=43:57) and ternary (Li:Na:K=43.5:31.5:25) eutectic carbonate mixtures in a temperature range of 700-800 °C, they concluded that the electroactive species is not oxygen molecules; both O_2^- and O_2^{2-} are present and are reduced in the parallel steps; reaction 2.24's neutralisation of O^{2-} is slow [42].

Cassir et al. [40] investigated the electrochemical behaviour of the reduced oxygen species O_2^{2-} and O_2^- in several alkali metal carbonate melts at different oxoacidity levels and temperatures. They developed theoretical acidity potential diagrams (Fig. 2.5) at different temperatures that provided the idea to analyse the stable condition of O_2^{2-} and O_2^- . The calculation of the electrochemical stability range for both binary (Na-Li, Li-K or Na-K) and ternary (Li-Na-K) eutectics considering the limits: oxidation (O^{2-} , O_2^{2-} or O_2^- formation), reduction (M(K or Na), CO (C formation), basicity (M_2O saturation), and acidity (P_{CO_2} set at 1 atm). The acidity potential diagram for ternary eutectic (Li-Na-K) at different temperatures is shown below in Fig. 2.5; the stability range of oxygen and the peroxide ion O_2^{2-} exhibits no significant move from 450 to 650 °C. No superoxide ion O_2^- is shown in Fig. 2.5 because superoxide species are not stable in the Li containing melts with activity as low as 10^{-3} . At a lower temperature, 450 °C, there is C formation in acidic media when CO_2 partial pressure is relatively large; to avoid this carbon formation, acidic media or low temperature should not be applied.

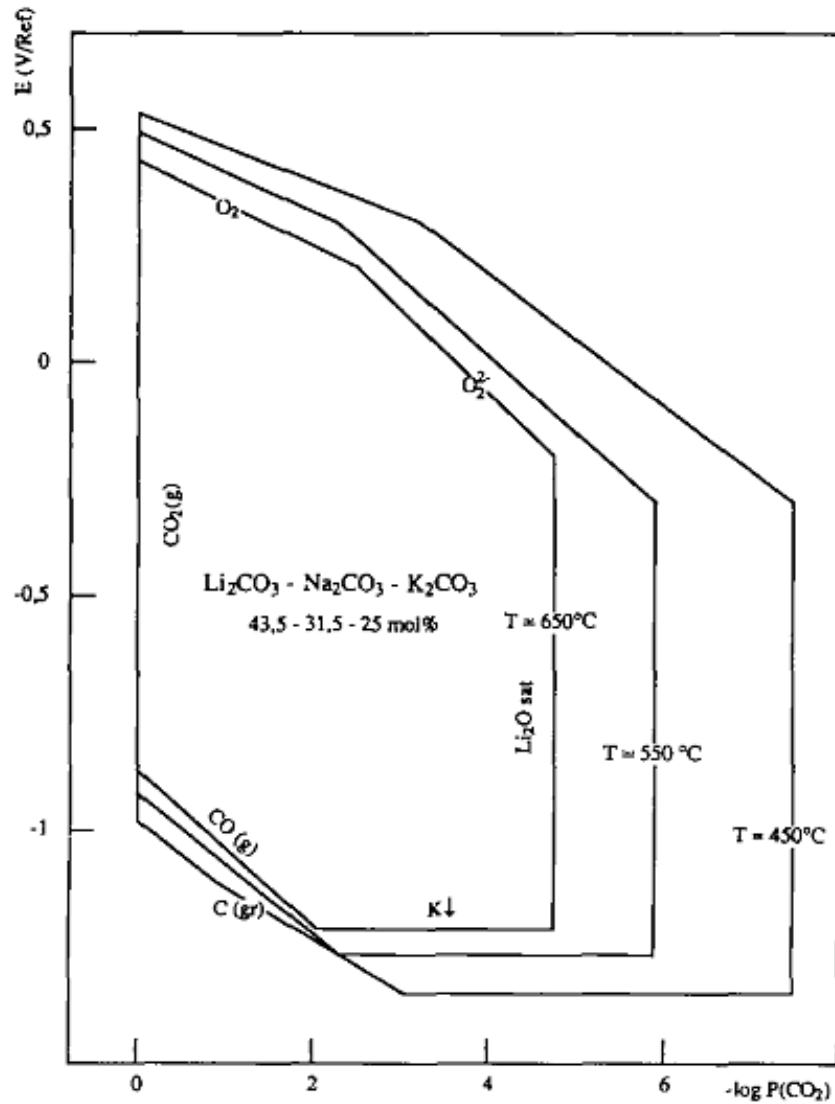


Figure 2.5 Electrochemical stability range in molten $\text{Li}_2\text{CO}_3\text{-Na}_2\text{CO}_3\text{-K}_2\text{CO}_3$ eutectic [40].

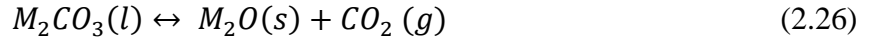
Table 2.1 gives information on oxide species' molar ratios in different carbonate melts when the oxygen partial pressure is 1 atm. As Cassir explained, superoxide ions are not stable in lithium-containing carbonate melts (Li, Li-Na, Li-K, or Li-Na-K), so the molar percent of superoxide ions is considered to be zero. However, in a Na-K carbonate melt, the superoxide ions comprise 45 mol%, 39 mol%, and 32 mol% of the total oxide species at the temperature of 1,000K, 1,100K, and 1,200K, respectively. In the ternary carbonate melt (Li-Na-K), the oxygen ion O^{2-} comprises 94.0, 95.7, and 96.8 molar percent at 1,000K, 1,100K, and 1,200K, respectively.

Table 2.1 Molar ratios of oxide, peroxide, and superoxide ions in alkali molten carbonates initially contain 3 mole percent oxide ions under pressure of $P(\text{O}_2) = 1$ atm [40].

Melt	$x(O^{2-}) - x(O_2^{2-}) - x(O_2^-)$ (m/o)		
	1000°K	1100°K	1200°K
Li	99.97-0.03-0	99.96-0.04-0	99.95-0.05-0
Li-Na	98.1-1.9-0	98.3-1.7-0	98.5-1.5-0
Li-K	95.1-4.9-0	96.9-3.1-0	97.8-2.2-0
Li-Na-K	94.0-6.0-0	95.7-4.3-0	96.8-3.2-0
Na			51-39-10
Na-K	10-45-45	22-39-39	37-32-32
K			8.6-8.7-83

2.3.5 Ternary molten alkali metal carbonates

Chery et al. [43] developed an expression for the auto-dissociation equilibrium of molten alkali metal carbonates:



In an ion form,



$$K^* = \frac{a(M_2O) \cdot P(CO_2)}{a(M_2CO_3)} \quad (2.28)$$

This process with the capability of gaining or releasing oxide ions was called oxoacidity by Chery et al. The oxoacidity domain value ($PK^* = -\log(K^*)$) depends on the nature of the molten carbonate and the temperature. The authors stated that the activity of molten salt is fixed in both pure and mixed carbonates and that the conditional auto-dissociation constant is given by Eq. 2.29:

$$K_d^* = a(M_2O) \cdot P(CO_2) \quad (2.29)$$

The oxoacidity domain, defined by PK_d^* values at different temperatures for alkali metal carbonate melts is shown in Table 2.2. For all molten carbonate types, PK_d^* decreases with increasing temperatures and excess lithium carbonate decreases the PK_d^* value. At the same temperature, such as 650°C, the values of PK_d^* in molten Li-K (62-38) and Li-Na (52-48) are similar and much lower than those of Na-K at 750°C. The authors concluded that a good compromise between temperature and high oxoacidity is a ternary molten carbonate (Li-Na-K) with high PK_d^* (8.26) at a low temperature of 450°C.

Table 2.2 pK_d^* values for each molten alkali metal carbonate at different temperatures [43].

	Temperatures							
	450°C 723 K	550°C 823 K	600°C 873 K	650°C 923 K	750°C 973 K	800°C 1023 K	850°C 1073 K	MP (°C)
Li-Na-K (43.5-31.5-25)	8.26	6.37	5.60	4.92	3.41			397
Li-K (42.7-57.3)	–	6.70	5.91	5.22	3.67			498
Li-K (62-38)	–	6.36	5.58	4.89	3.37			488
Li-Na (52-48)	–	6.37	5.59	4.91	3.39			501
Na-K (56-44)	–	–	–	–	9.14	8.42	7.75	710
Li	–	–	–	–	3.04			726

2.4 Oxygen-permeable membranes

2.4.1 MIEC membranes

There are two types of oxygen-permeable membrane systems based on ceramics: mixed ionic-electronic conducting (MIEC) membranes and pure oxygen conducting membranes. The focus of this section is mainly MIEC membranes.

Mixed ionic-electronic conducting (MIEC) membranes have wide applications in the field of oxygen separation, solid oxide fuel cells [44-46] and membrane reactors for the light hydrocarbon oxidation process [47-49], and so on. MIEC membranes can perm-selectively separate oxygen from air over a range of high temperatures. The materials for MIEC membrane fabrication are normally perovskite-type or fluorite-type oxides [50-52]. The oxygen permeation flux through a dense MIEC membrane can be described by the Wagner equation (2.30), which considers the bulk diffusion as the limiting step. The principle shows that the oxygen flux can be increased by reducing the membrane thickness (increasing bulk diffusion) until it less than a characteristic value at which the oxygen permeation is determined only by surface exchange kinetics [53].

$$J_{O_2} = \frac{RT}{16F^2L} \int_{P_{O_2}'}^{P_{O_2}''} \sigma_{amb}(P_{O_2}) d \ln P_{O_2} \quad (2.30)$$

where J_{O_2} is the oxygen permeation flux in $mol m^{-2} s^{-1}$; R is the gas constant; F is the Faraday constant; L is membrane thickness; σ_{amb} is the ambipolar conductivity; and P_{O_2}'' and P_{O_2}' are high and low oxygen partial pressure, respectively.

Theoretically, there are three progressive steps that determine the oxygen permeation rate, which are called rate-determining steps (r.d.s.) or limiting steps. The schematic graph in Fig. 2.6 shows that the first step is the surface exchange reaction on interface I; the second step is the bulk diffusion of charged species and electron/electron holes; and the third step is the surface exchange reaction on interface II [54].

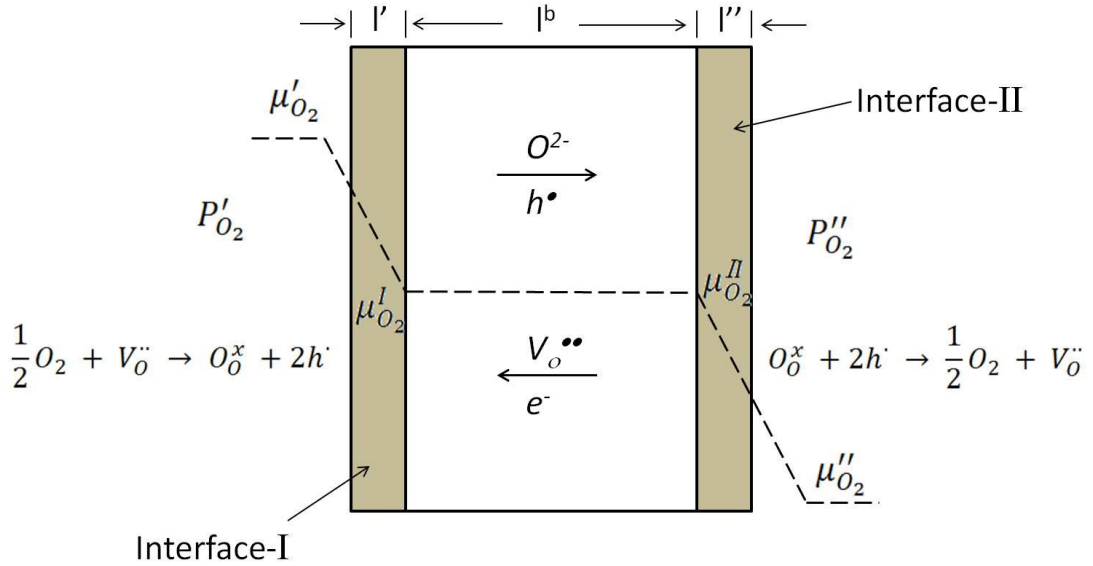


Figure 2.6 Schematic graph of oxygen transportation across an MIEC membrane by chemical potential drop [54, 55].

Oxygen permeation through a dense MIEC membrane with a perovskite structure normally operates at high temperatures, typically 800°C to 900°C, and high oxygen flux can be observed. Although the oxygen ions are transported across the membrane from the high concentration side to the low concentration side, the overall charge is balanced and maintained by the opposite movement of the electron flow [53, 56].

The ideal perovskite crystal structure ABO_3 is shown in Fig. 2.7, which consists of a large A cation and a smaller B cation. An A-site ion can be a rare earth, alkali, or alkaline earth ion such as La or Sr; a B-site ion is a transitional metal such as Fe or Co [57]. The shape of the crystal structure is mainly determined by the relative size of the A and B ions; an equation for estimating the values of the tolerance factor (t) calculated by Goldschmidt shows that the perovskite structure can be maintained if the tolerance factor t is between 0.75 and 1.

$$t = \frac{R_A + R_O}{\sqrt{2}(R_B + R_O)} \quad (2.31)$$

where R_A , R_B , and R_O are the radius of the A cation, B cation, and oxygen anion, respectively.

If the factor t is lower than 0.75, an A ion will be too small to fit into a B ion site; if the factor t is greater than 1, a B ion will be too large to fit into an A ion site [58].

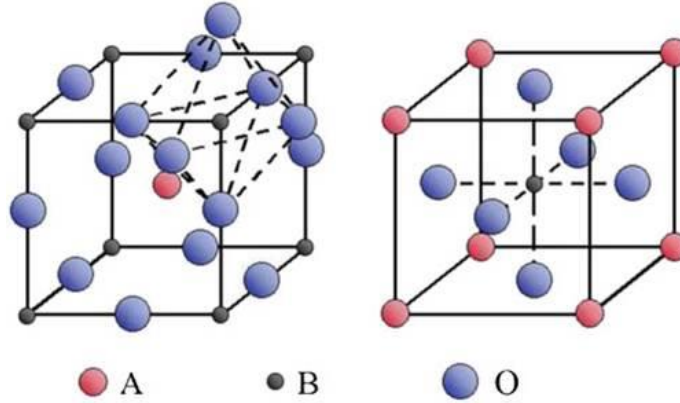


Figure 2.7 Crystal structure of an ideal ABO_3 perovskite oxide [59].

In the crystal, several defects can be found within the structure; the defects are generally categorised as vacancies (particles missing in the lattice), interstitial particles (particles should not occupy the lattice sites), or substitutional particles (lattice sites occupied by foreign particles). The vacancy defect in the perovskite can provide oxygen ion mobility, which allows ion diffusion within the crystal structure, and the oxygen permeability or ion conducting is mainly due to the high tolerance of the perovskite materials [53, 60, 61]. When a metal ion with a low valence state is doped into an A site, oxygen vacancies are generated and the valence state of a B site changes to maintain the electron neutrality. To improve the stability of the crystal structure, doping a B site with a more stable ion can be applied to produce a structure of $A_xA'_{1-x}B_yB'_{1-y}O_{3-\delta}$. It is noted that δ represents the number of defects or vacancies; a large number of vacancies results in high oxygen permeation flux. Therefore, to increase the vacancies, many different ions can be doped into the crystal structure to improve the oxygen flux [62-64].

At high temperatures, the oxygen vacancies are reduced by the occupying oxygen within the perovskite structure and two electron holes form, as expressed in Equation 2.32:



where $V_O^{\bullet\bullet}$ is the oxygen vacancy, O_O^x is the oxygen in the lattice, and h^{\bullet} is the electron hole [60].

Researchers primarily use MIEC membranes for the application of oxy-combustion processes, and their attention is on the development of MIEC membrane reactor technology for hydrocarbon fuel combustion. In particular, the lanthanum cobaltite perovskite-type ceramics have been studied and developed extensively [65, 66]. Recently, the new MIEC materials studied for membrane reactor systems typically include modified perovskite (e.g., $SrFeCo_{0.5}O_x$ [67]), structured ceramic (e.g., $La_{0.6}Sr_{1.4}GaFeO_{3.5}$ [68]), ceramic-metal dual-phase membranes such as $La_{0.8}Sr_{0.2}Co_{0.1}Fe_{0.69}Cr_{0.2}Mg_{0.01}O_{3+\delta}$ 50Ag/50Pd [69], and thin dual-phase membranes with two phases, one of yttria-stabilized zirconia (YSZ) and the other is a Pd phase [70, 71].

2.4.2 Perovskite-type LSCF system

The perovskite-type ABO_3 oxide $La_{1-x}Sr_xCo_{1-y}Fe_yO_{3-\delta}$ has been studied and exhibits mixed oxygen ion- and electron-conducting (MIEC) properties and can potentially be used for cathode materials of solid oxide fuel cells (SOFCs) or oxygen-permeable membranes. Many researchers have found that the combination of x and y strongly affects its physical and chemical properties, especially the electrical conductivity, catalytic activity, and thermal expansion. For example, electronic and ion conductivity and catalytic activity can be improved by increasing x and decreasing y; however, it has a negative effect on the chemical stability of the material [72].

The membrane material used in the project for up-hill CO_2 permeation and kinetic experiment is $La_6Sr_4Co_2Fe_8O_{3-\delta}$ (LSCF6428), and the electronic conductivity is about 250 S cm^{-1} at 1073 K. However, oxygen ionic conductivity is slow ($10^{-2} \text{ S cm}^{-1}$ at 1273 K). Lin [27] pointed out that, in high-temperature (700°C ~ 950°C) CO_2 permeation experiments using LSCF materials as membrane substrates, oxygen ionic conductivity is the limiting step for permeating CO_2 according to down-hill permeation results. Therefore, enhancing the ionic conductivity of LSCF without degradation will improve LSCF membrane CO_2 permeance at high temperatures [72].

Tai et al. [73] studied the high-temperature phase stability and electrical properties of $La_{1-x}Sr_xCo_{0.2}Fe_{0.8}O_3$ as a function of temperature, oxygen activity, and Sr content by

thermogravimetric (TG) analysis. They started their experiments by equilibrating an LSCF sample with pure oxygen at 1,200°C; the oxygen was considered to be in equilibrium with given oxygen activity when the sample weight remained steady for 24 hr. The oxygen activity then dropped gradually from 10^{-1} to 10^{-19} , and the weight loss during the reduction process was recorded. The fully reduced sample (reducing LSCF into components of La_2O_3 , SrO , Co , and Fe at 1,200°C) was then successfully reoxidised to its original state ($La_{1-x}Sr_xCo_{1-y}Fe_yO_{3-\delta}$, $La^{III}, Sr^{II}, Co^{III}, Fe^{III}$, synthesised from $La(NO_3)_3 \cdot 6H_2O$, $Sr(NO_3)_2$, $Co(NO_3)_2 \cdot 6H_2O$, and $Fe(NO_3)_3$; Co^{II} were oxidised to Co^{III} at a temperature of about 800°C).

The TG results for various $La_{1-x}Sr_xCo_{0.2}Fe_{0.8}O_3$ composites during the heating process under an oxygen atmosphere are presented in the Fig. 2.8 below, which shows that the undoped sample ($Sr = 0$) is stable at 1,100°C; the weight loss is not significant at 1,200°C. A maximum weight loss of 1% was found for the Sr doped sample with $Sr = 0.4$; this weight change was found to be reversible and depends on oxygen activity. Therefore, Tai et al. concluded that the oxygen evolution from an oxide sample results in weight loss.

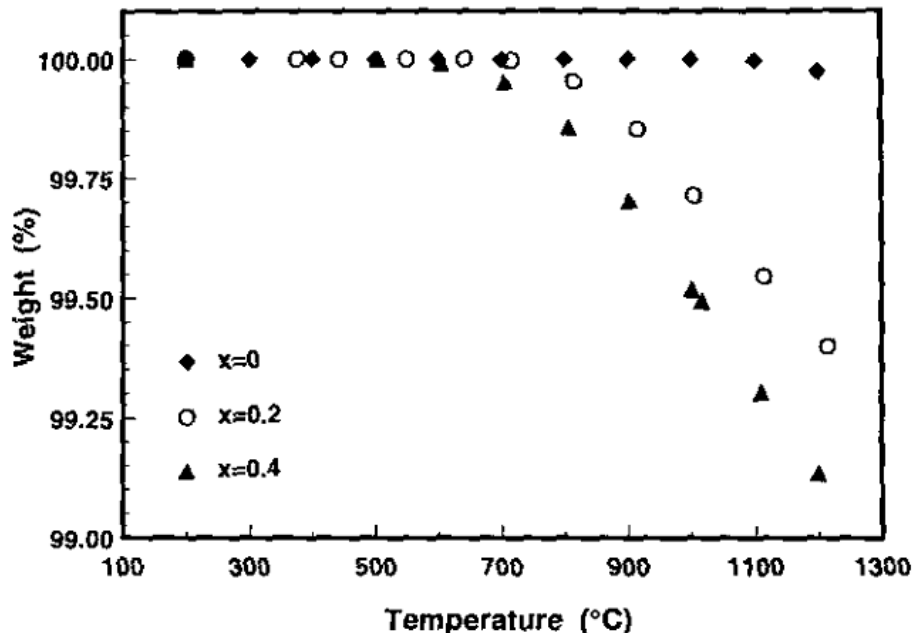


Figure 2.8 Relative weight change of LSCF sample as a function of Sr content (moles) and temperatures under oxygen [73].

Additional work has been done to measure and calculate the composition of LSCF at room temperature and high temperature; in particular, oxygen contents with Sr values of

0, 0.2, and 0.4 at ambient atmosphere are presented in the table below. Table 2.3 shows that increasing Sr content resulted in oxygen deficiency [74].

Table 2.3 Oxygen content (moles) of LSCF compositions under various conditions [74].

Oxygen content ($3 - \delta$)	Room temperature in air	1000°C under oxygen	1200°C under oxygen
$\text{LaCo}_{0.2}\text{Fe}_{0.8}\text{O}_{3-\delta}$	3.005 ± 0.010	3.005 ± 0.015	3.003 ± 0.010
$\text{La}_{0.8}\text{Sr}_{0.2}\text{Co}_{0.2}\text{Fe}_{0.8}\text{O}_{3-\delta}$	2.999 ± 0.003	2.992 ± 0.005	2.972 ± 0.003
$\text{La}_{0.6}\text{Sr}_{0.4}\text{Co}_{0.2}\text{Fe}_{0.8}\text{O}_{3-\delta}$	2.948 ± 0.009	2.908 ± 0.005	2.849 ± 0.006

The thermogravimetric results in the graph and table indicate that the Sr dopant induced the formation of more oxygen vacancies at lower temperature. It can be noted that $\text{LaCo}_{0.2}\text{Fe}_{0.8}\text{O}_{3-\delta}$ without dopant Sr was nearly stoichiometric from room temperatures up to 1,200°C.

Further results from the calculation of oxygen content on $\text{La}_{1-x}\text{Sr}_x\text{Co}_{0.2}\text{Fe}_{0.8}\text{O}_3$ with an x of 0, 0.2, and 0.4 at 1,200°C show that oxygen activity of 10^{-13} decreases the oxygen content of all three LSCF compositions significantly, down to the minimum oxygen content in the region of 10^{-15} to 10^{-16} . [75]

Teraoka et al. [76] measured the ionic (σ_i) and electronic (σ_e) conductivities of $\text{La}_{1-x}\text{Sr}_x\text{Co}_{1-y}\text{Fe}_y\text{O}_{3-\delta}$ separately and found that σ_i increased as the content of both Sr and Co increased, Sr content was more influential on σ_i . They also noted that σ_i increased significantly when x increases and that σ_i gradually decreased with increasing y , indicating that σ_i is primarily controlled by A-site composition [76].

The electrical conductivity of a $\text{La}_{0.8}\text{Sr}_{0.2}\text{Co}_{1-y}\text{Fe}_y\text{O}_3$ system studied by Tai et al. [74] as a function of the Co/Fe ratio and temperature in air showed that the σ_e of each composition (different y) increased with temperature. The temperature-dependent electrical conductivity reached about 200 S/cm with the composition of $y \geq 0.8$, and this conductivity is similar to that of $\text{La}_{0.8}\text{Sr}_{0.2}\text{FeO}_3$. Further study indicated that the unique temperature dependence of σ_e can be attributed to several factors, including high-temperature ionic compensation, the preferential electronic compensation of Fe over Co ions, and charge-disproportional Co ions.

Previous research has suggested that increasing the acceptor dopant concentration can increase the electronic conductivity and oxygen deficiency of LSCF and therefore improve the ionic conductivity and oxygen permeability [73].

The electrical conductivity of $La_{0.6}Sr_{0.4-z}Co_{0.2}Fe_{0.8}O_{3-\delta}$ ($0.00 < z < 0.025$) in air is shown in Fig. 2.9 as a function of temperature. The figure shows that the electrical conductivity σ_e was significantly affected by a change in Sr deficiency, z . The electrical conductivity decreased with increasing z except $z=0.01$. The maximum conductivity can be obtained when $z=0.00$ at a temperature around 773-873 K. Atsushi [72] explained that the decreases in electrical conductivity are due to a decrease in the concentration of the p-type electronic carriers by introducing Sr deficiency.

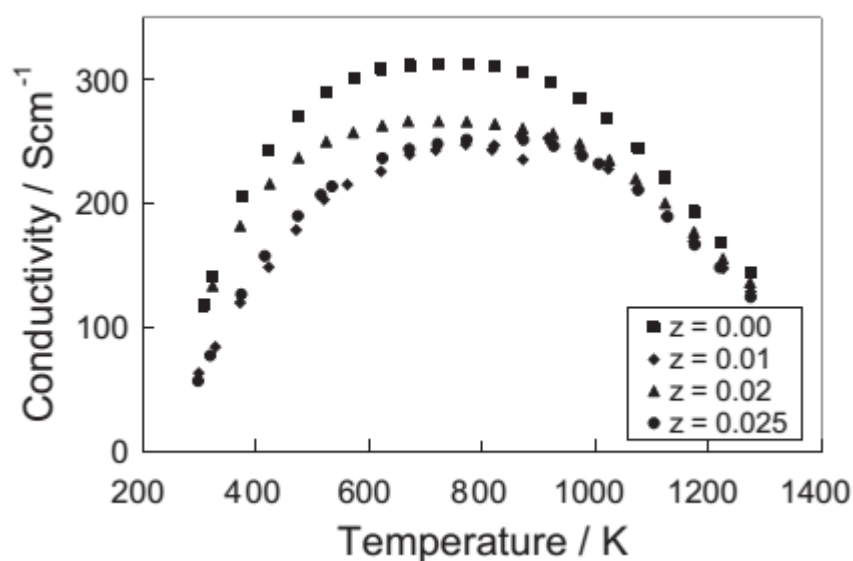


Figure 2.9 Electrical conductivity of $La_{0.6}Sr_{0.4-z}Co_{0.2}Fe_{0.8}O_{3-\delta}$ measured in air [72].

2.5 Porous membrane fabrication

A dual-phase membrane requires a certain porosity for carbonate infiltration; moreover, the pores must be connected. Pore formers are applicable for SOFCs-like solid oxide electrolytes. Ideally, a pore network should be formed that communicates from one membrane surface to the other. However, it is likely that enclosed pores will also be formed, which may affect mechanical strength.

There are four typical pore formers for increasing membrane porosity: polymethylmethacrylate (PMMA), potato/corn starch, ammonium oxalate, and ammonium carbonate. In addition, glassy carbon can be used, although the expense may

Chapter 2. Literature review

be prohibitive. The general process for pore former removal is simply combustion in air. Liu et al. tested the porosity of various pore formers in cathode substrates of prepared NiO-YSZ composite SOFCs; the results showed that, as the content of the pore former increased, the porosity of PMMA-mixed substrate increased from 14% to 58%, for potato starch, it was increased from 14% to 48%, for ammonium oxalate, it was increased from 4% to 46%, and for ammonium carbonate, it was increased only from 2% to 10% as measured by the Archimedes method [77]. The Archimedes method involves using a certain liquid to fill the pore network by capillary force and obtaining the volume of the pore network by measuring the volume of the liquid that filled the pores; the volume of infiltrated liquid can be calculated from the mass increase.

Porous $\text{Ca}_{0.8}\text{Sr}_{0.2}\text{Ti}_{0.7}\text{Fe}_{0.3}\text{O}_{3-\delta}$ (CSTF) supported thin film membranes were synthesised by Araki and used as an oxide ionic and electronic mixed conductor. It provided an alternative method to increase the porosity of the dense membrane by using ultrasonic agitation for CSTF powder and 0-30% carbon black in isopropanol for 1 hr and sintered at 1,423 K to remove carbon black. Pore sizes between 10 μm and 50 μm were measured by Hg porosimetry. The work indicated that porosity was improved by increasing the carbon black content; the maximum porosity was about 65% with the use of 30 wt% carbon black [78].

Etchegoyen et al. [79] developed asymmetric membranes with porous $\text{La}_{0.6}\text{Sr}_{0.4}\text{Fe}_{0.9}\text{Ga}_{0.1}\text{O}_{3-\delta}$ (LSFG) support by using large corn-starch particles (14 μm) as a pore-forming agent to form a connected porous structure. Magnesia (5 vol% grain size = 0.5 μm) was required to control the microstructure of the membrane. As Etchegoyen explained, the increases of magnesia particles also improved the oxygen permeability of LSFG dense membranes because magnesia inhibits the LSFG matrix phase grain growth. Thus, the porosity increased only by reducing the substrate particle size; however, the porosity was low (less than 30%) [79, 80].

Porous alumina ceramics with uni-directionally aligned cylindrical pores were reported by Isobe et al., prepared with the extrusion method by using Nylon fibres (30 vol.%) as a pore former. The results showed better gas permeability than conventional methods with an observed porosity of >34%. The original pores were formed by burning the fibre pore formers, and a small shrinkage was found after sintering. The average diameters of the Nylon fibres were 9.5-4.3 μm , and the length was 800 μm ; the pore

size was observed to be higher than those achieved by the conventional method, PMMA [81].

2.6 Membrane sealing at high temperatures

To successfully conduct the experiment using a ceramic membrane reactor, high-temperature sealing methods are required, and the principle is based on the application of inorganic sealing materials, which is the only way to create a seal at a typical high temperature over 600°C. There are three common methods to seal a dense or tubular membrane onto a support, and the figure below shows how to fill the gaps between the membrane pellet and the support with sealing materials. As Fig. 2.10 shows, the sealing material first needs to melt or soften at a certain temperature and fill the gaps between the membrane and the ceramic support, and then cooling is required to make the sealant become solid to completely seal the membrane.

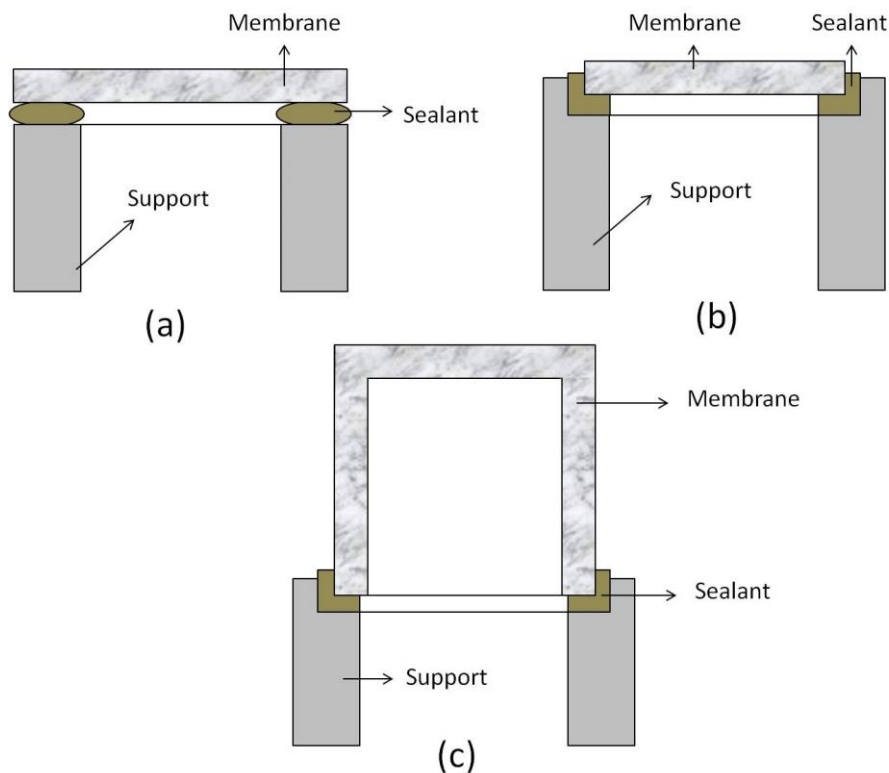


Figure 2.10 Schematic of the sealing of a typical membrane on a ceramic support [26].

Different sealing materials have been reported to seal a ceramic membrane; Ti-Au-Cu or Ni-Ag-Cu alloys have been used to seal a ceramic membrane to a dense tube metal substrate by brazing the alloy melt above the melting temperature [82] [83]. By doing

Chapter 2. Literature review

this, the sealing was permanently fabricated between the membrane and the support. However, the membrane cannot be easily replaced after experiments, and the alloy melt makes it difficult to wet the surface of the ceramic membrane and support during an experiment; the thermal extension of the alloys cannot match that of the membrane and support tube, which causes membrane cracking. Those disadvantages make the application of such technology difficult, and only a few researchers have sealed their membranes using this method.

Instead of permanent sealing materials, silver or gold pastes have also been used as sealing material because of their advantages of chemical inertness and durability at high operation temperatures [84, 85]. The membrane can be easily removed from the support after an experiment.

Soft inert metals like silver or gold have been used to seal membranes; similar to rubber O-rings, metal O-rings can be placed into the gap between a ceramic membrane and the support. To achieve gas-tight sealing, an external compression force needs to be applied, but it is difficult to design the reactor because of the high operating temperature; the external force may cause membrane cracking during heating or cooling [86-90].

Glasses or ceramic mixtures are also used as sealing materials; either paste or a ring can be applied, and during the heating process, the sealing materials liquefy, which can fill the gaps between the ceramic membrane and the support, and the sealant will be solid at a lower temperature [91, 92]. A glass sealant can wet the membrane surface and spread easily; however, the sealing will only work for a few hours because of interfacial leaking, and the liquid glass can be sucked into the pore network. The diffusion of the glass also causes error when calculating the flux.

Chapter 3 Methodology

3.1 Experimental equipment

The membrane reactor system presented below in Fig. 3.1 is used for a typical down-hill CO₂ permeation experiment. During the down-hill permeation process, CO₂ permeates from the high CO₂ partial pressure side to the lower CO₂ partial pressure side. For an up-hill CO₂ permeation process in which CO₂ permeates in the opposite direction, the same reactor system is used, but different cylinders are selected (Fig. 7.1).

In general, the reactor system consists of a reactor with a furnace, gas cylinders (depending on the experimental purpose), and a data analysis mass spectrometer (MSP) or gas chromatograph (GC) controlled by a computer.

3.1.1 Reactor

The membrane reactor is designed for working at high temperatures of up to 900°C at 1 atmosphere pressure and consists of a feed-side volume in the inner tube and a permeate side with a quartz shell outside. Both the feed and permeate sides have the inlet and outlet stream connected to the mass flow controller and mass spectrometer, respectively. These two sides are connected if there is no membrane sealed; the feed side and permeate side are isolated from each other with a well-sealed membrane at the top of the alumina tube support. However, gas leakage during permeation experiments creates a connection between the feed side and permeate side, and this could cause the experiment to fail. The volumes of the feed-side and permeate-side chambers are 11.5 cm³ and 250 cm³, respectively. The reactor is designed to be about 20 cm from the top shell to the bottom in length, and this reduces the temperature at the bottom of the reactor during high-temperature experiments and protects the O-ring at the bottom because only the reactor top is heated by a tube furnace. When the furnace heats the reactor to 900°C at the top, the reactor bottom temperature is about 60 to 70°C.

3.1.2 Gas cylinders

The type of cylinders and gases are selected depending on the experimental requirements. For the typical down-hill permeation experiments, the feed-side gas is provided by a gas cylinder with 50% CO₂ and 50% N₂, and the permeate side is fed by pure helium; the helium used here is a carrier gas that brings the CO₂ from the permeate side to the mass spectrometer for analysis. Both the feed- and permeate-side gas flow rates are 20 ml min⁻¹ (STP); the reason for setting the same flow rates for both chambers is the convenient calculation of CO₂ permeance and permeability. Moreover, the outlet of the mass spectrometer is a vacuum, so the mass spectrometer requires an inlet flow rate of at least 14 to 15 ml min⁻¹ (no vacuum for GC). However, a large flow rate cannot be used because the CO₂ permeate rate is limited and a large flow rate of helium to the permeate side could dilute the CO₂ significantly and the amount of CO₂ could be too small to be detected by the mass spectrometer (resolution 0.01%).

An oxygen cylinder with 20% O₂ balanced by argon is used in kinetic experiments in Chapter 6; the oxygen added to the feed side of the membrane was mixed with CO₂ and the total flow rate for the feed side was always constant at 20 ml min⁻¹. The CO₂ and O₂ volume percentage in the total 20 ml min⁻¹ gas flow can be controlled by mass flow controller 1 (MFC-1) and mass flow controller 2 (MFC-1). The permeate side of the membrane reactor is fed by a carrier gas (helium) at the same flow rate.

The up-hill CO₂ permeation experiments use different gas cylinders. One setup is 1% CO₂ fed to both the feed and permeate sides of the membrane and 20% oxygen added to the feed-side; another is 0.5% CO₂ fed to the feed side and 1% CO₂ to the permeate side, with 20% oxygen added to the feed side. The symmetrical condition was applied during the experiments, and the details are described in Chapter 7.

3.1.3 Data analysis

For the down-hill CO₂ permeation experiments, only outlet gas from the permeate side is delivered to the mass spectrometer for analysis because the CO₂ partial pressure difference between the feed and the permeate sides is significant, which is where the driving force arises from. The CO₂ in the mole fraction in the feed side is much greater than the CO₂ that crosses the membrane; in other words, the decreased (permeated) CO₂ mole fraction (about 0.6) is tiny compared to the CO₂ in the feed side (50%). The typical down-hill CO₂ permeation experiments use 50% CO₂ in the feed side, and only

about 0.6% of a 20 ml min⁻¹ gas flow can permeate across the membrane. The mass spectrometer is calibrated and used to measure CO₂ only in the permeate side when conducting down-hill experiments.

Up-hill permeation experiments use two mass spectrometers, one for each side; these two mass spectrometers are in the same condition and calibrated using the same standard gas cylinders. The error range and detailed experimental parameters are presented in Chapter 7.

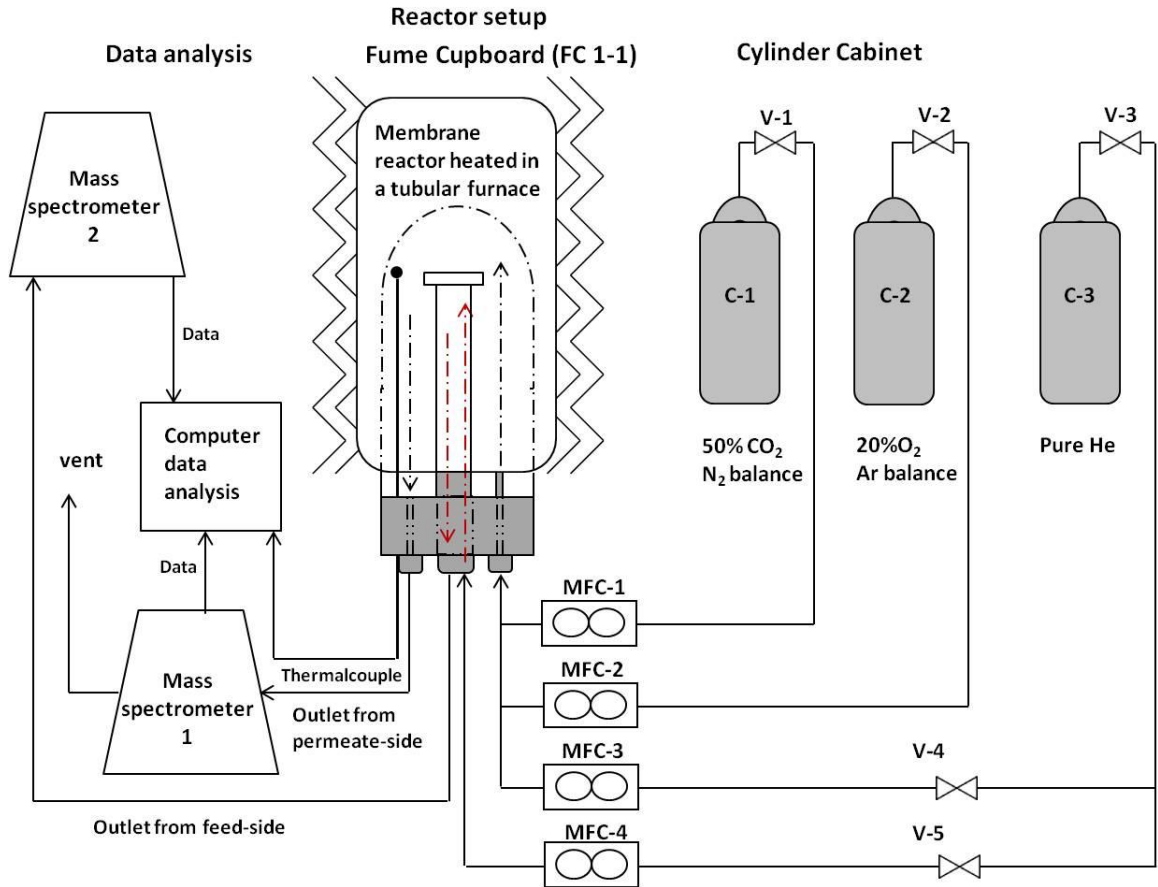


Figure 3.1 Permeation cell apparatus comprising a gas supply and feed control, membrane module, and furnace.

The permeance of carbon dioxide across the membrane ($\text{mol m}^{-2} \text{s}^{-1} \text{Pa}^{-1}$) based on CO₂ driving force is defined as follows:

$$\text{Permeance} = \frac{\text{mol}\% \times 20 \text{ ml/min}}{22400 \text{ ml/mol}} \times \frac{1}{0.5 \times 10^{-4} \text{ m}^2} \times \frac{1}{60 \text{ s/min}} \times \frac{1}{P_{a''}(\text{CO}_2) - P_{a'}(\text{CO}_2)}$$

The permeance of oxygen across the membrane ($\text{mol m}^{-2} \text{s}^{-1} \text{Pa}^{-1}$) based on the oxygen driving force is defined as follows:

$$\text{Permeance} = \frac{\text{mol}\% \times 20 \text{ ml/min}}{22400 \text{ ml/mol}} \times \frac{1}{0.5 \times 10^{-4} \text{ m}^2} \times \frac{1}{60 \text{ s/min}} \times \frac{1}{P_{a''}(\text{O}_2) - P_{a'}(\text{O}_2)}$$

Chapter 3. Methodology

where $P_{a'}'(\text{CO}_2)$ and $P_{a'}(\text{CO}_2)$ are the partial pressure of carbon dioxide in the permeate side and feed side and $P_{a'}'(\text{O}_2)$ and $P_{a'}(\text{O}_2)$ are the partial pressure of oxygen in the permeate side and feed side.

Chapter 4 Membrane fabrication and characterisation

4.1 Introduction

This chapter focuses on analysing the pore network, which is important for molten metal carbonate infiltration. To determine the maximum pore size for holding a certain amount of molten phase carbonate, a simple model is described based on the surface tension of molten potassium carbonate and water (the Archimedes method) (Section 4.2). The reason for doing this is that the liquid carbonate can be easily held by small pores according to the capillary force that arises from the surface tension of the liquid. The size of the pores depends on the particle size of the pore former used to create porosity during membrane sintering at high temperatures. The model is also used to estimate the volume of the pore structure in the membrane and comes out with porosity. A fresh host porous membrane substrate was sintered from LSCF by pore former combustion to create porosity at high temperatures; because membrane materials sintered at high temperatures are always dense (1,250°C) and have high mechanical strength, different amounts of pore former were tested considering both porosity and mechanical stability. Section 4.3 introduces the method of fabricating a partially sintered membrane with a porous structure at the relatively low temperature of 900°C in such a way that no pore former was applied, and this method is generally used by Lin's group [25, 29, 93]. Section 4.4 describes the method of fabricating a fully sintered membrane substrate with a porous structure using pore formers, and three typical carbon-based pore formers are introduced; the selection of the pore former was made by the resulting membrane structure, and the membrane sintered in the selected way was used for the kinetic experiment and the up-hill permeation experiment.

4.2 Model for pore size estimation

4.2.1 Surface tension

For a liquid, surface tension is the contractive tendency to resist a force on the tangent line of the interface between the liquid and the air. At the air-liquid interface, because of the cohesion of the water molecules, the water overcomes the force that causes them to

Chapter 4. Membrane fabrication and characterisation

attract air molecules. Another explanation is that, because the liquid molecules at the surface are rare and thin, the attraction of water molecules is greater than the repulsive force; the resulting force is attraction that is parallel to the surface. For a liquid drop system, applying work to the system increases thermodynamic energy to equal the volumetric work and surface work. Thus, the surface tension (N m^{-1}) can be expressed as surface Gibbs free energy (J m^{-2}). The surface tension of a solution can be calculated using the following equation:

$$\sigma V_m^{2/3} = k (T_c - T - 6.0) \quad (4.1)$$

where V_m is molecular volume, K is the gas constant, T_c is critical temperature, and σ is the surface tension.

For practice, using molten salts at high temperatures with no water content, the surface tension can be obtained from the following empirical equation:

$$\sigma_s(T) = c_1 + c_2 T \quad (4.2)$$

The thermodynamic parameters c_1 and c_2 for molten potassium carbonate can be obtained from the literature [94]. For potassium carbonate at its melting point,

$$\begin{aligned} \sigma_s(1172.15) &= 243.17 + (-0.06368) \times 1172.15 \\ &= 0.169 \text{ N m}^{-1} \end{aligned}$$

4.2.2 Pore size estimation

Assuming that the molten carbonate fills the pores of the membrane by capillary force, the pore was considered an ideal micro tube, as Fig. 4.1 shows. The force from the surface tension of liquid towards the boundary of the tube and liquid is expressed as f ; the surface A-B is horizontal when surface A-B is balanced so that external pressure from the atmosphere equals the pressure from the inner liquid, as shown in Fig. 4.1(a). If the supplementary pressure P_s is the same direction as the external pressure P_o , the surface A-B will be convex, as shown in Fig. 4.1(b); the cooperating force is downward. If the supplementary pressure is upward and higher than the external pressure, the liquid tends to go up towards the tube.

Chapter 4. Membrane fabrication and characterisation

For molten potassium carbonate, the liquid carbonate needs to infiltrate the pore, as shown in Fig. 4.1(a) and (c). In the case of Fig. 4.1(b), the liquid tend to leave the tube (downward). In the case of Fig. 4.1(a), the liquid has stopped moving and is steady.

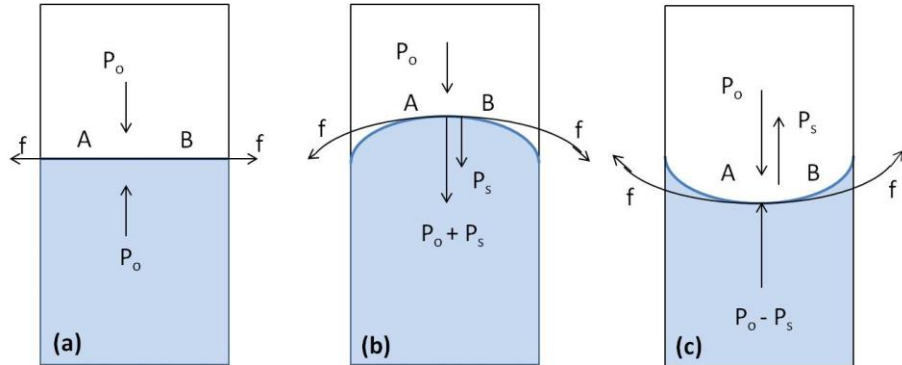


Figure 4.1 External pressure on the curved surface of a liquid. (a) Equilibrium state; (b) cooperating force towards the liquid (downward); (c) cooperating force towards the air (upward) [95].

From the perspective of physical chemistry, the system can be described as a drop of liquid connected to the end of a micro-tube (capillary), as in Fig. 4.2. The supplementary pressure P_s is towards the centre of the curved surface of the liquid (ignoring gravity). The total pressure on the liquid drop can be expressed as follows:

$$P = P_o + P_s \quad (4.3)$$

The supplementary pressure P_s comes from the surface tension of the liquid drop, and the work from the system on the liquid drop equals the change of the surface Gibbs free energy of the liquid drop. Hence, the following equation can be obtained:

$$P_s dV = \sigma_s dA_s \quad (4.4)$$

$$\text{The surface area of the liquid drop is } A_s = 4\pi R^2 \quad (4.5)$$

$$\text{The volume of the liquid drop is } V = \frac{4}{3}\pi R^3 \quad (4.6)$$

$$\text{Thus, } dA_s = 8\pi R dR \quad (4.7)$$

$$\text{and } dV = 4\pi R^2 dR \quad (4.8)$$

According to Equations 4.4, 4.7, and 4.8, the supplementary pressure P_s can be expressed as follows:

$$P_s = \frac{2\sigma_s}{R} \quad (4.9)$$

Chapter 4. Membrane fabrication and characterisation

For a concave surface, the radius R will be negative, which is the radius of the micro-tube, as shown in Fig. 4.3(a).

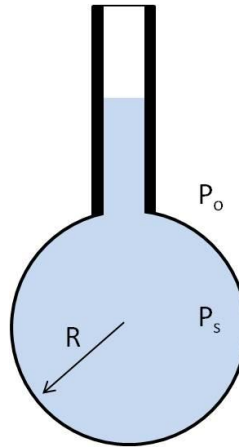


Figure 4.2 Supplementary pressure from a curved surface

The liquid column shown in Fig. 4.3(a) will rise until it reaches the equilibrium state shown in Fig. 4.1(a).

$$\text{Thus, } \Delta P = P_s = \frac{2\sigma_s}{R} = \Delta\rho gh \quad (4.10)$$

Assuming that the density of molten potassium carbonate ρ equals that of the solid potassium carbonate, the density of air at high temperatures can be ignored compared to that of potassium carbonate.

The height of the liquid column in the micro-tube can be obtained by the following:

$$h = \frac{2\sigma_s}{R\rho g} \quad (4.11)$$

Assuming that the membrane thickness is 2 mm (that is, $h = 0.002$ m), the maximum pore radius (not considering the contact angle) can be obtained:

$$R_{pore} = \frac{2\sigma_s}{h\rho g} = \frac{2 \times 0.169}{0.002 \times 2.429 \times 10^3 \times 9.8} = 7 \times 10^{-3} \text{ m} = 7 \text{ mm}$$

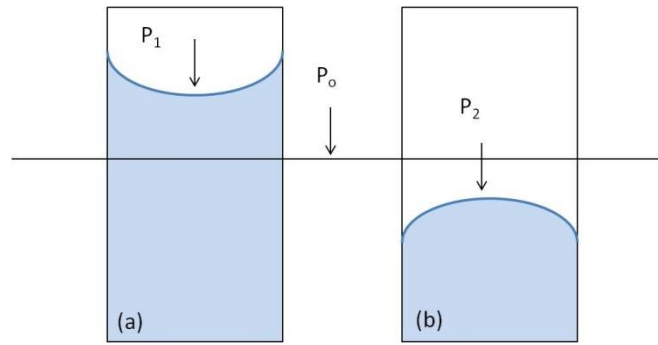


Figure 4.3 Height of a liquid column under supplementary pressure. (a) Liquid column tends to go up; (b) liquid column tends to go down.

If the contact angle θ is considered, Equation 4.11 can be expressed as follows:

$$h = \frac{2\sigma_s}{R\rho g} \cos \theta \quad (4.12)$$

The contact angle θ for the molten alkali metal carbonate is a function of temperature. As the literature [96] has shown, θ is 41° at a temperature of 550°C , 33° at a temperature of 636°C , and 14° at a temperature of 740°C and decreases with increasing temperature. Therefore, the value of $\cos \theta$ is 0.75 at a temperature of 550°C and 0.97 at a temperature of 740°C ; that is, the value range of $\cos \theta$ is between 0.75 and 0.97 when the temperature is between 550°C and 740°C (radius=5.2 mm at 550°C ; radius=6.7 mm at 740°C). Accordingly, the $\cos \theta$ will not change the magnitude of the pore radius or diameter result calculated above. The pore radius is estimated to be the average value of 5.2 mm and 6.7 mm, which is about 6.0 mm if the membrane working temperature is around 600°C .

The maximum pore radius inside the membrane for potassium carbonate infiltration is considered to be 6.0 mm. Assuming that the pore is cylinder-shaped, the diameter will be 12.0 mm. To obtain a continuous molten carbonate phase, the amount of carbonate powder that can fully fill the pores needs to be estimated before membrane infiltration (Fig. 4.4).

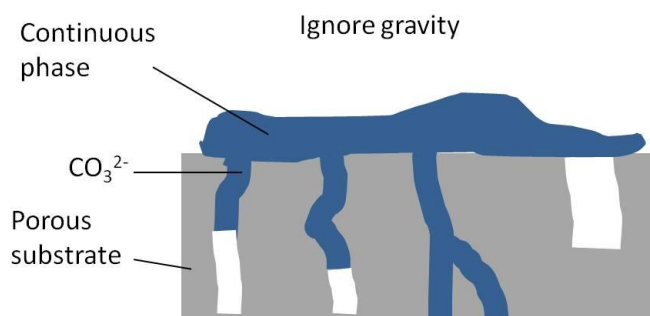


Figure 4.4 Scheme of a porous membrane with a continuous molten carbonate phase.

4.3 Partially sintered membrane fabrication and characterisation

4.3.1 General preparation of porous host MIEC membranes

Commercial powders of $\text{La}_{0.6}\text{Sr}_{0.4}\text{Co}_{0.2}\text{Fe}_{0.8}\text{O}_{3-\delta}$ (LSCF6428) and $\text{La}_{0.2}\text{Sr}_{0.8}\text{Co}_{0.8}\text{Fe}_{0.2}\text{O}_{3-\delta}$ (LSCF2882) supplied by Praxair were used. Approximately 2 g of powder was placed into a 20 mm diameter stainless steel die and pressed to 3 MPa for 1 minute by an automatic hydraulic press. The LSCF6428 and LSCF2882 pellets were sintered in a box furnace in air for 24 hours at 900°C (ramp rate of 2°C min⁻¹) to produce porous LSCF6428 and LSCF2882 substrates.

4.3.2 Carbonate salt infiltration

(a) Surface application followed by heating

Membranes with a molten-carbonate phase (Li/Na/K with corresponding mol%; 42.5/32.5/25) were prepared by melting ground powders of eutectic mixtures on the surface of LSCF6428 and LSCF2882 disk membranes followed by heating in a split tube-furnace at 520°C for 1 hour in non-circulating air to obtain LSCF6428 and LSCF2882 dual-phase membranes. The temperature was monitored using a k-type thermocouple.

(b) Mixing carbonate salt and host membrane powder

A well-mixed ground powder of potassium carbonate and LSCF2882 (1:0.8 weight ratio) was placed into a 20 mm diameter die, pressed by hand, and sintered at 900°C in a box furnace for 12 hours (ramp rate of 2°C min⁻¹) to obtain LSCF2882 dual-phase membranes.

The average pore size (radius) and pore size distribution of the supports sintered at 900°C were measured by mercury porosimetry from Imperial College. An SEM (scanning electron microscope) was used to characterise the appearance of the surface area of membranes. EDS (energy-dispersive X-ray spectroscopy) was used to characterise the element of each component but was not sensitive to carbon and also could not be used for quantity measurement but could show the relative amount of alkali metal sodium and potassium for comparison.

4.3.3 Characterisation of results and discussion

SEM images of porous LSCF2882 membrane substrates were pressed with a 20 mm diameter die and sintered at 900°C for 24 hours at a ramp rate of 1°C min⁻¹. Fig. 4.5 shows that the LSCF2882 pellet has connected particles on the surface, while the LSCF6428 pellet simply has gathered particles on the surface.

The porosity of LSCF2882 measured by Hg porosimetry was 29.35%, while LSCF6428 has less porosity (4%). In addition, LSCF2882 had higher Sr and Co content than LSCF6428, which can increase the oxygen ionic (σ_i) conductivity of the membrane, though Sr had a greater contribution [97]. Considering porosity, sintering temperature, and high oxygen ionic conductivity, LSCF2882 was selected as the dual-phase membrane substrate material. However, this material was identified as having low mechanical stability, which may be one of the factors that causes cross-chamber leaking through the membrane. This will be improved in future work.

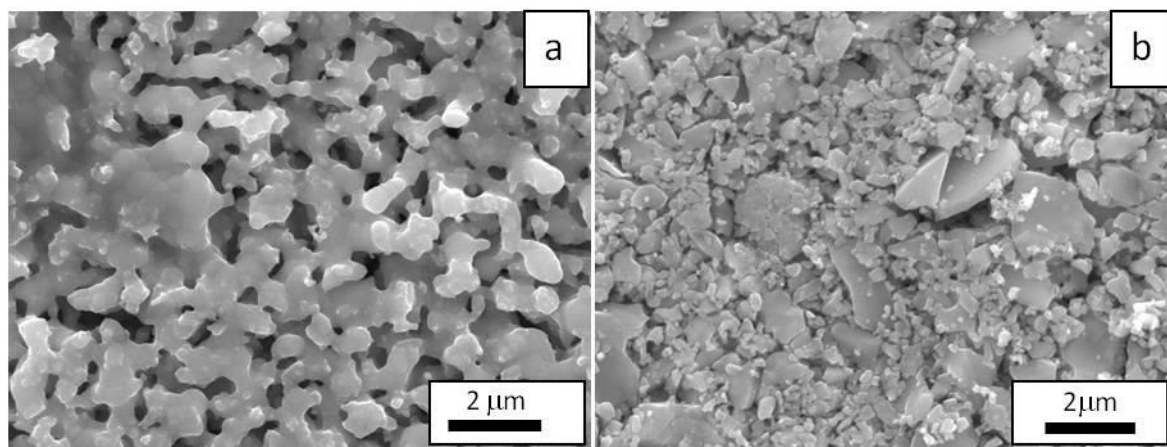


Figure 4.5 SEM images of fresh porous membrane substrates sintered at 900°C. (a) Surface of an LSCF2882 membrane; (b) surface of an LSCF6428 membrane.

Chapter 4. Membrane fabrication and characterisation

The molten carbonates (Li/Na/K 43.5/31.5/25 mol% eutectic mixtures) were mixed and ground in a mortar and pestle and then placed on top of the porous membranes to form a thin, solid layer to cover the top surface of the membranes; the LSCF2882 and LSCF6428 pellets were placed in a box furnace and heated to 520°C at 2°C min⁻¹ and then held for 20 minutes at 520°C. The eutectic mixture was expected to become viscous at 520°C and fill the pores of membranes at the surface; under gravity, the molten carbonates can then infiltrate the porous host membrane. EDS analysis on the surface of carbonate intrusion was carried out (Fig. 4.6). It was found that the Sr and Co content in LSCF2882 was higher than in LSCF6428, but it had lower Fe and La, which confirmed the formula for LSCF composite. The carbon and potassium signal on the LSCF2882 surface was higher than that of LSCF6428. For EDS technical reasons, Li cannot be detected and characterised using EDS analysis, and it is also not very sensitive to carbon signals.

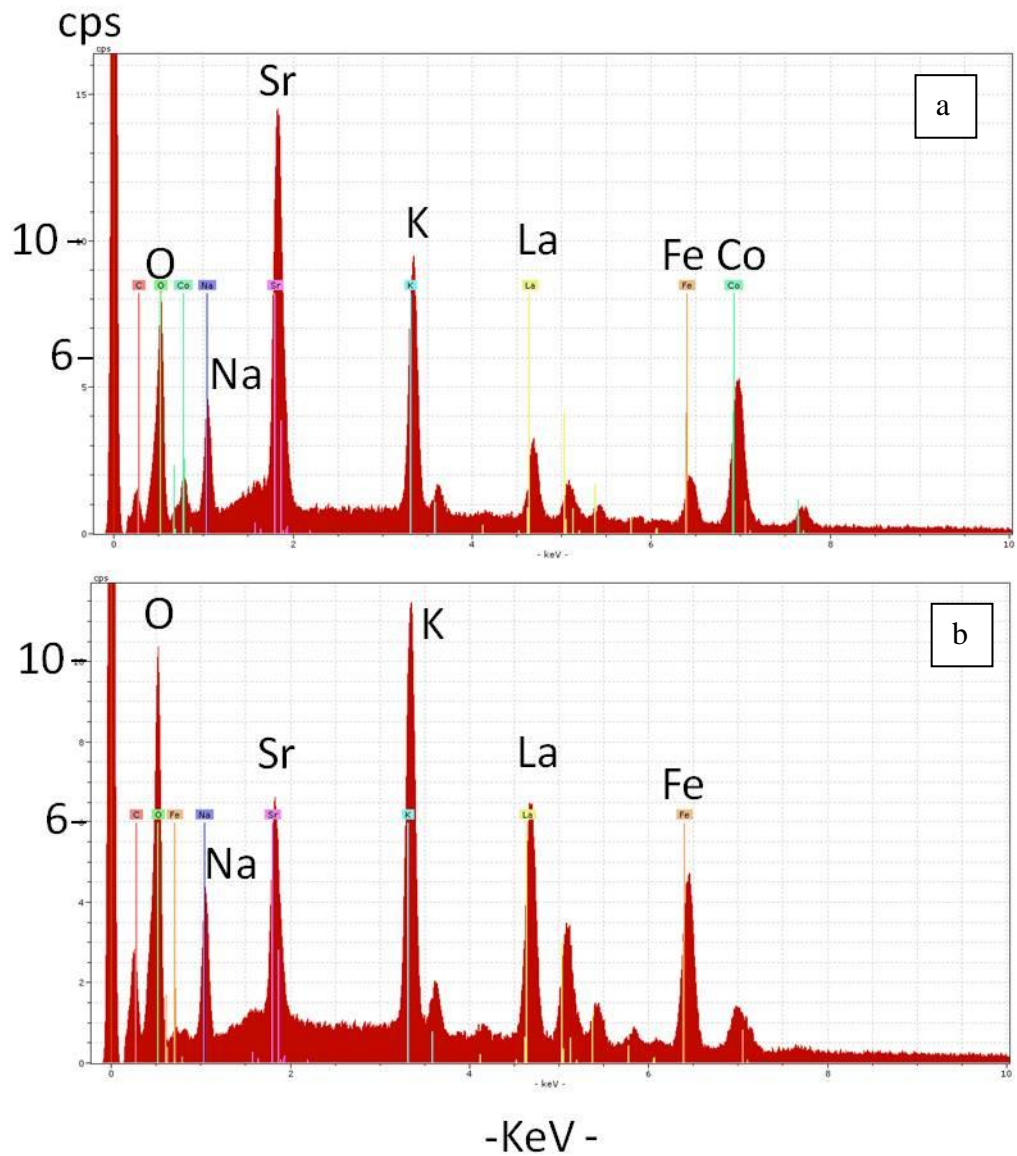


Figure 4.6 EDS analysis of carbonates (Li, Na, K in a 42.5:32.5:25 mol ratio) – infiltration on the surface of an LSCF membrane; molten carbonates infiltrated at 520°C. (a) LSCF 2882 membrane; (b) LSCF 6428 membrane.

LSCF2882 pellets with carbonate infiltration at temperatures of 520°C, 600°C, 700°C, and 800°C were obtained. Fig. 4.7 shows that a layer was formed on the surface of the membrane when carbonates infiltrated at 600°C and 700°C, respectively, which indicated that the molten carbonates were not fully infiltrated into the pores of the membrane. In addition, the molten carbonates were not dispersed sufficiently on the surface at 520°C. There was no such layer on the surface when carbonates infiltrated at 800°C.

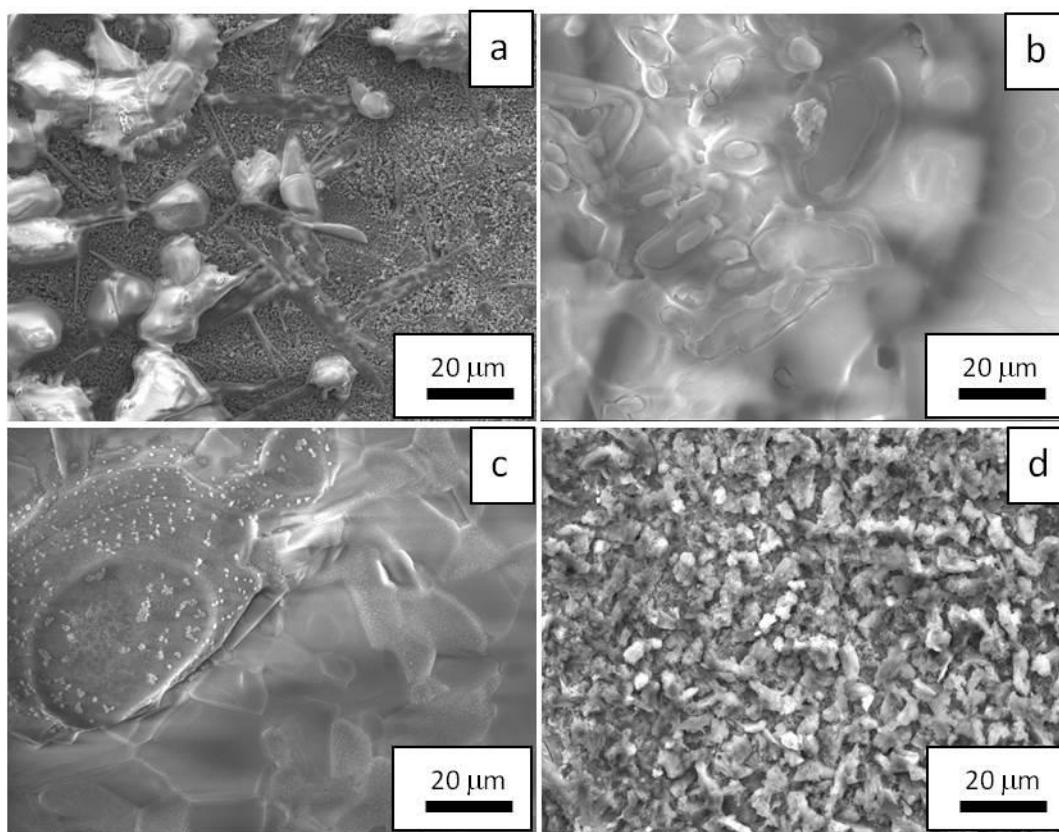


Figure 4.7 SEM images of LSCF2882 membranes on the surface of molten carbonates' (Li, Na, K in a 42.5:32.5:25 mol ratio) infiltration side. (a) 520°C carbonate infiltration; (b) 600°C carbonate infiltration; (c) 700°C carbonate infiltration; (d) 800°C carbonate infiltration.

The infiltration of carbonate was checked by cross-section analysis. High carbonate content can be detected at the edge of the cross-section area, with the noise signal shown at the very beginning of graph a in Fig. 4.8. The results show the distance from the infiltrated surface to depths of approximately 400 μm (700°C) and 500 μm (800°C); the alkali metal ions at 800°C infiltration are higher and decreased more slowly according to the distance than those of 700°C infiltration. It can be estimated that a higher temperature is better for alkali ion distribution inside the membrane, but the carbon signals from both 700 and 800°C have no large differences; this may have been because of the low sensitivity of EDS for carbon signals.

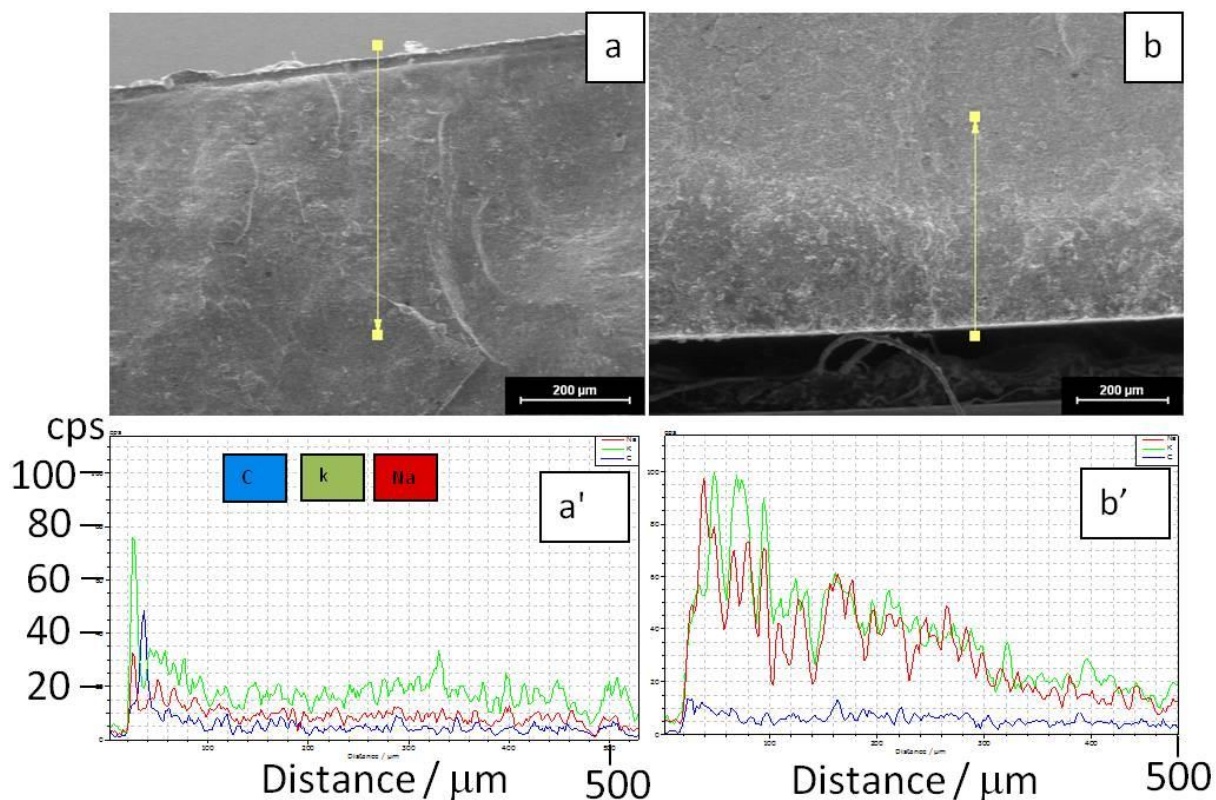


Figure 4.8 EDS analysis of a cross section of carbonate-infiltrated LSCF2882 membrane. (a) 700°C infiltration; (b) 800°C infiltration.

4.4 Fully sintered membrane fabrication and characterisation

4.4.1 Porous structure sintering and infiltration test

The LSCF membrane sintered at 1,250°C showed a dense structure with relatively high mechanical strength compared to that sintered at a lower temperature, which showed certain porosity. To fabricate a porous membrane substrate with high porosity and small pore size, pore former must be applied to create porosity during membrane sintering; the pore size mainly depends on the size of pore former particles, and the porosity depends on the amount of pore former that has been mixed with the membrane materials. Carbon black (Alfa Aesar 50% compressed), graphite (Alfa Aesar), and cornstarch (Sigma-Aldrich) were selected and tested. The membrane material to be tested to fabricate a porous structure was LSCF6428 powder (Alfa Aesar).

The method used membrane materials mixed with the pore former materials in various ratios, which were compressed by an automatic ATLAS T25 uniaxial press (3 tonnes applied). Subsequently, the pellets were sintered in air by ramping their temperature

from room temperature to combustion temperature, holding it for 0.5 to 2 hours, and the ramping the temperature to sintering temperature, which was 1,250°C, at 1°C min⁻¹ for 8 hours of sintering. Different pore formers need different temperatures to combust, and the actual temperature to be used also depends on experience. For carbon black and graphite, the temperature was increased at 1°C min⁻¹ directly to 1,250°C, and the carbon black and graphite are combusted during heating. A cornstarch-mixed membrane would be held at 200°C for 2 hours because the cornstarch burns at low temperatures of about 200°C. Continuing to increase the temperature will cause the membrane to crack, but for carbon black and graphite, there are no such problems.

4.4.2 Carbon black and graphite

Carbon black particles are very small, the typical diameter being about 100 nanometres; they are easy to combust owing to the significantly large surface area. Graphite particles are different they are large compared to carbon black, and the typical length of the graphite is 100 micrometres (Fig. 4.9).

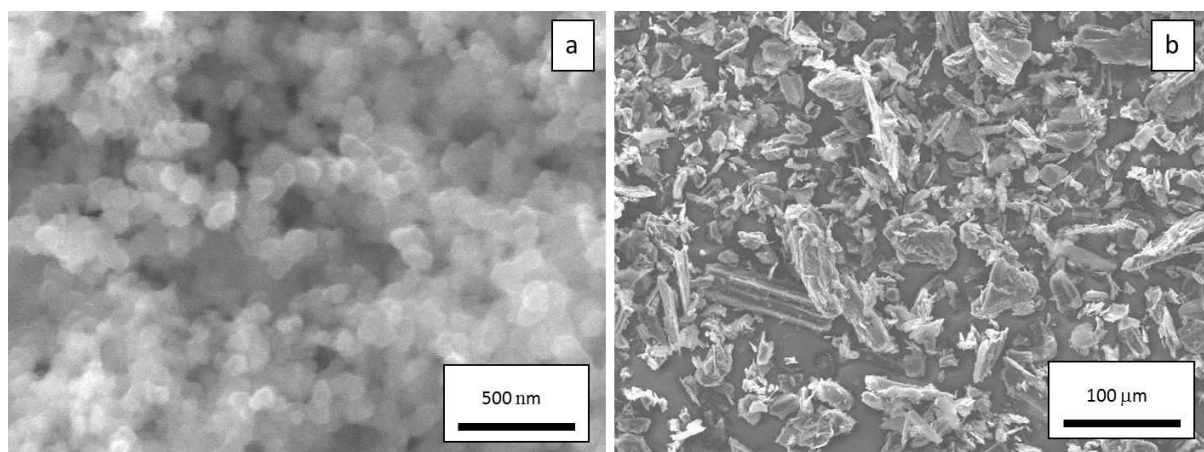


Figure 4.9 SEM images of pore former particles: (a) carbon black; (b) graphite.

Before synthesising the membrane, it was assumed that a pore former with a large particle size would result in relatively larger pore size, although there are other factors that affect the pore size.

Carbon black and graphite were mixed and ground with LSCF powders separately at a weight ratio of 1:4, and the membrane was sintered at 1,250°C for 8 hours. The cross section of the membrane was analysed by SEM; the results are shown in Fig. 4.10. The figure shows that the pores were not well distributed; the cross-section image a in Fig. 4.10 shows that large pores and micro-pores are mixed together and that many layers were formed, while image b shows the cross section formed by using graphite particles.

Chapter 4. Membrane fabrication and characterisation

It has more large pores than those formed by carbon black particles, and there are some dense parts in this cross section.

The results show an inhomogeneous pore structure, which indicates a problem in the mixing process. To solve this problem, it is necessary to determine how the particles of pore former and LSCF mixed and caused the inhomogeneous structure.

One explanation is that same-charged particles during mixing create a repulsive force and causes the ceramic and pore former particles to separate from one another (the particles were mixed in a plastic bottle installed in an electric shaker). However, compared with graphite, carbon black is a better pore former because of the pore size and structure.

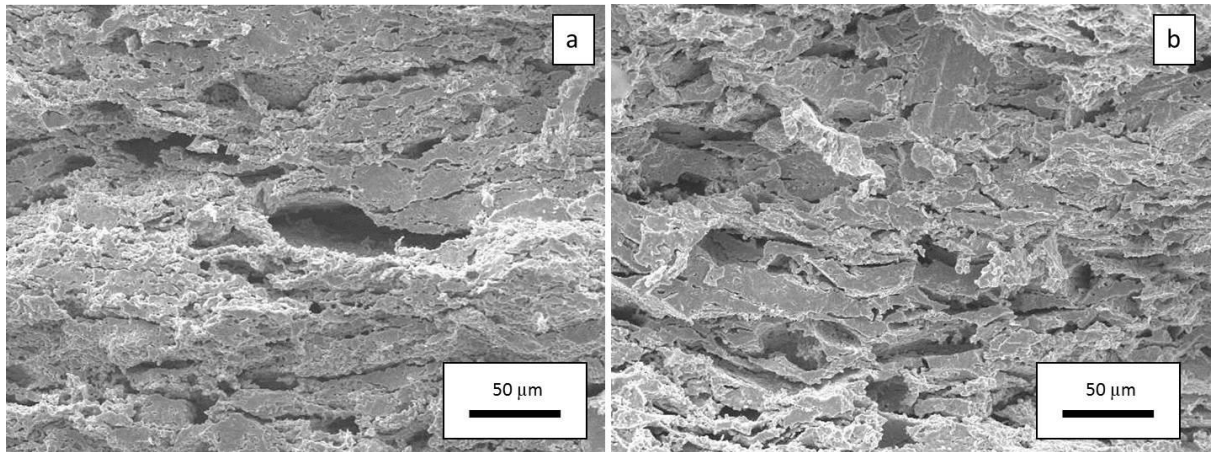


Figure 4.10 SEM images of sintered LSCF6428 membranes fabricated from mixing with pore formers. (a) Cross section of the membrane formed by using carbon black; (b) cross section of the membrane formed by using graphite.

4.4.3 Cornstarch

The cornstarch particles were about 10 micrometres diameter and round in shape (Fig. 4.11); it is a typical pore former and a non-electron conducting material, which could help in pore distribution. Another advantage is that cornstarch is a non-toxic and environmentally friendly material.

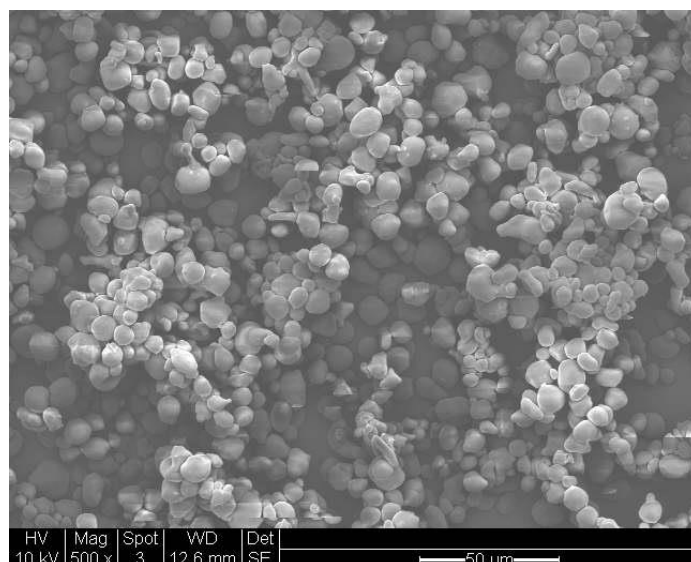


Figure 4.11 SEM images of cornstarch particles.

From the experience of many tests, the best LSCF-cornstarch membrane can be fabricated by using 0.5 grams of cornstarch well mixed with 1.5 grams of LSCF powder and pressed at 3 tonnes; the membrane needs to be heated to 200°C at a ramp of 1°C min⁻¹ and held for 0.5 to 1 hour to burn out the cornstarch and create pores, followed by ramping to 1,250°C at 1°C min⁻¹ for sintering the membrane. The membranes easily cracked during heating and the pore former combustion process. According to the results shown in Fig. 4.12, the structure of the membrane with a uniform pore network is appropriate for further application. The results show that the expected structure was achieved.

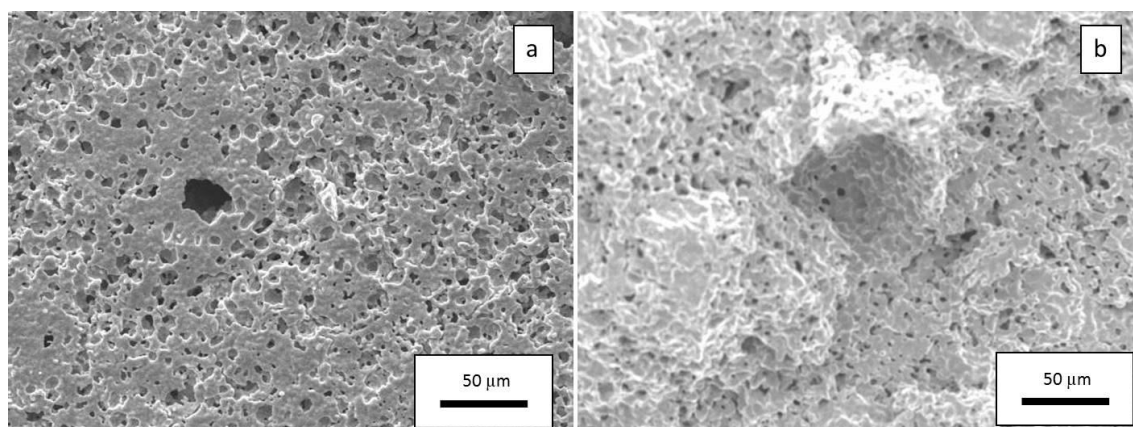


Figure 4.12 SEM results for an LSCF6428 membrane sintered by mixing with cornstarch. (a) Surface area of the membrane; (b) cross section of the membrane.

4.4.4 Infiltration test and pore volume estimation

The ideal host membrane with a porous structure needs to have high porosity and a small pore size to obtain a large interface area where the liquid phase carbonate can contact well with the membrane substrate; the interface area is critical for carbon dioxide separation, as the membrane substrate or carbonate alone cannot perm-selectively separate carbon dioxide.

To estimate the porosity of the fabricated membrane, the membrane needs to be infiltrated with deionised water, and the volume can be easily calculated by the weight increase of the membrane, which indicates that the water has been absorbed by the membrane. During the water infiltration, the water drops contacted the membrane surface and was sucked in immediately by the membrane until it fully infiltrated and the water drops were no longer sucked in by membrane and stayed at the surface; the water infiltrated into the membrane was considered to consume the whole pore volume, and the volume of the water in the membrane was considered the pore volume. The average pore volume of the membrane fabricated by mixing 1.5 grams of LSCF6428 with 0.5 grams of cornstarch was estimated to be 0.12 cm^3 , while the host porous membrane was about 0.35 cm^3 . Therefore, the porosity of the membrane was about 34%.

The volume of pores in the membrane can vary depending on the weight percentage of the pore former added to the membrane powder before sintering; however, a membrane sintered with too much pore former will have many cracks on the surface of the membrane and even become fragmented. The cornstarch weight percentage that can fabricate LSCF6428 membranes with a uniform pore structure using this method was found to be 25%. The experiments also showed that 30% cornstarch may work and that the resulting membrane may not crack in some cases, but to ensure that we can obtain a homogeneous membrane, 25% cornstarch is the best choice.

In comparison with cornstarch-LSCF membranes, carbon black-LSCF membranes are not easy to crack, but the structure is worse than that of cornstarch-LSCF membranes; carbon black added in an LSCF6428 membrane can create a very porous membrane with about 60% porosity. The pore volume also depends on the weight percentage of carbon black pore formers. According to the results shown in Fig. 4.13, the pore volume of the membrane is a function of the applied pore former .

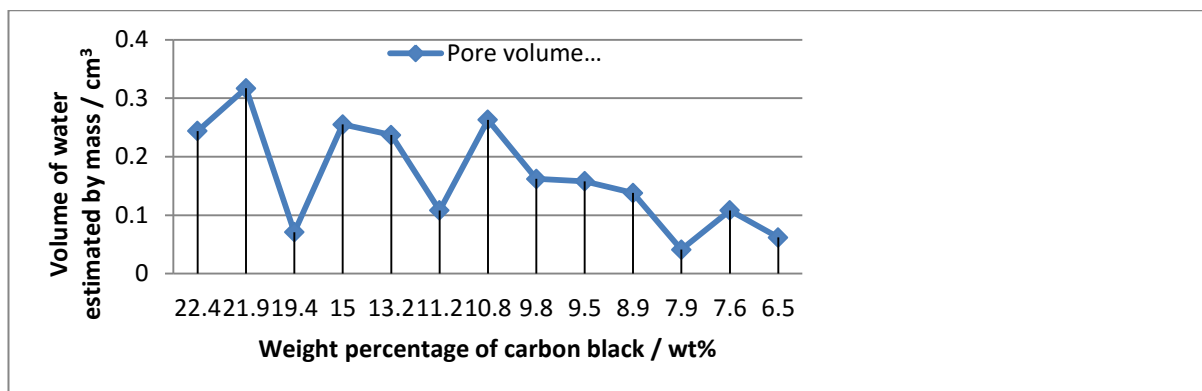


Figure 4.13 Pore volume estimation according to water intrusion for carbon black applied to an LSCF6428 membrane.

Table 4.1 LSCF6428 membrane with cornstarch applied; green: 2.188 g, sintered: 1.624 g

Infiltration	Carbonate added (g)	Increase measured (g)	Membrane weight (g)
1 st	0.0355	0.0338	1.6578
2 nd	0.0367	0.0350	1.6928
3 rd	0.0322	0.0298	1.7226
4 th	0.0305	0.0297	1.7523
5 th	0.0460	0.0430	1.7953
6 th	0.0298	0.0276	1.8229
7 th	0.0315	0.0306	1.8535
8 th	0.0305	0.0259	1.8794
Total	0.2727	0.2554	+15.72wt%

Table 4.2 YSZ membrane with cornstarch applied; green: 2.400 g, sintered: 1.594 g

Infiltration	Carbonate added (g)	Increase measured (g)	Membrane weight (g)
1 st	0.0442	0.0428	1.6368
2 nd	0.0492	0.0457	1.6825
3 rd	0.0317	0.0297	1.7122
4 th	0.0325	0.0330	1.7452
5 th	0.0371	0.0328	1.7780
6 th	0.0330	0.0295	1.8075
7 th	0.0327	0.0316	1.8391
8 th	0.0294	0.0270	1.8661
Total	0.2898	0.2721	+17.07wt%

4.4.5 The typical LSCF membrane preparation and porosity used in the project

Commercial $\text{La}_{0.6}\text{Sr}_{0.4}\text{Co}_{0.2}\text{Fe}_{0.8}\text{O}_{3-\delta}$ (LSCF6428) powder was purchased from Praxair. The powder was synthesised by combustion spray pyrolysis, resulting in powders with a particle size of less than 1.1 μm . The pellets were formed by uniaxial pressing of approximately 1.5 g of the LSCF powder mixed with 0.5 g of cornstarch (Sigma-Aldrich) at 3 tons using an automatic ATLAS T25 uniaxial press. Subsequently, the pellets were sintered in air by ramping their temperature from room temperature to 200°C at 1°C/min and holding at 200°C for 2 hours (so that cornstarch burn-out and pore formation occurs) and then ramping the temperature to 1,250°C at 1°C/min and holding this temperature for 12 hours, followed by slow cooling to room temperature at 1°C/min. The diameter and the thickness of the sintered pellets were approximately 15.5 mm and 1 mm, respectively, after being polished using SiC paper. The average pore size (radius) and pore size distribution of the LSCF substrate sintered at 1,250°C were measured by mercury porosimetry at Imperial College (porosity: 47% approx., average pore size: 600-700 nm). The porosity-radius diagram from mercury porosimetry data (raw data in Appendix C) is shown in Fig. 4.14.

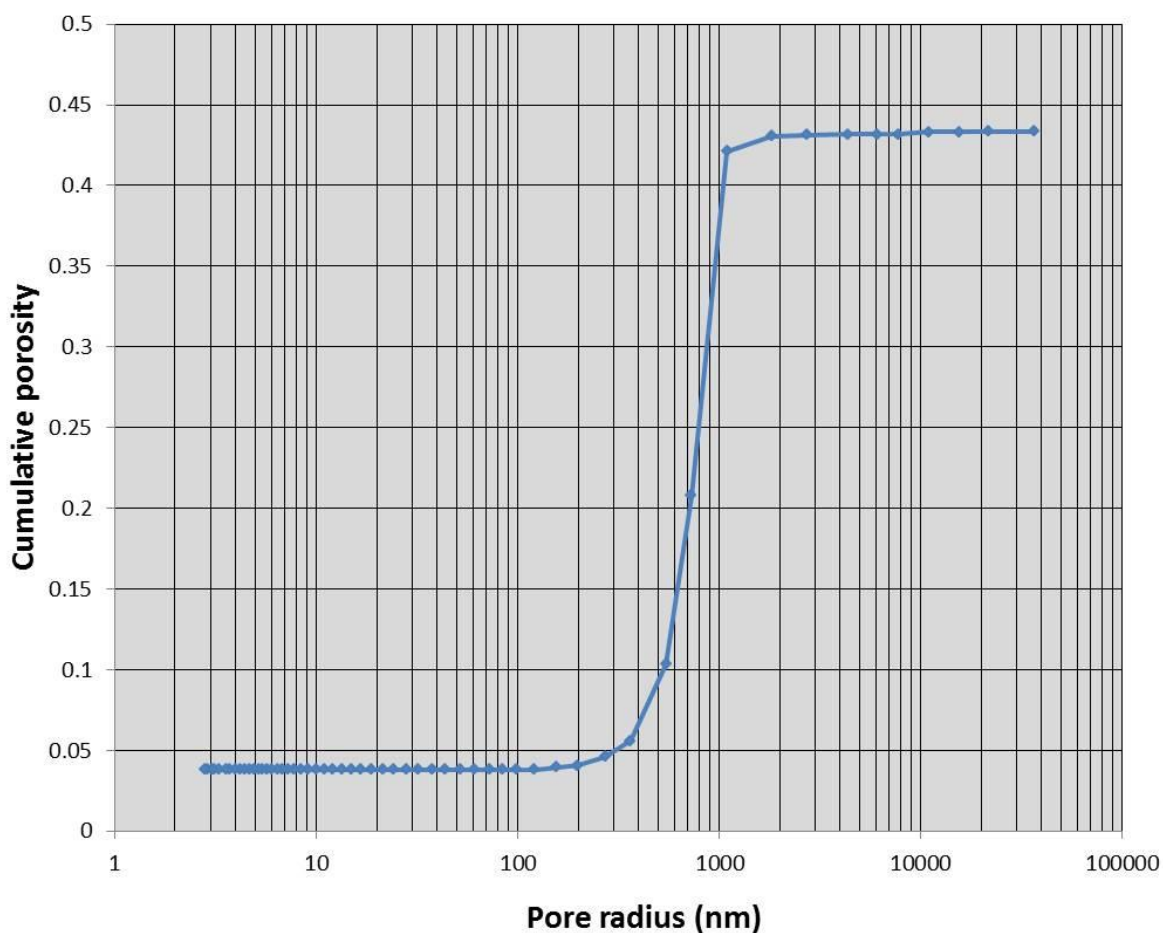


Figure 4.14 Cumulative porosity as a function of pore size. The mean pore diameter is 667 nm and the corrected porosity is 47.8%. The raw data for Hg injection are presented in Appendix C with parameters.

Table 4.3 Hg intrusion data for LSCF6428; refer to Fig. 4.10(b) [using graphite powder (Fig. 4.9(b)) as a pore former for comparison].

Total Intrusion Volume	0.0822 mL/g
Total Pore Area	0.084 m ² /g
Median Pore Diameter (Volume)	4.3494 μm
Median Pore Diameter (Area)	2.6394 μm
Average Pore Diameter	3.9241 μm
Bulk Density at 0.22 psia	3.8044 g/mL
Apparent (Skeletal) Density	5.5350 g/mL
Stem Volume Used	9%

4.5 Conclusion

A simple model was developed to estimate the maximum pore diameter for carbonate infiltration. To obtain the ideal membrane, a small pore size with a large pore volume is necessary. Cornstarch was finally selected as the pore former material for porous structured membrane fabrication, as the results showed a better structure compared with that of carbon black and graphite. The pore volume estimation by water drop showed that the volume of a membrane is determined by the weight percentage of the pore former added to the membrane material before sintering; however, the results also depend on other factors, such as the ramp speed and combustion temperature, the moisture of the powder, and detailed control of the ventilation in the furnace.

There are many reasons that cause a membrane to crack before and after sintering; from experience, 25% cornstarch makes the best LSCF6428 membranes with a homogeneous micro-porous structure, which is what was needed to perform the experiments.

Chapter 5 High temperature sealing development

5.1 Introduction

An yttria-stabilised zirconia-carbonate dual-phase membrane as a simple model system was studied to test the sealing of the dual-phase membrane system in experiment 1 in Section 5.2. A glass-ceramic to be used as sealing material was prepared that melts at about 700-800°C; the molten phase glass-ceramic mixture could fill the gaps between the membrane and the alumina tube support to seal the membrane system. However, the results showed that the molten phase glass was very mobile and could easily cover the membrane surface and block it, causing the membrane to fail.

Early work on CO₂ permeation using an LSCF2882-potassium carbonate membrane was performed using a ceramic sealant (hard sealant); a large leak was found, and this sealant was given up when silver paste (a soft sealant) was applied to the LSCF membrane (Section 5.3).

Silver paste was used as sealing material. It is designed to reduce the mobility of glass-ceramic at high temperatures and improve the stability of the membrane system. The membrane selectively, long term test and the function of temperatures were tested separately, and the results are shown in Section 5.4.

Finally, the glass-based sealing method was also given up because there are many impurities in glass materials that influence the permeation results of the membrane, especially the silicon oxide from glass-based sealant, which can react with carbonates and produce carbon dioxide. To improve the chemical stability of the membrane, only silver paste was tested and showed very good stability and 50 hours of CO₂ permeation; however, the leak rate was quite significant, about ten times the CO₂ permeation rate.

From many experimental tests, it was shown that silver paste can work much better if a certain pressure is applied on the membrane surface to compress the silver paste after its drying. Two newly designed reactors were tested based on this idea, one using a hook and spring system to press the membrane pellet and the other using heavy tubes to press the membrane; both of them provided 300 g of weight on the membrane. The heavy

tube reactor was finally chosen owing to the successful application on the LSCF membrane. Details are shown in Section 5.5.

To simplify the dual-phase system and easily understand the mechanism, the oxygen ion-conducting membrane YSZ was used for the experiment. The dual-phase system consists of a porous oxygen anion O^{2-} -conducting ceramic substrate hosting a guest molten carbonate phase (usually a Li/Na/K carbonate eutectic mixture) infiltrated within the pore network. Carbon dioxide from the feed gas reacts with oxygen ions supplied by the ionic conducting host membrane to form a carbonate (CO_3^{2-}) anion in the molten carbonate phase. The CO_3^{2-} anion is transported through the molten phase carbonate at high temperatures under a chemical potential gradient and released as gaseous CO_2 on the permeate side. The O^{2-} anion is transported back to the feed-side membrane by the substrate.

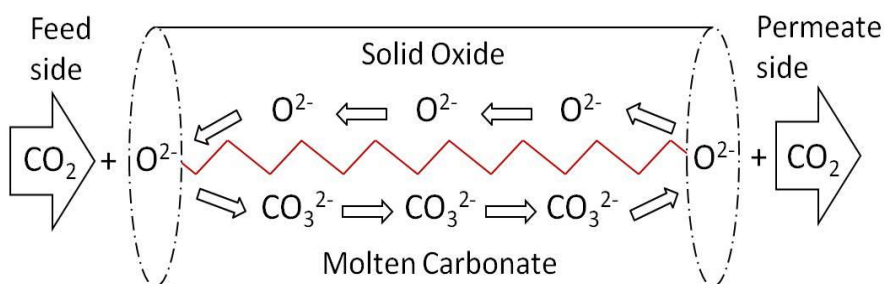


Figure 5.1 Conceptual schematic of the ion-conducting dual-phase membrane.

5.2 Experiment 1: Glass-based sealant

5.2.1 Membrane preparation

The porous membrane fabrication method was introduced in the previous chapter. The molten carbonate was infiltrated into a porous YSZ substrate by a direct infiltration method based on capillary force because of the pore network. The porosity of the host membrane was measured by mercury porosimetry, which indicated that 33 wt% of cornstarch pore former creates about 47% porosity with an average pore size of around 700 nm.

For a 1.5 g porous YSZ host membrane with about 47% porosity, 0.28 grams of carbonate (2.2 g cm^{-3}) was infiltrated, as one would expect if all of the pore volume was occupied by carbonate.

5.2.2 Membrane sealing

The membrane was sealed using a novel combination of glass-based sealant [25] and silver paste, with each component performing a different role. The silver pre-sealed the membrane on the alumina support; the glass-based sealant was then applied around the edge of the membrane after drying the silver paste. The silver can decrease the mobility of the glass and also fits the thermal expansion of the ceramic membrane because it softens at high temperatures of up to 900°C, while the glass-based sealant melts at about 800°C and fills the small gaps between the silver and the membrane and improves the sealing of the whole membrane system. A membrane scheme is shown in Fig. 5.2.

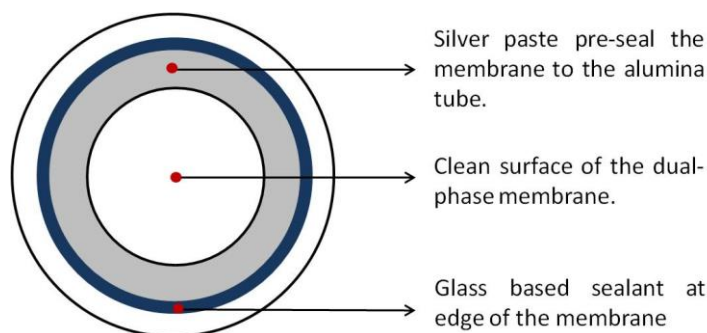


Figure 5.2 Sealing of a dual-phase membrane with a combination of silver and glass-based materials.

5.2.3 Experimental setup

A gas mix of CO₂/N₂ (1:1 mol ratio) was provided as the feed gas to the reactor at 10 ml min⁻¹ (STP), while 20 ml min⁻¹ (STP) of helium was provided as a sweep gas in the permeate side. The membrane reactor was heated by a tube furnace. Permeated CO₂ and N₂ leak were measured on-line by mass spectrometry.

5.2.4 Results and discussion

Fig. 5.3 shows that the CO₂ flux (active area of 0.5 cm²) plateaued for three hours at 850°C but then steadily decreased. The CO₂ flux then declined sharply when the temperature decreased from 850 to 780°C at 5°C min⁻¹. This change in temperature was made to determine the effect of a temperature change on performance and to reduce the mobility of the sealant. The average leakage-subtracted CO₂ permeability at 850°C was 7×10⁻¹¹ mol m⁻¹ s⁻¹ Pa⁻¹, while at 780°C, it decreased to 2×10⁻¹¹ mol m⁻¹ s⁻¹ Pa⁻¹. The

average selectivity of CO₂ over N₂ at 850°C was 15:1 and was initially 17:1 at 780°C. It decreased to 2:1 after a further one hour as the N₂ leak increased.

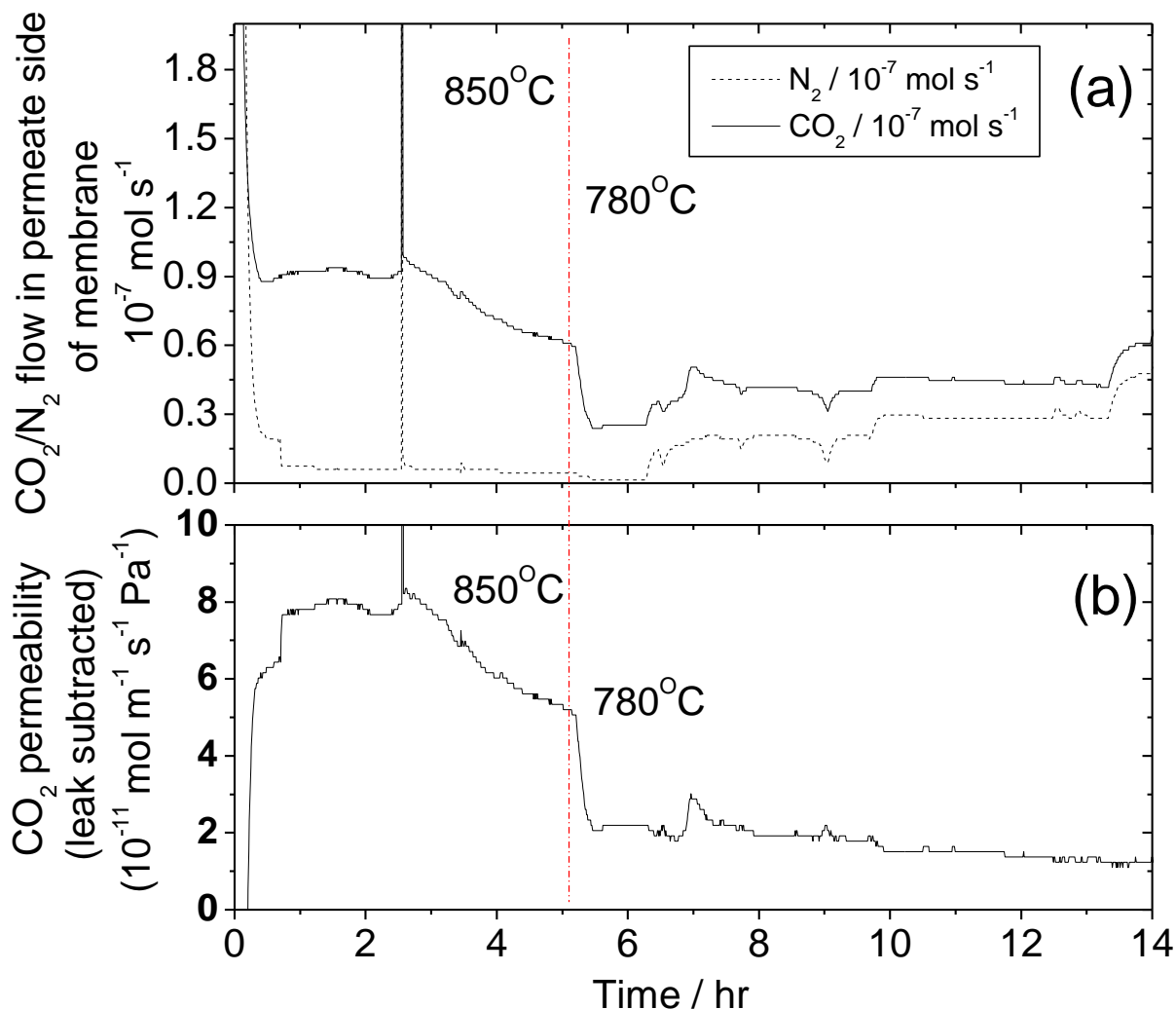


Figure 5.3 (a) Flux of CO₂ and leaking N₂ in the permeate side of the membrane at 850 ° and 780°C. 50% CO₂ and 50% N₂ at 1 atmosphere are provided in the feed side of the membrane at a total inlet flow rate of 10 ml (STP) min⁻¹; (b) the resultant leakage-subtracted CO₂ permeability.

CO₂ permeation was also studied at 800°C, as shown in Fig. 5.4. The CO₂ permeability was stable for the first 30 hours and then decreased slowly when the N₂ leak increased and, finally, the sealing of the membrane failed. The CO₂ permeated over 50 hours was estimated to be 0.009 mol, while the carbonate that infiltrated into the membrane, 0.28 grams, contained 0.0028 mol of carbonate ions.

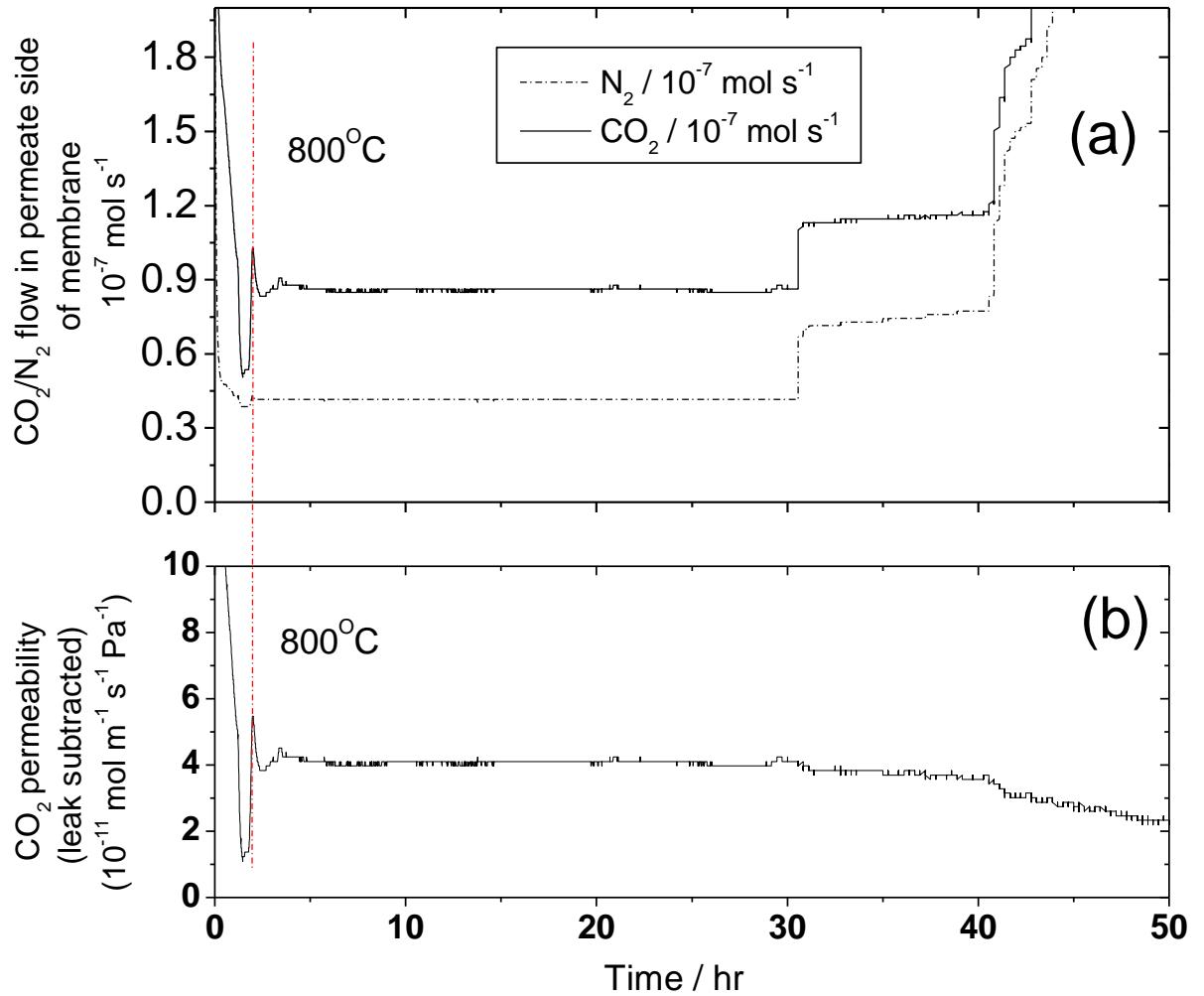


Figure 5.4 CO_2 permeation over 50 hours. (a) Flux of CO_2 and leaking N_2 in the permeate side of membrane at 800°C ; (b) the resultant leak-subtracted CO_2 permeability.

The CO_2 flux at different temperatures was measured. Fig. 5.5 shows the CO_2 permeability dependence on temperature. It indicates that permeability decreased with a decrease in temperature. This decrease was reversible on returning the membrane temperature to a higher value.

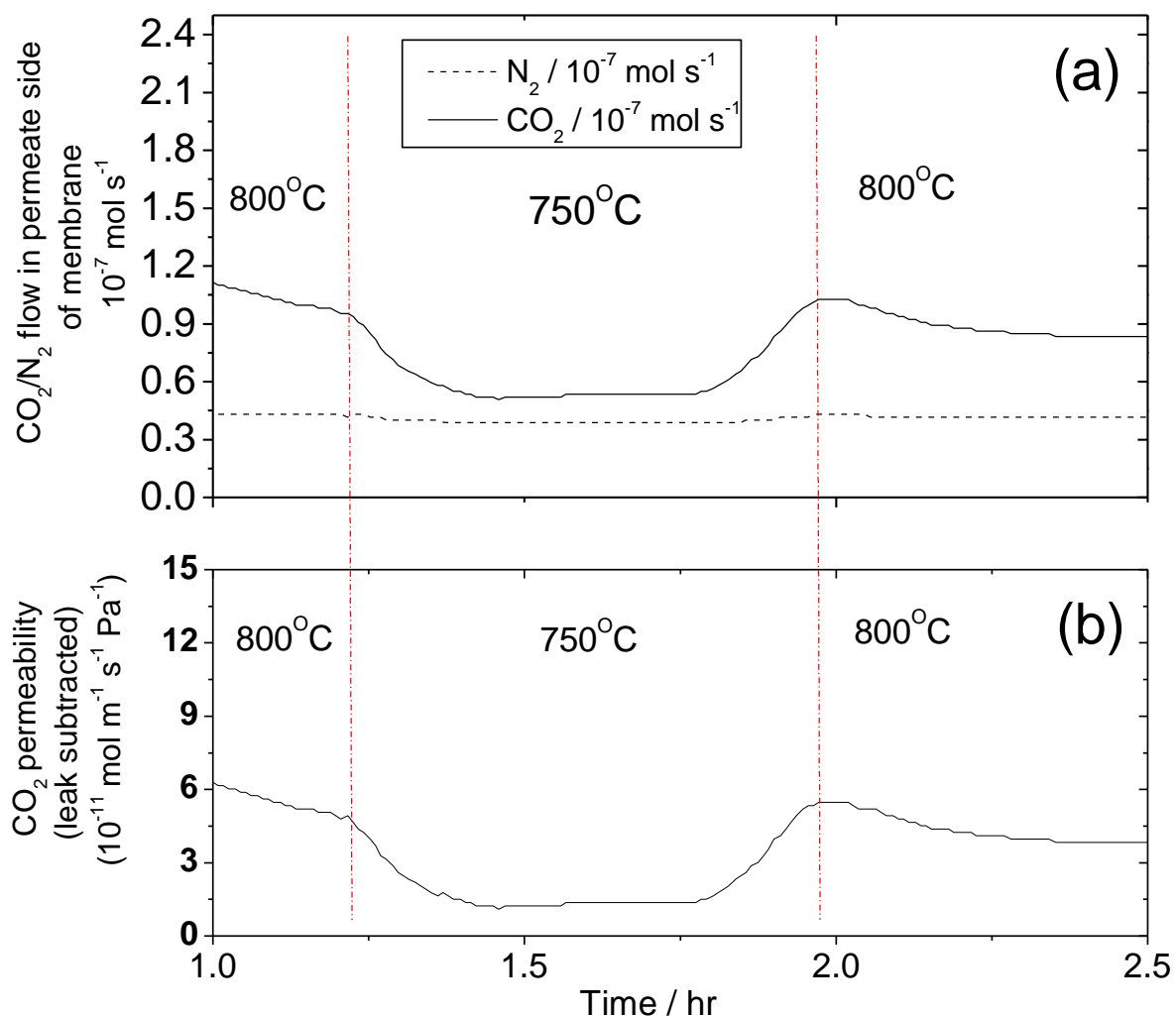


Figure 5.5 (a) Flux of CO_2 and leaking N_2 ; (b) the resultant leak-subtracted CO_2 permeability.

5.2.5 Summary

The CO_2 permeability of a dual-phase YSZ-carbonate membrane was investigated at 800°C. 0.009 mol of CO_2 were permeated over 50 hours, while 0.0028 mol of carbonate ions were infiltrated, which indicated that CO_2 permeation had occurred. The CO_2 permeability at 850 °C was $7 \times 10^{-11} \text{ mol m}^{-1} \text{ s}^{-1} \text{ Pa}^{-1}$, while at 800°C, it decreased to $4 \text{ mol m}^{-1} \text{ s}^{-1} \text{ Pa}^{-1}$ and $2 \text{ mol m}^{-1} \text{ s}^{-1} \text{ Pa}^{-1}$ at 780°C. The sealing method gave a ratio of permeated CO_2 to N_2 leakage of 15:1 at 850°C.

However, this sealing method had many problems when applied to LSCF membranes because the molten phase glass goes through the pores, covers the membrane surface immediately after heating to 800°C, and blocks the membrane in 5 hours. Another disadvantage is that the glass-based materials contain silicon oxide, which can slowly

react with molten carbonate at high temperatures; this could give an incorrect CO₂ permeation result.

The next experiment was an early test for CO₂ permeation using an LSCF-carbonate membrane but sealed with ceramic sealant (alumina oxide); because a large leak was found, this method was not applied in other experiments.

5.3 Experiment 2: Ceramic sealant

An LSCF2882 membrane infiltrated with potassium carbonate was used in this experiment; the feed side contained 50% CO₂ in N₂. Helium was used as the carrier gas. The graph in Fig. 5.6 shows the mole fraction of each component of outlet gas from the CO₂ permeation test; there was a small amount of N₂ (1.17 mol%) and CO₂ (0.17 mol%) leakage from the inner tube to the permeate side of the membrane at the beginning of the test. The mole percentage of CO₂ and N₂ increased as the temperature increased. The N₂ mole fraction was higher than that of CO₂ from the beginning until the temperature reached about 880°C, mainly caused by the feed gas and air flowing through various connections. The membrane was quite fragile; also, the sealant and alumina tube had different thermal expansion rates from that of the dual-phase membrane, which may have contributed to the sealing failure.

The CO₂ mol fraction increased significantly from 880°C on and exceeded that of N₂ after 900°C (Fig. 5.6). The maximum CO₂ permeation rate was calculated to be 0.58 μmol cm⁻² s⁻¹ at 930°C and 1 atm or permeance of 1.15×10^{-7} mol m⁻² s⁻¹ Pa⁻¹. This CO₂ permeation rate, shown in Fig. 5.6(b), was obtained by subtracting the leaking CO₂ flow rate from the total CO₂ emissions to the downstream; this was determined by monitoring the N₂. The temperature at which CO₂ mol% started to increase and exceed that of N₂ was close to the melting point of potassium carbonate (891°C). The ionic CO₃²⁻ that released CO₂ to the permeate side of the membrane may have come from both potassium carbonate from the dual-phase membrane (molten salt) and feed gas CO₂ in the upstream side of the membrane. After the reactor was maintained at 940°C for more than 12 hours, the N₂ mole fraction rose to just 1 mol% less than that of CO₂, and the CO₂ content was slightly decreased. This indicated a bad leak in the sealing or a membrane break and less CO₂ release to the downstream side of the membrane.

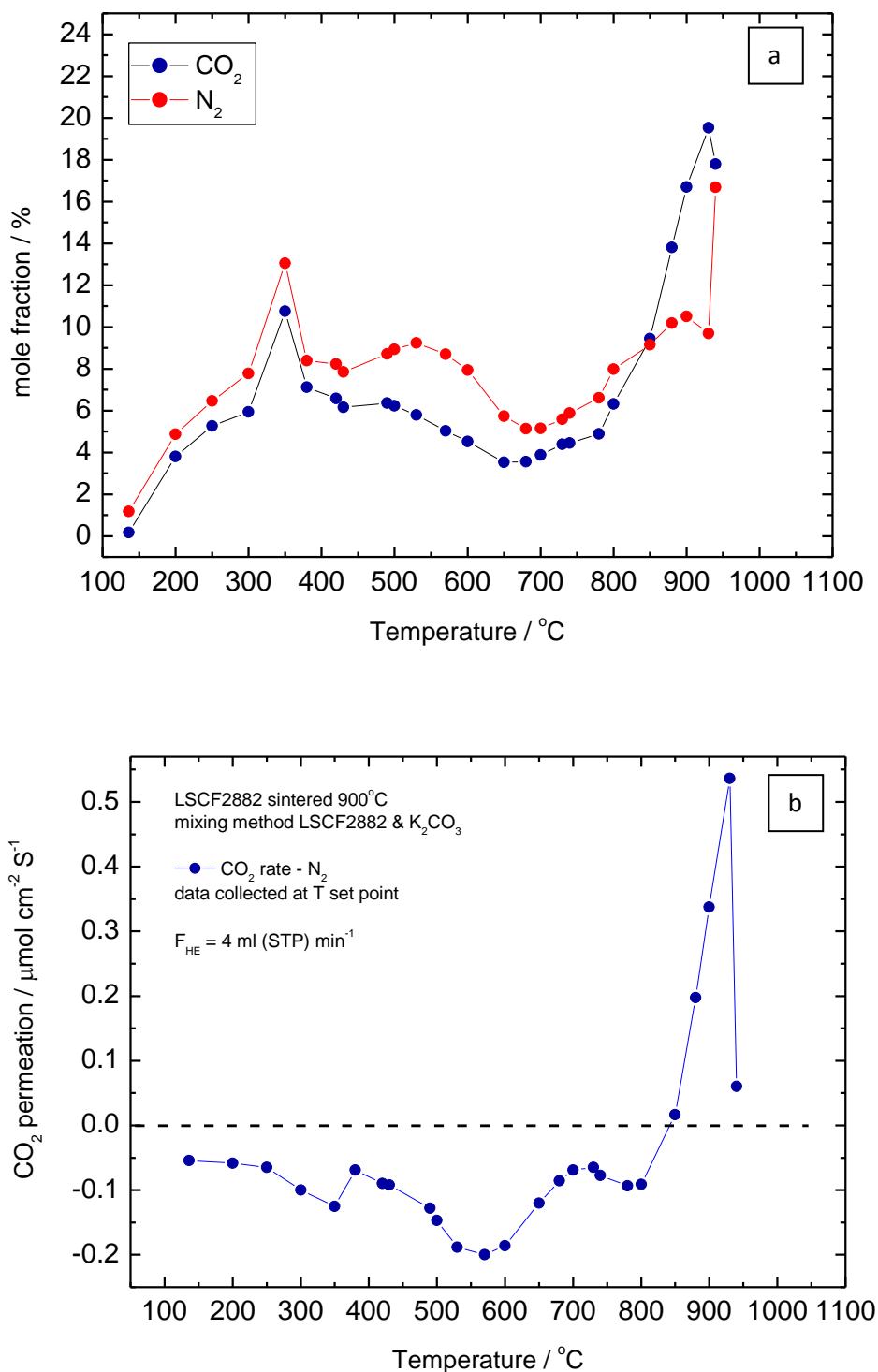


Figure 5.6 (a) CO₂ and N₂ mole fraction from the downstream side of the membrane according to the temperature; (b) CO₂ permeation apart from N₂ leak CO₂ flow.

The experiment was repeated using an LSCF2882-potassium carbonate dual-phase membrane (Fig. 5.7). The mol% of CO₂ was higher than that of N₂ from 890°C to 940°C and persisted for more than 1 hour. The potassium carbonate melted at a temperature around 890°C and became viscous, which would have filled some leaking

Chapter 5. High temperature sealing development

areas and pores; this may have decreased the N_2 flow rate. The path for CO_3^{2-} transportation through the molten potassium carbonate was theoretically activated at a temperature above $890^\circ C$. This might be the reason that the CO_2 content did not decrease as the N_2 fraction declined. However, carbonate decomposition and desorption may also happen in this process. Dense LSCF2882 membranes sintered at $1,250^\circ C$ for 12 hours were also prepared for a blank experiment and to test the quality of the ceramic sealant.

As there was gas resistance in the GC gas sampling valve to provide back pressure, this may have caused the softened sealing to move away from the membrane at high temperatures so that the reactor developed a cross-chamber leak between the inside and outside of the membrane support tube in the reactor. A needle valve was temporarily applied to balance the back pressure from the GC and control the rate of the gas flow from the inner tube and the outer tube to be approximately equal to the feed gas flow rate (10 ml min^{-1}) when a leak occurred on the membrane. This problem will be solved in later work to improve the gas-tightness of the membrane and sealing to eliminate the gas phase transport of the feed gas through to the permeate side of the permeation cell and prevent back pressure from the GC.

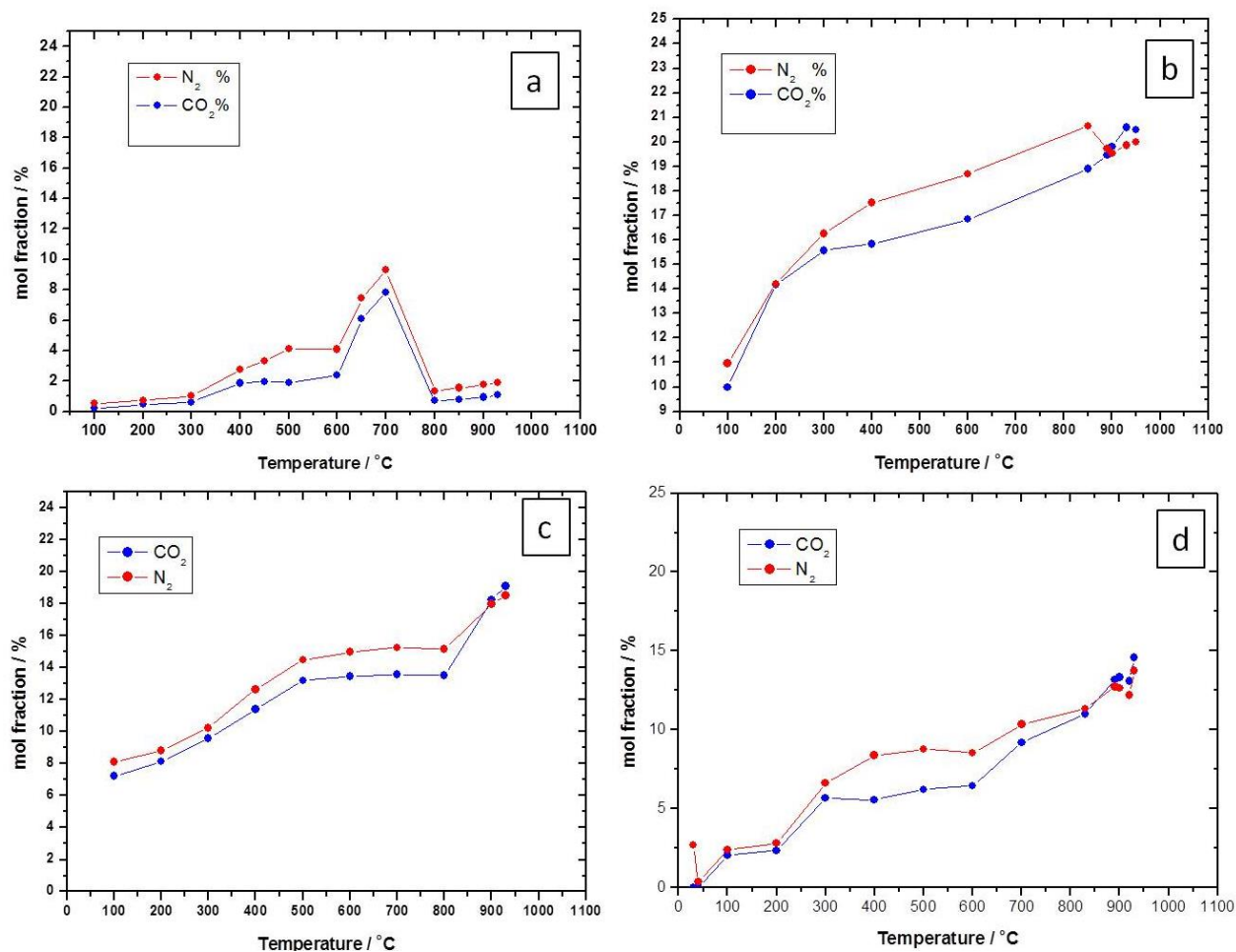


Figure 5.7 CO₂ and N₂ mol fractions from the downstream side of the membrane according to the temperature. (a) Blank test with a dense LSCF2882 membrane; (b), (c), and (d) are CO₂ permeation results; also indicated is the N₂ leakage.

5.3.1 Summary

The initial CO₂ permeation flow rate was obtained at a temperature near the melting point of potassium carbonate (900°C), but significant leakage was also involved with CO₂ permeation. The CO₂ mole fraction became greater than that of N₂ at around 900°C with a maximum CO₂ permeate flux of 0.58 $\mu\text{mol cm}^{-2} \text{s}^{-1}$ ($1.15 \times 10^{-7} \text{ mol} \cdot \text{m}^{-2} \text{s}^{-1} \text{ Pa}^{-1}$) at 930°C, decreasing to 0.07 $\mu\text{mol cm}^{-2} \text{s}^{-1}$ / $1.38 \times 10^{-8} \text{ mol m}^{-2} \text{s}^{-1} \text{ Pa}^{-1}$ (1 mol% more than N₂) after 12 hours' operation.

5.4 Experiment 3: Silver paste sealant

5.4.1 Membrane fabrication

Commercial La_{0.6}Sr_{0.4}Co_{0.2}Fe_{0.8}O_{3- δ} (LSCF6428) powder was mixed with cornstarch (Sigma-Aldrich) with a weight ratio of 1.5:0.5. The pellets were formed by uniaxial

pressing at 3 tonnes using an automatic ATLAS T25 uniaxial press. Subsequently, the pellets were sintered in air to combust the cornstarch and then the temperature was ramped up to 1,250°C at 1°C/min and held for 12 hours, followed by slow cooling to room temperature at 1°C/min. The diameter and the thickness of the sintered pellets were approximately 15.5 mm and 2 mm, respectively. Direct molten carbonate infiltration was applied on the membrane surface; the carbonate mixture (Li:Na:K = 51:16:33) was ground and placed on the top surface of the membrane and heated to 500°C in an atmosphere of air.

5.4.2 Membrane sealing

The hook-spring reactor shown in Fig. 5.8 consists of a Pt wire connected to a hook to press the membrane, and the silver paste was compressed during the heating process; the force applied on the membrane was about 300 g. The experimental results showed that the hook-spring system cannot work at high temperatures, especially when the reactor system heats up to 600°C; either the spring or the Pt wire will break because of the softness of the materials. The disadvantage of this design is that the whole reactor system was heated during the experiment; the mechanical strength of the metal materials became weak, which caused the system to fail, and when the spring fails at high temperatures, this becomes very dangerous.

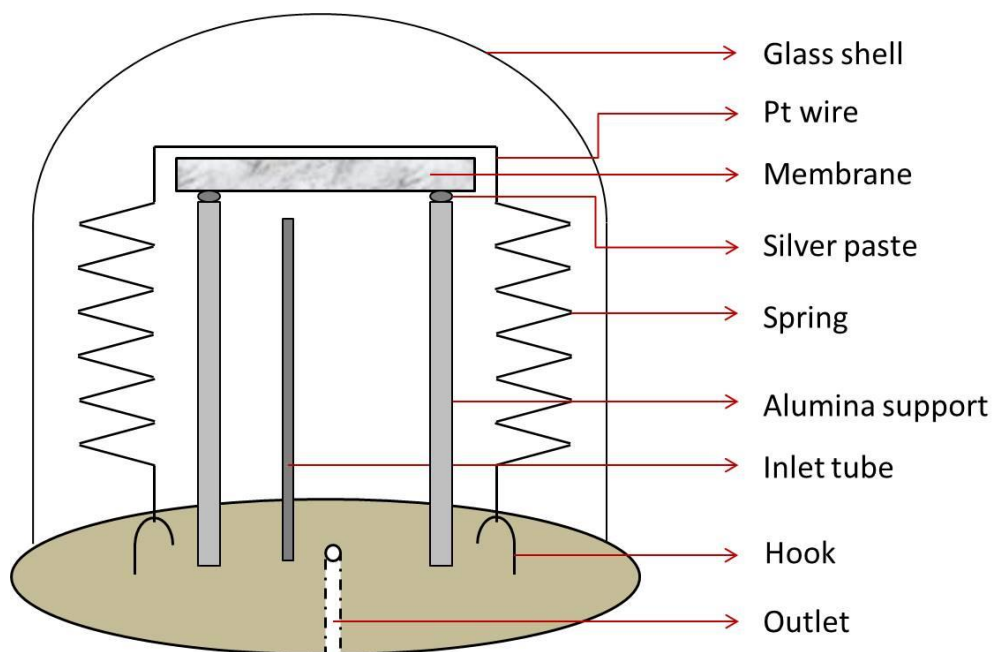


Figure 5.8 Schematic diagram of a membrane sealing system that includes spring and hook to apply pressure on the silver paste below the membrane; the silver paste was dried in air before pressure was applied.

Another design was different but simpler than the hook-spring reactor, based on the same principle that the silver sealant needed to be pressed to improve the membrane sealing. Fig. 5.9 shows a 300 g alumina tube with a semi-closed end on the membrane to put pressure on the silver paste, which was previously dried. The membrane was sealed after heating to about 500°C.

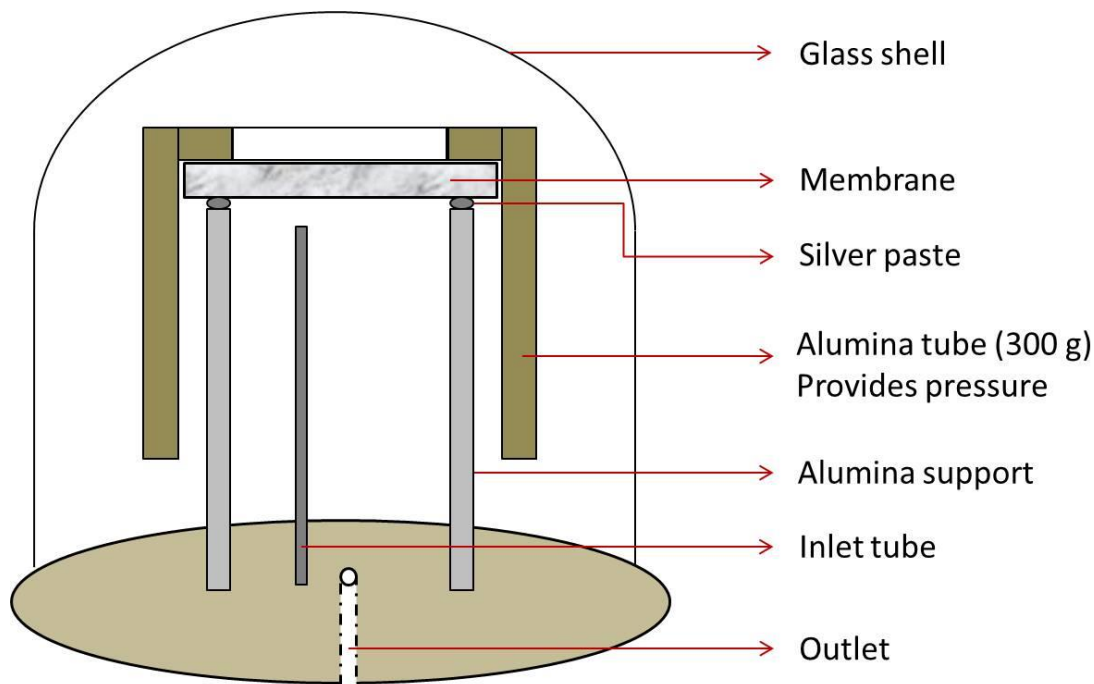


Figure 5.9 The scheme of a membrane sealing system that includes a heavy tube with a semi-closed end to press the membrane.

5.4.3 Experimental equipment

A gas cylinder with a mixture of CO₂ and N₂ in a 1:1 ratio was provided for the feed side of the membrane and pure helium was used for the permeate side of the membrane. The gas flow rate for the feed and permeate sides of the membrane were both 20 ml min⁻¹ (STP). The membrane reactor was heated by a tube furnace. Permeated CO₂ and N₂ leak were measured on-line by mass spectrometry.

5.5 Results and discussion

When the LSCF membrane was operated without a press device and sealed by silver paste normally, the reactor was heated from room temperature to 400°C to deep dry the silver paste. The mass spectrometer read the mole fraction of both nitrogen and carbon dioxide in the permeate side of the membrane. In period A, the membrane developed a

Chapter 5. High temperature sealing development

bad leak; the high nitrogen value came from the atmosphere because of the leak in the membrane, as the gas flow rate from the permeate side of the membrane could not supply the mass spectrometer, which requires a 15 ml min^{-1} gas flow, as a pump was connected to the outlet of the mass spectrometer.

Then the membrane was heated to 400°C at $955^\circ\text{C min}^{-1}$, and the membrane was sealed during the heating but still had a high leak rate; the permeate gas flow was enough to feed the mass spectrometer and the air stopped coming to the mass spectrometer. As the feed side provides carbon dioxide and nitrogen at a 1:1 ratio, the leak rate of carbon dioxide was considered to have the same value as the nitrogen in the permeate side of the membrane. Fig. 5.10(b) shows the carbon dioxide permeation process with a nitrogen leak; the portion of carbon dioxide that was higher than the nitrogen was the permeate carbon dioxide, and the nitrogen was considered to leak. Although a large leak occurred, the carbon dioxide permeation was quite stable, and it was maintained for about 50 hours.

After this, the temperature was decreased from 950°C to 900°C and the carbon dioxide permeation rate was correspondingly decreased. When the temperature dropped to room temperature, there was no carbon dioxide permeation; the carbon dioxide and nitrogen in the permeate side showed a 1:1 ratio.

The carbon dioxide permeation rate, apart from the leak, can be estimated by the subtraction of nitrogen; the pure carbon dioxide permeation results are shown in Fig. 5.11.

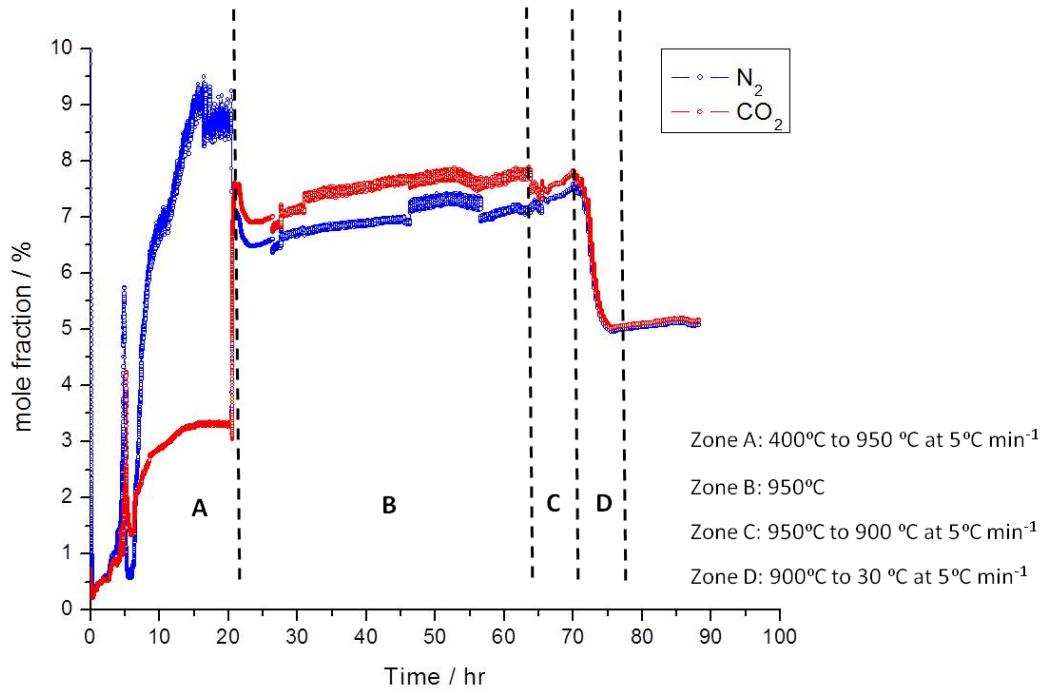


Figure 5.10 Sealing effect of silver paste without a press device.

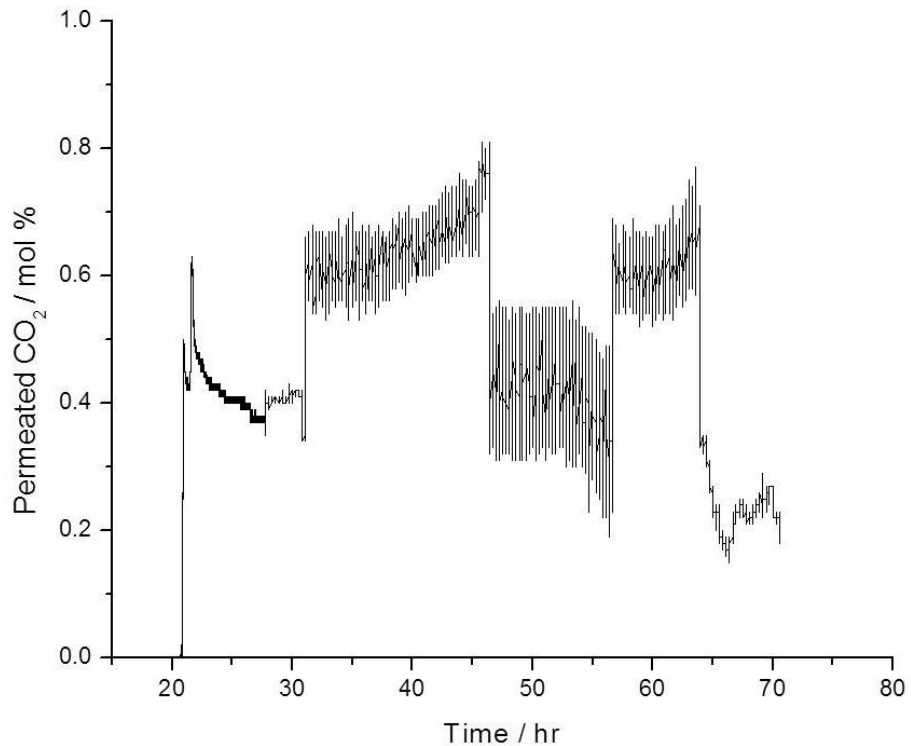


Figure 5.11 Time dependence of permeate carbon dioxide after subtracting leaks.

Long-term carbon dioxide permeation of about 50 hours could be achieved by using a silver sealant, and the membrane was quite stable, without any cracking; however, the leak rate was quite significant. Using a press device, as shown in Fig. 5.9, the same

Chapter 5. High temperature sealing development

experiment was carried out, and the membrane sealing improved dramatically; the silver paste was first dried in air for 8 hours, and the membrane installed into a membrane reactor. The membrane was heated directly from room temperature to 800°C by a ramp rate of 1°C min⁻¹; the membrane showed a large leak at the beginning, but when the temperature reached about 500°C, the membrane was sealed perfectly (Fig. 5.12). As the temperature increased, the carbon dioxide started to permeate across the membrane; when the temperature reached 700°C, the nitrogen leaked, which indicated a very small carbon dioxide show leak with a value between 0.02 and 0.05%, and the permeate carbon dioxide in the permeate side was about 0.8%. At 18 hours, the temperature was increased from 800°C to 900°C; the carbon dioxide permeation was correspondingly increased, but the nitrogen leak also rose slightly.

The experiment was not stopped after this; rather, it operated for more than 100 hours, and the nitrogen leak increased continuously. This indicated that the molten carbonate was moving and that leaks were generated slowly. In many further experimental tests, the reason that the leak developed, even though the sealing was excellent in the beginning, was studied. There are two main reasons; one is that the carrier gas in the permeate side was helium, which has a small molecule size and is very sensitive to tiny leaks, so it could easily develop a leak during such a long-term experiment. The results were much better when using argon as the carrier gas. The second reason is that the molten carbonate in the pore network in the permeate side has contact with pure helium or argon, so it needs a certain carbon dioxide partial pressure to prevent the calcination of carbonate salts and decrease the loss of carbon ions at high temperatures. However, the smaller the pore size is, the greater the ability is to lose carbonate ions from molten carbonate at high temperatures because of the large surface area of the carbonate that is in contact with the carrier gas flow.

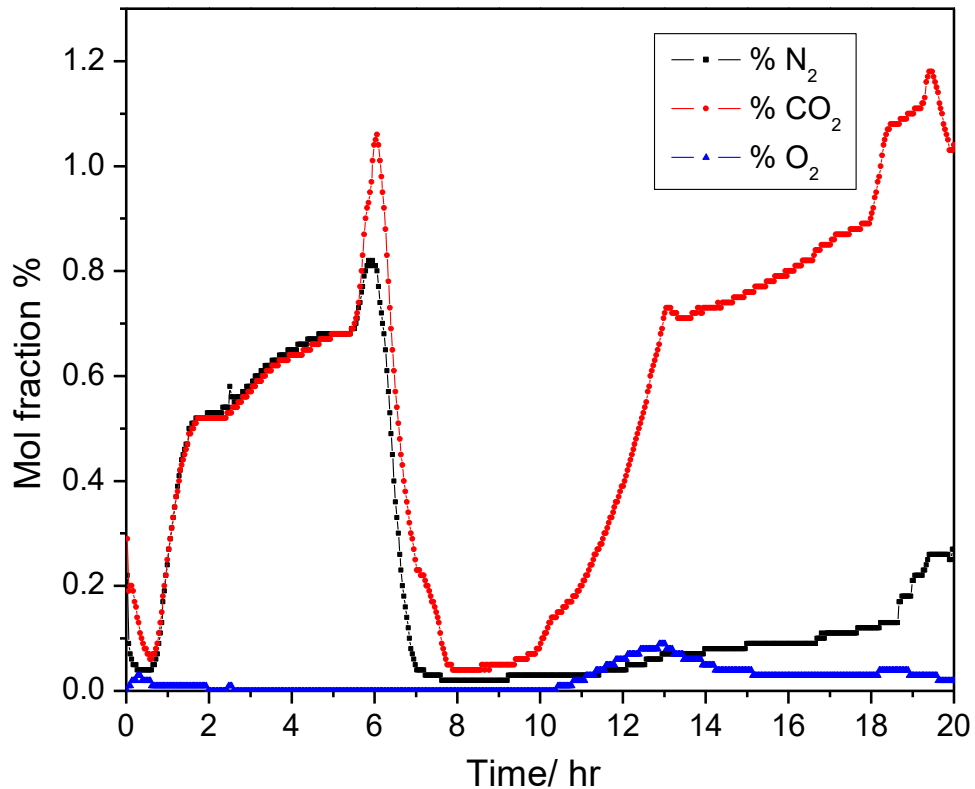


Figure 5.12 Sealing effect using silver paste with a press device.

5.6 Conclusion

The sealing method is important for a membrane, especially for a dual-phase membrane, and sealing is difficult to achieve. This chapter described how the sealing method in our experiment was developed. A ceramic sealant was firstly used for the initial experiment described in Chapter 3, and the problem detected was membrane cracking caused by the thermal expansion of both the membrane material and the ceramic sealant. After this, a glass-based sealant was selected from Anderson and Lin's paper; however, there was membrane blocking during the heating process, so the membrane could not work after the glass covered the membrane surface and there was no data collection after blocking.

To solve this problem, silver paste was used to reduce the mobility of the molten glass at high temperatures. It worked for the YSZ membrane, although it has been reported that there is a reaction between silicon and molten carbonate. However, it did not work for the LSCF membranes because an LSCF membrane functions at higher temperatures and the molten phase glass can spread into the pore structure and cause membrane

Chapter 5. High temperature sealing development

failure. In addition, the side reaction always gives incorrect data. The glass-based sealant was not used in further experiments.

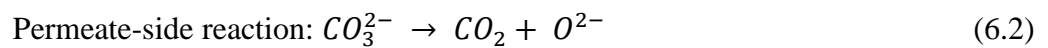
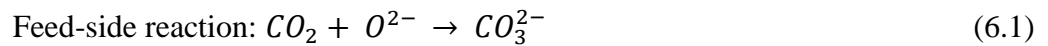
Silver paste was tested as a sealing material for an LSCF membrane, and the results showed a significant leak; however, the membrane operation was very stable during a 50-hour experiment. The silver sealant was chemically stable, and there were no side reactions between the silver and the carbonate or membrane materials.

Two reactor designs were introduced, one using a hook-spring system to press the membrane sealant to improve the sealing and the other using a heavy tube to press the membrane. For convenience and because of safety issues, the second one was finally chosen, and it showed excellent sealing; the ratio of carbonate and leaked nitrogen was 40:1, and the best result was 97.5% carbon dioxide in the permeate side of the membrane. However, leaks developed during the long-term experiment, and the leak rate, though it increased very slowly, finally disturbed the experiment. The problem was investigated and found to be the helium carrier gas and low carbon dioxide partial pressure. Using argon instead of helium and a supply of about 1% carbon dioxide in the permeate side of the membrane could solve the problem. A long-term experiment with excellent sealing was achieved when conducting up-hill permeation. This is described in Chapter 7.

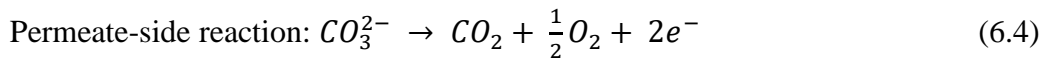
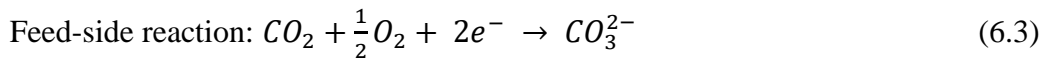
Chapter 6 Kinetics and the limiting step for CO₂ permeation

6.1 Introduction

La_{0.6}Sr_{0.4}Co_{0.2}Fe_{0.8}O_{3-δ} (LSCF6428) is known as a mixed ionic-electronic conducting (MIEC) perovskite oxide material that has wide applications, especially for oxygen separation membrane fabrication. Ceramic-carbonate dual-phase membranes made from LSCF6428 were tested for carbon dioxide separation from nitrogen at high temperatures. The mechanism that was investigated is explained; the ionic oxygen combines with carbon dioxide molecules to form carbonate ions in the molten carbonate in the feed side of the dual-phase membrane and releases gaseous carbon dioxide in the permeate side of the membrane and oxygen ions back to the feed side through the perovskite substrate. However, as a mixed ionic-electronic conducting membrane, the LSCF-carbonate membrane allows oxygen to permeate through the substrate together with carbon dioxide permeation when oxygen is provided in the feed side. Therefore, both carbon dioxide and oxygen can permeate across the membrane if they are fed together to the reactor at a high temperatures (>700°C). The different mechanisms of carbon dioxide permeation are shown in Fig. 6.1. The pure ion-conducting dual-phase membrane is shown in Fig. 6.1(a); the oxygen cycles in the solid oxide substrate, while the carbon dioxide permeates across the membrane by the reaction shown below:



This happens when the LSCF-carbonate dual-phase membrane operates at high temperatures (>700°C) and carbon dioxide is provided to the feed-side of the membrane without gaseous oxygen. However, at temperatures below 700°C, the membrane substrate has no obvious oxygen ion conductivity and is only in an electron-conducting solid phase. Therefore, gaseous oxygen needs to be provided together with carbon dioxide in the feed side of the membrane to permeate carbon dioxide at a temperature between 500°C (at which molten phase carbonate is obtained) and 700°C by the reaction:



The pure electron-conducting membrane is shown schematically in Fig. 6.1(b). There is a hypothesis that, at high temperatures of more than 700°C, both carbon dioxide and oxygen are provided in the feed side of the membrane; the solid phase is a porous mixed ionic-electronic conducting membrane infiltrated with molten carbonate, and the carbon dioxide may permeate across the membrane by both mechanisms shown in Fig. 6.1. In addition, the oxygen can permeate across the membrane substrate directly as a pure oxygen-conducting membrane.

The objective of this chapter is to investigate the relationship between carbon dioxide permeance and oxygen partial pressure in the feed side at 880°C and the impact of carbon dioxide partial pressure on both oxygen and carbon dioxide permeance. The first two experiments aimed to test the carbon dioxide permeance as a function of the partial pressure of the feed oxygen and carbon dioxide, respectively; the third experiment was conducted to test whether the feed oxygen or the feed carbon dioxide was the limiting step that dominated carbon dioxide permeation and to measure how large of a driving force oxygen provides to ‘push’ the carbon dioxide across the membrane, as Fig. 6.1(b) shows that both oxygen and carbon dioxide partial pressure differences could improve the carbon dioxide permeation.

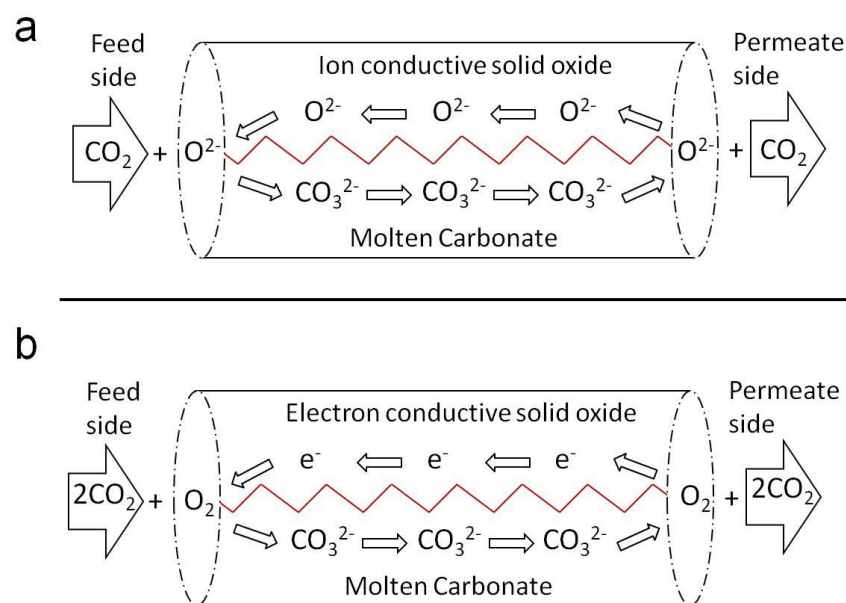


Figure 6.1 Schematic mechanism of ion-conducting (a) and electron-conducting (b) dual-phase membranes for CO₂ separation.

6.2 Experiment

6.2.1 Host membrane fabrication

Commercial La_{0.6}Sr_{0.4}Co_{0.2}Fe_{0.8}O_{3-δ} (LSCF6428) powder was purchased from Praxair. The powder was synthesised by combustion spray pyrolysis, resulting in powders with a particle size of less than 1.1 μm. The pellets were formed by uniaxial pressing of approximately 1.5 g of the LSCF powder mixed with 0.5 g of cornstarch (Sigma-Aldrich) at 3 tonnes using an automatic ATLAS T25 uniaxial press. Subsequently, the pellets were sintered in air by ramping their temperature from room temperature to 200°C at 1°C/min and holding at 200°C for 2 hours (so that cornstarch burnout and pore formation occurs) and then ramping the temperature to 1,250°C at 1°C/min and holding this temperature for 12 hours, followed by slow cooling to room temperature at 1°C/min. The diameter and the thickness of the sintered pellets were approximately 15.5 mm and 1 mm, respectively, after being polished using SiC paper. The average pore size (radius) and pore size distribution of the LSCF substrate sintered at 1,250 °C were measured by mercury porosimetry at Imperial College (porosity: 40% approx., average pore size: 600-700 nm).

6.2.2 Carbonate infiltration for sintered LSCF host membranes

Sintered LSCF supports were infiltrated with molten carbonate (Alfa Aesar, 99% min) to obtain a dual-phase membrane. Direct infiltration of the supports was performed using 0.2 g of a mixture of lithium carbonate (Li₂CO₃), sodium carbonate (Na₂CO₃), and potassium carbonate (K₂CO₃) in a molar ratio of 42.5/32.5/25 and heated from room temperature to 500°C at 5°C/min, followed by holding at 500°C for 30 min to allow the molten carbonate to soak into the membrane via capillary action. The membrane was cooled to room temperature at 5°C/min. The infiltration process was repeated until residual carbonates were seen to be present on the top surface of the membrane (taking the usual two steps). This residual carbonate was removed with SiC paper by light polishing.

6.2.3 Sealing of prepared membranes

The dual-phase membrane was placed on top of an alumina tube support and sealed with a commercial silver ink (FuelCellMaterials, silver ink AG-1, 73.8% wt) to

minimise cross-chamber leaks; the sealant was dried in air for 6 hours at room temperature before use.

6.2.4 Experimental setup and reactor system

High-temperature CO₂ and O₂ permeation were carried out in different CO₂/O₂ molecular ratios using a membrane reactor. The reactor system consisted of a feed-side chamber and a permeate-side chamber. The chamber volume for the feed side and permeate side were 11.5 cm³ and 250 cm³, respectively. The dual-phase pellet separate two chambers. The gases provided by BOC were 50% CO₂ balanced by N₂ (cylinder 1, C-1), 20% O₂ balanced in argon (cylinder 2, C-2), and pure helium as a carrier gas (cylinder 3, C-3). The nitrogen in C-1 was set at 50% to estimate cross-chamber leakage, as the CO₂/N₂ molecular ratio was 1:1. When the experiment was performed, the CO₂ leakage was estimated to be the same as the nitrogen leakage for the identical partial pressure driving forces and the leakage rate proportional to that driving force.

A set of four mass flow controllers (MFC-1, MFC-2, MFC-3, and MFC-4) (Flotech) was used to control the flow rate of gases. For experiment 1, the aim of which was to investigate the CO₂ permeation by feeding a range of different partial pressures of oxygen together with a constant 20% CO₂, the gases flowed from C-1 controlled by MFC-1 mixed with the gas flow from C-2 controlled by MFC-2 in different ratios and balanced by pure helium from C-3 controlled by MFC-3 (shown in Table 1 below), such that mixed gases were delivered to the feed side of the dual phase membrane in the reactor. Pure helium as a carrier gas, also from C-3, was split to a second pipe connected to and controlled by MFC-4 and delivered to the permeate side of the membrane in the reactor. The outlet gas flow from the permeate side, which was mainly helium, was transported to the mass spectrometer (HIDEN, HALO 100-RC) for analysis. Both gas flows, to the feed side and the permeate side, were set to 20 (STP) ml min⁻¹.

Table 6.1 Mass flow control for experiment 1

O ₂ mol% in 20 ml min ⁻¹ (%)	50%CO ₂ flow rate from MFC-1 (ml min ⁻¹)	20% O ₂ flow rate from MFC-2 (ml min ⁻¹)	Balance helium flow rate from MFC-3 (ml min ⁻¹)	Total flow rate for feed side (ml min ⁻¹)
2	8	2	10	20
4	8	4	8	20
6	8	6	6	20
8	8	8	4	20
10	8	10	2	20

12	8	12	0	20
----	---	----	---	----

Similarly, experiment 2 aimed to investigate CO₂ permeation but provide different partial pressures of CO₂ to the feed side of the membrane, and the oxygen mole fraction was constant at 4%. MFC-1 determined the gas flow rate from C-1, MFC-2 determined the gas flow rate from C-2, and a balanced gas helium flow was split from C-3 determined via MFC-3. A second pipe split from C-3 provided the carrier helium connected to MFC-4. The series of different partial pressures of CO₂ for this experiment are presented in the following table.

Table 6.2 Mass flow control for experiment 2

CO₂ mol% in 20 ml min⁻¹ (%)	CO₂ and N₂ flow rate from MFC-1 (ml min⁻¹)	4% O₂ flow rate from MFC-2 (ml min⁻¹)	Balance helium flow rate from MFC-3 (ml min⁻¹)	Total flow rate for feed side (ml min⁻¹)
40	16	4	0	20
30	12	4	4	20
20	8	4	8	20
10	4	4	12	20
5	2	4	14	20

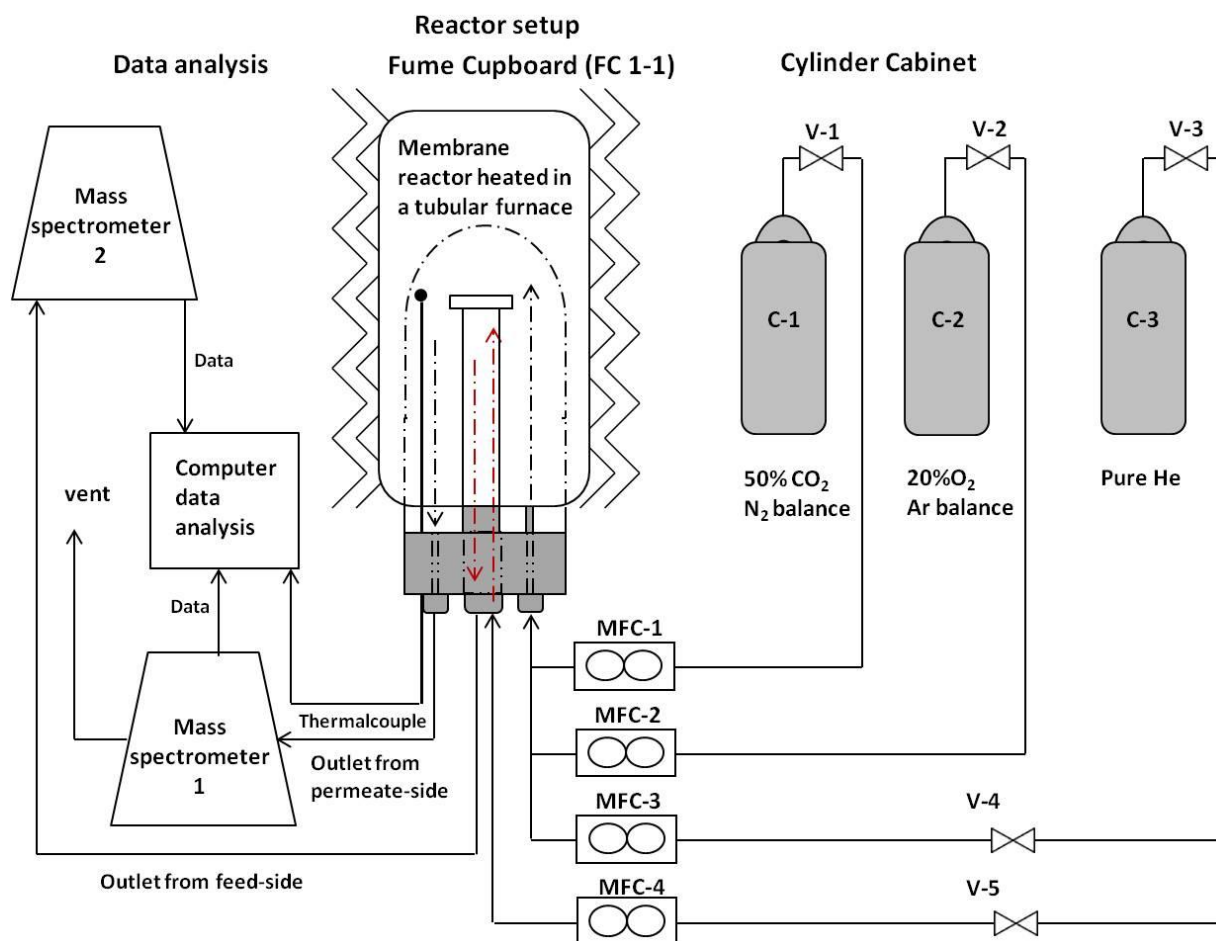


Figure 6.2 Scheme of the membrane reactor setup for the kinetic experiment.

6.3 Results analysis

Experiment 1: CO₂ permeation as a function of O₂ partial pressure in the feed side

Experiment 1 was started at a temperature of 30°C; gases from C-1 (50% CO₂) diluted in helium to 20% carbon dioxide were put into the feed-side chamber of the membrane reactor at 20 (STP) ml min⁻¹ and pure helium from C-3 was fed to the permeate side of the reactor at 20 (STP) ml min⁻¹. The reactor started heating at a ramp of 1°C min⁻¹ from 30°C to 880°C and stayed at 880°C, while the mass spectrometer began recording the data at the same time as the reactor heating started. The raw data for the gas composition were collected from the permeate-side chamber of the reactor and are shown in Fig. 6.3 as mole fractions consisting of nitrogen, carbon dioxide, and oxygen. It can be noted that the carbon dioxide and nitrogen mole fractions started to increase at

the beginning of the heating process and that the CO₂/O₂ ratio was about 1:1. This is due to cross-chamber leakage during the heating process, and the leak declined gradually after 7 hours' further heating of the reactor. At times between 7 and 10 hours, there was carbon dioxide evolution rather than carbon dioxide and nitrogen leakage. The extra carbon dioxide in this period is considered to derive from the release of dissolved carbon dioxide and the decomposition of bicarbonate that formed before and during membrane infiltration. The gas evolution was repeatable when heating the dual-phase membrane and it was also found that there was no significant carbon dioxide permeation at about 600°C at this point unless oxygen was provided because there was no mobile ionic oxygen to form carbonate at this temperature, according to the mechanism (Fig. 6.1(b)).

The carbon dioxide started to permeate across the membrane after 10.5 hours and increased rapidly with increasing temperature. The permeation of carbon dioxide was stable with a mole fraction of 0.63% at about 15 hours after heating when the temperature stayed at 880°C. It was also noted that dissolved oxygen came out of the membrane and formed a tiny peak. Nitrogen leakage stayed at 0.1% during this period. It is interesting that both carbon dioxide and oxygen increased rapidly in the permeate side after introducing 2% oxygen to the feed-side chamber at the 16-hour point. The carbon dioxide reached the mole fraction value of 0.76% from 0.63%; the oxygen increased from 0.02% to 0.19%. The permeated oxygen at this point came from two sources, molten carbonate and mobile oxygen that crossed the membrane, and this could explain the fact that the ratio of carbon dioxide and oxygen was not the 2:1 that was expected according to the carbon dioxide transport mechanism (Fig. 6.1).

To show the kinetic experiment clearly, a leak-subtracted result is shown in Fig. 6.3 and focuses on the time during the oxygen kinetic experiment period. In Fig. 6.3, periods a, b, c, d, e, and f correspond to 2%, 4%, 6%, 8%, 10%, and 12% oxygen put into the feed-side of the reactor, respectively, while the carbon dioxide stayed at 20%. It is clear that, with the increase of oxygen fed to the feed-side of the membrane from 2% to 12%, carbon dioxide permeation increased correspondingly at each step when the oxygen partial pressure rose to a higher value. Thus, the oxygen partial pressure gradient is considered a driving force for carbon dioxide permeation, as it accelerated the carbon dioxide permeation. A 20% carbon dioxide feed with 2%, 4%, 6%, 8%, 10%, and 12% oxygen separately gave a carbon dioxide permeance of $9.57 \times 10^{-8} \text{ mol m}^{-2} \text{ s}^{-1} \text{ Pa}^{-1}$, $1.06 \times 10^{-7} \text{ mol m}^{-2} \text{ s}^{-1} \text{ Pa}^{-1}$, $1.15 \times 10^{-7} \text{ mol m}^{-2} \text{ s}^{-1} \text{ Pa}^{-1}$, $1.22 \times 10^{-7} \text{ mol m}^{-2} \text{ s}^{-1} \text{ Pa}^{-1}$,

Chapter 6. Kinetics and the limiting step for CO₂ permeation

$1.28 \times 10^{-7} \text{ mol m}^{-2} \text{ s}^{-1} \text{ Pa}^{-1}$, and $1.37 \times 10^{-7} \text{ mol m}^{-2} \text{ s}^{-1} \text{ Pa}^{-1}$, respectively, while the carbon dioxide permeance without oxygen feeding was $7.66 \times 10^{-8} \text{ mol m}^{-2} \text{ s}^{-1} \text{ Pa}^{-1}$.

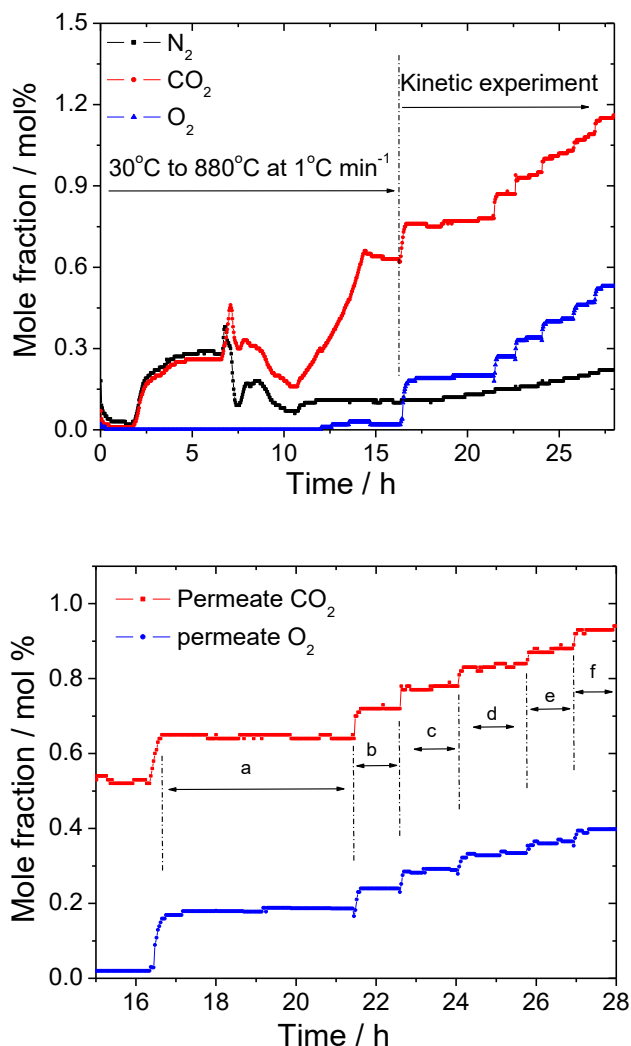


Figure 6.3 Mole fraction of N₂, CO₂, and O₂ in the permeate side of the membrane. Period a, b, c, d, e, and f correspond to 2%, 4%, 6%, 8%, 10%, and 12% oxygen put into the feed side of the reactor, while the carbon dioxide stayed at 20%.

The increases in carbon dioxide and oxygen permeation refer to oxygen feeding and are presented in the table below.

Table 6.3 Permeation results for CO₂ and O₂ when the feed-side O₂ mole fraction was increased.

Feeding Oxygen (%)	Mole Fraction of Permeate CO ₂ (%)	CO ₂ Permeance (mol m ⁻² s ⁻¹ Pa ⁻¹)	Mole Fraction of Permeate O ₂ (%)	O ₂ Permeance (mol m ⁻² s ⁻¹ Pa ⁻¹)
0	0.53	7.66×10^{-8}	0.02	0
2	0.65	9.57×10^{-8}	0.18	2.65×10^{-7}
4	0.72	1.06×10^{-7}	0.24	1.76×10^{-7}
6	0.78	1.15×10^{-7}	0.29	1.42×10^{-7}

8	0.83	1.22×10^{-7}	0.33	1.21×10^{-7}
10	0.87	1.28×10^{-7}	0.36	1.06×10^{-7}
12	0.93	1.37×10^{-7}	0.39	9.57×10^{-8}

It is obvious that the carbon dioxide permeation rate, referring to the permeate side is in direct proportion to the oxygen partial pressure in the feed side. The relationship between carbon dioxide permeation and oxygen partial pressure from the feed side is presented in Fig. 6.4. The mole ratio of permeated carbon dioxide and oxygen from the permeate side of the membrane was estimated to be 3.5 at the beginning of the experiment; then it decreased gradually after 2% oxygen was introduced to the feed side of the membrane and was followed by 4%, 6%, 8%, 10%, and 12% oxygen fed into the feed side of the membrane. The ratio between permeated carbon dioxide and oxygen declined with each step when more oxygen was provided (Fig. 6.5).

The experiment indicated that carbon dioxide permeation increased when the oxygen partial pressure gradient was introduced to the system.

The oxygen has two ways to cross the membrane at 880°C; first, the oxide ions are formed by oxygen molecules and combine with carbon dioxide to form carbonate ions, which cross the membrane via molten carbonate and release carbon dioxide and oxygen in the permeate side of the membrane. Second, the membrane substrate transports oxygen by itself at this temperature. There is another possibility: that oxide ions do not permeate across the membrane; they may be cycled in the substrate to form carbonate ion and release carbon dioxide in the permeate side and back to the feed side continuously.

The increase of carbon dioxide permeation in Fig. 6.4 is constructed based on Table 6.3, which shows that the carbon dioxide permeation had a large improvement when 2% oxygen was introduced into the feed side of the reactor; the carbon dioxide in the permeate side increased from 0.53% to 0.65%, a 0.12% increase in carbon dioxide. Then, the increases were 0.07%, 0.06%, 0.05%, 0.04%, and 0.06%, caused by the increasing oxygen partial pressure gradient. Similarly, the oxygen concentration in the permeate side of the membrane increased first from 0.02% to 0.18% and then increased less and less. It seems that the oxygen did not cross the membrane on its own; it improved the carbon dioxide permeation and crossed the membrane by combining with carbon dioxide to form carbonate ions. There is still a possibility that some oxygen

molecules cross the membrane by the membrane substrate only because of the ion-conducting properties that emerge at this temperature.

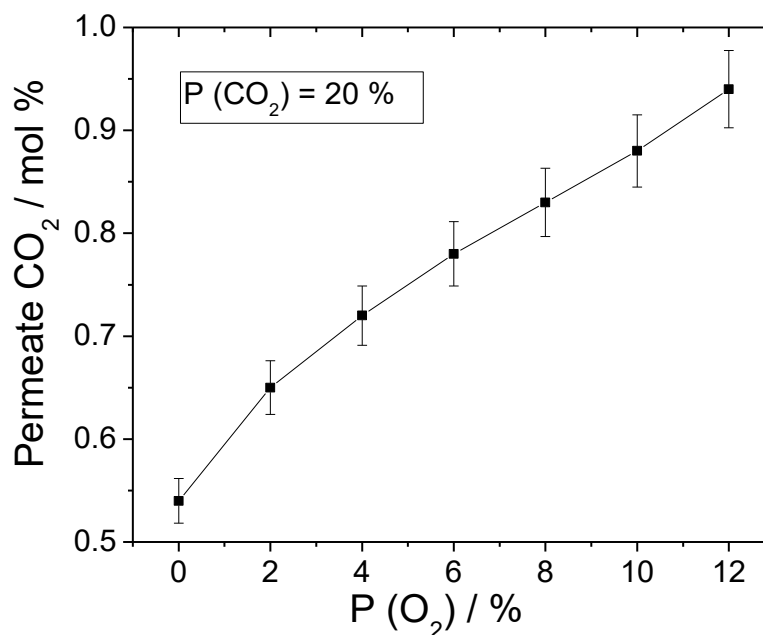


Figure 6.4 The CO₂ mole fraction in the permeate side corresponds to the O₂ partial pressure increase in the feed side; 20% CO₂ is provided in the feed side. The x-axis is the oxygen partial pressure gradient, which is equal to ΔP_{O_2} ; the y-axis is the permeate (leakage subtracted) CO₂ mole fraction in the permeate side ($\pm 5\%$ error).

To determine what mechanism dominated the carbon dioxide permeation, a ratio of carbon dioxide and oxygen in the permeate side of the membrane was established according to the oxygen concentration decreasing in the feed side, as shown in Fig. 6.5, which relates to Fig. 6.3. This shows that, during the period when 2% oxygen was provided in the feed side of the membrane, the ratio between carbon dioxide and oxygen in the permeate side of the membrane was more or less stable at 3.5:1 rather than 2:1; as the oxygen partial pressure increased, the ratio of carbon dioxide and oxygen in the permeate side decreased and finally reached 2.4:1. This result demonstrated that the carbon dioxide permeation mechanism shown in Fig. 6.1(a) dominated the permeation process, with no oxygen crossing the membrane; a little oxygen crossed the membrane either by the pure ion-conducting membrane substrate or the mechanism shown in Fig. 6.1(b). As the oxygen concentration increased in the feed side of the membrane, the oxygen permeation increased, and the ratio of carbon dioxide and oxygen in the permeate side finally decreased to 2.4:1; it seems that the oxygen permeation dominated the process, and the carbon dioxide permeation increased less than expected. The

mechanism shown in Fig. 6.1(b) dominated the permeation of carbon dioxide and oxygen.

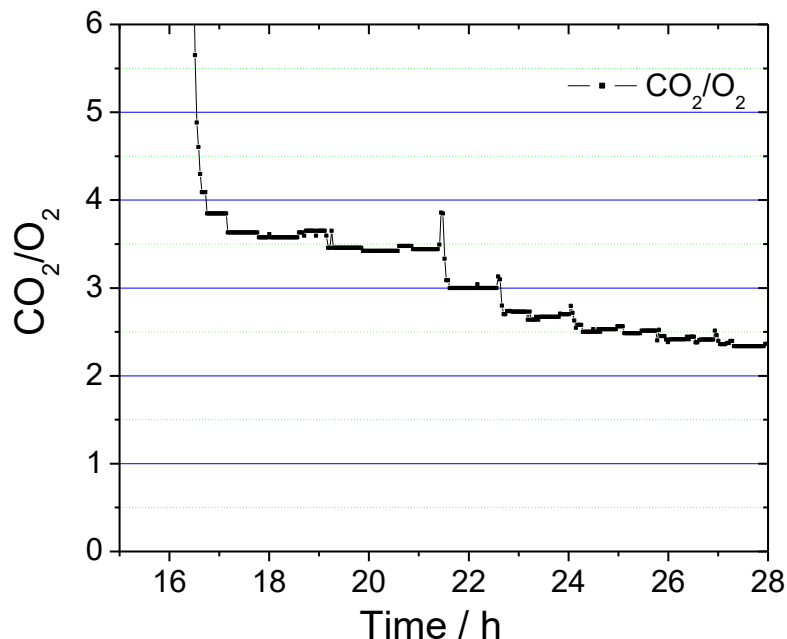


Figure 6.5 The ratio of CO₂/O₂ in the permeate side of the membrane from Fig. 6.3; 2% oxygen was introduced to the feed side of the membrane and followed by 4%, 6%, 8%, 10%, and 12% oxygen fed into the feed side of the membrane.

Experiment 2: CO₂ permeation as a function of CO₂ partial pressure in the feed side

Experiment 2 was started when the prepared dual-phase membrane was heated from the temperature of 30°C at a ramp of 2°C min⁻¹ to 880°C; the carbon dioxide kinetic experiment was carried out at the same temperature. The gas provided to the feed side of the membrane initially during the heating process was 40% carbon dioxide, 40% nitrogen, and 4% oxygen in argon from cylinder C-1 and C-2, controlled by MFC-1 and MFC-2. Cylinder C-3, which contained pure helium, was used to balance the feed gas when the mole fraction of carbon dioxide was reduced for the kinetic experiment. Pure helium as a carrier gas was fed to the permeate-side chamber of the membrane, which was the data collection chamber for gas analysis. The total flow rate for both the feed and permeate sides was 20 (STP) ml min⁻¹, which is the same as experiment 1 for carbon dioxide permeation comparison.

The aim of this experiment was to investigate the influence of the carbon dioxide driving force between the two chambers of the dual-phase membrane on carbon dioxide

permeability, with 4% oxygen provided to the feed side of the membrane. Fig. 6.6 below shows the raw data for the mole fraction of each component from the permeate side of the membrane, starting from the initial heating process.

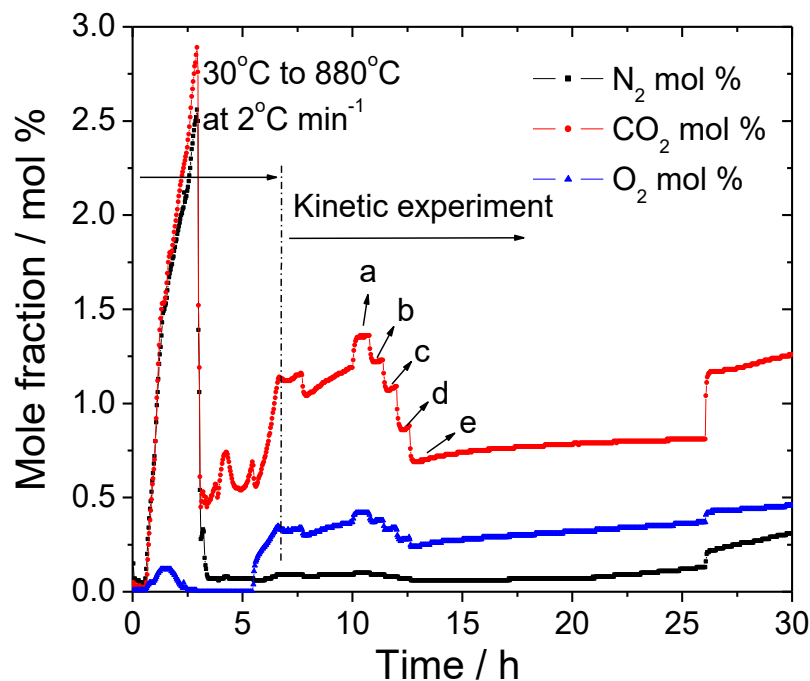


Figure 6.6 Mole fractions of N₂, CO₂, and O₂ in the permeate side of the membrane.

In the first three hours, the carbon dioxide and nitrogen increased significantly and reached 2.9% and 2.6%, respectively, while there was no carbon dioxide permeation at temperatures below 500°C; it was considered that a leak development caused the carbon dioxide and nitrogen free diffusion from the feed side of the membrane to the permeate side owing to the large partial pressure gradient of carbon dioxide and nitrogen. This is because the silver-based sealant did not start to work below 500°C. The extra carbon dioxide from bicarbonate decomposition during the heating process also occurred at the same time that the sealant started to seal the membrane.

After three hours' heating at a temperature of around 400°C, the sealing improved dramatically and the nitrogen from the feed side of the membrane (40% nitrogen in the feed side) via leak decreased rapidly, from 2.6% to 0.07%, and was steady at 0.07 after a tiny fluctuation after 12 hours. Generally, the sealing system is perfect to ensure that the carbon dioxide permeation occurs in the following experiment other than via cross-chamber leakage from the feed side, which had 40% carbon dioxide initially.

It can be noted that, after 6 hours of heating, the oxygen started to permeate at a temperature of around 700°C, together with a significant increase in carbon dioxide permeation. Between 7 and 10 hours, there was a drop in carbon dioxide permeation because an inappropriate early operation started before the steady state, which caused 30% carbon dioxide to be provided to the feed side instead of 40%. The carbon dioxide kinetic experiment started after 10 hours of heating with the temperature steady at 880°C; the leak corrected the carbon dioxide and oxygen permeation. These data are presented in Fig. 6.7 below. Here, the time periods a, b, c, d, and e correspond to 40%, 30%, 20%, 10%, and 5% carbon dioxide going to the feed side of the membrane with 4% oxygen. The data collected in the permeate side show that the permeated carbon dioxide and oxygen are 1.25% and 0.42% in zone 'a' with 40% carbon dioxide in the feed side, 1.13% and 0.38% in zone 'b' with 30% carbon dioxide in the feed side, 0.99% and 0.33% in zone 'c' with 20% carbon dioxide in the feed side, 0.79% and 0.28% in zone 'd' with 10% carbon dioxide in the feed side, and 0.63% and 0.24% in zone 'e' with 5% carbon dioxide in the feed side. The decrease of both carbon dioxide and oxygen permeation responds to carbon dioxide partial pressure drops in the feed side of the membrane, when the oxygen provided in the feed side was 4% at 880°C. It can be noted that the oxygen permeation rate also decreased when the feeding carbon dioxide dropped; the oxygen put into the feed side of the membrane was 4% during the heating process and the kinetic experiment.

The carbon dioxide and oxygen permeance decreases according to the carbon dioxide feeding decrease is presented in the table below.

Table 6.4 Permeation results of CO₂ and O₂ in the permeate side of the membrane corresponding to the CO₂ mole fraction decreasing in the feed side.

Carbon Dioxide Feeding (%)	Mole Fraction of Permeate CO ₂ (%)	CO ₂ Permeance (mol m ⁻² s ⁻¹ Pa ⁻¹)	Mole Fraction of Permeate O ₂ (%)	O ₂ Permeance (mol m ⁻² s ⁻¹ Pa ⁻¹)
40	1.25	9.21 × 10 ⁻⁸	0.42	3.10 × 10 ⁻⁷
30	1.13	1.11 × 10 ⁻⁷	0.38	2.80 × 10 ⁻⁷
20	0.99	1.46 × 10 ⁻⁷	0.33	2.43 × 10 ⁻⁷
10	0.79	2.33 × 10 ⁻⁷	0.28	2.06 × 10 ⁻⁷
5	0.63	3.71 × 10 ⁻⁷	0.24	1.77 × 10 ⁻⁷

The experiment showed that not only the permeated carbon dioxide but also the permeated oxygen responded according to the decline of carbon dioxide feeding. The permeated oxygen that crossed the membrane was highly related to the carbon dioxide

permeation, which proves the mechanism of carbon dioxide transportation by only an electronic conducting membrane (Fig. 6.1(b)) at temperatures below 700°C, at which the oxygen cannot permeate on its own.

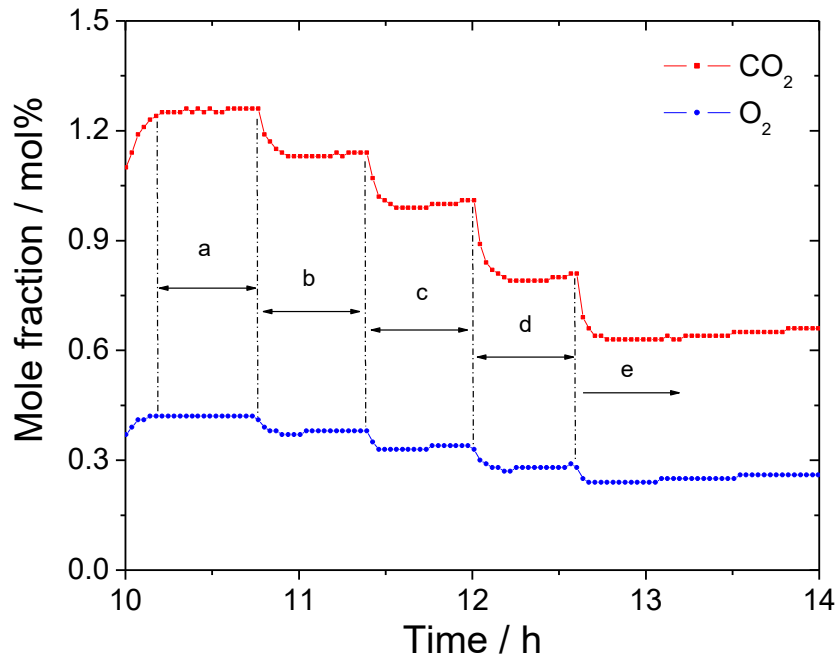


Figure 6.7 Leak-corrected CO₂ and O₂ mole fractions in the permeate side of the membrane as the feed CO₂ decreased from 40% to 5%; time periods a, b, c, d, and e correspond to 40%, 30%, 20%, 10%, and 5% carbon dioxide, respectively, going to the feed side of the membrane with 4% oxygen.

The carbon dioxide permeation rate as a function of the carbon dioxide partial pressure in the feed side is shown in Fig. 6.8. The increases in the carbon dioxide permeation rate in the mole fraction are 0.16%, 0.2%, 0.14%, and 0.12% when the partial pressure of carbon dioxide in the feed side increased from 5% to 10%, 10% to 20%, 20% to 30%, and 30% to 40%. The carbon dioxide permeation rate increased the most when the carbon dioxide partial pressure in the feed side increased from 10% to 20%, and then the increases decreased gradually. It can be estimated that increasing the partial pressure of feed carbon dioxide will not provide the same driving force as at the beginning.

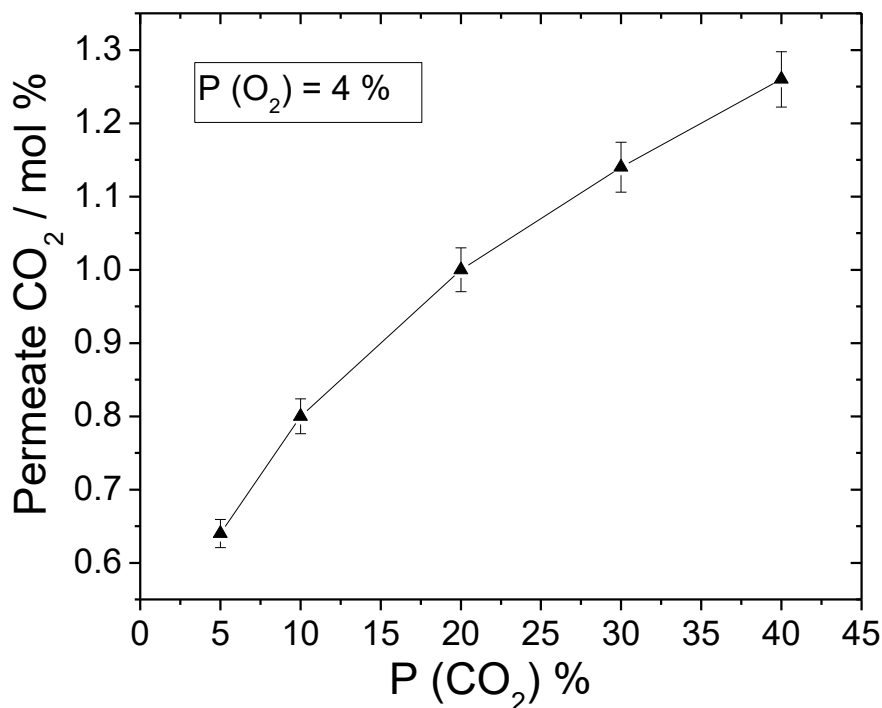


Figure 6.8 The CO₂ mole fraction in the permeate side corresponding to the CO₂ mole fraction in the feed side; refer to Fig. 6.7 ($\pm 3\%$ error).

The ratio of permeated carbon dioxide and oxygen was also calculated and is shown in Fig. 6.9; the times between 10 and 14 hours from the beginning refer to the kinetic experiment shown in Fig. 6.7. The ratio between carbon dioxide and oxygen stayed at 3:1 for an hour at the beginning of the kinetic experiment after 10 hours and then decreased gradually to 2.5:1 after about 15 hours as the partial pressure of the feed carbon dioxide decreased from 40% to 5%. This indicates that, in conditions of high carbon dioxide partial pressure in the feed side, the carbon dioxide permeated across the membrane by carbonate ion transportation with oxygen ion diffusion in the opposite direction. That is why the ratio between permeated carbon dioxide and oxygen is higher than 2:1; as the temperature decreased, the carbon dioxide in the feed side reacted with oxygen molecules rather than oxygen ions from the membrane substrate.

The gradual decline of the ratio of carbon dioxide and oxygen may have occurred because the oxygen permeation through the membrane substrate replaced the permeation through carbonate ions; also, the leak slowly increased after 22 hours (Fig. 6.6).

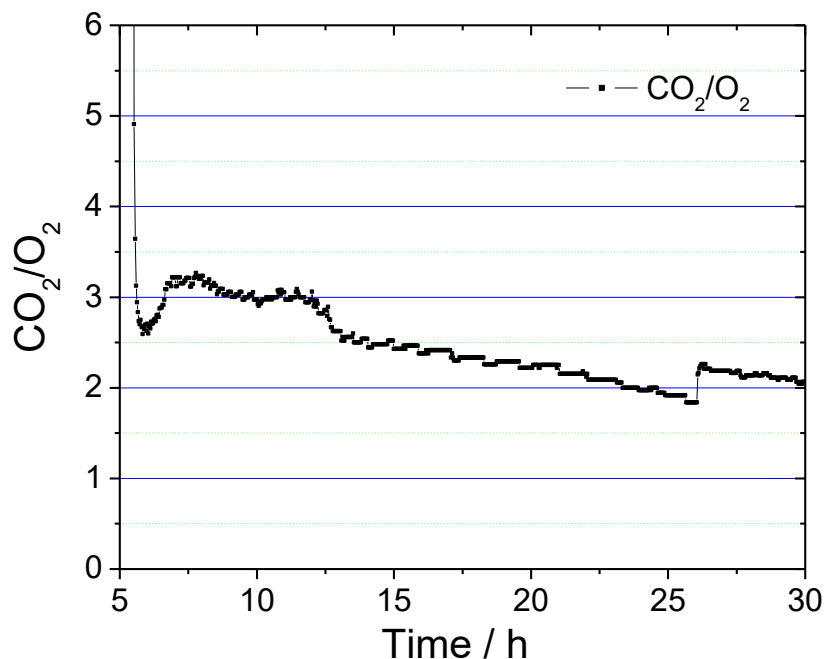


Figure 6.9 Ratio of CO₂/O₂ in the permeate side of the membrane when the CO₂ mole fraction in the feed side changed following Fig. 6.6.

Experiment 3: Limiting step for CO₂ permeation

Another two similar experiments were also performed, using cylinder C-1 (CO₂ and N₂, ratio of 1:1) diluted with 20% oxygen in argon and pure helium, respectively, to see how large the oxygen driving force was that could push carbon dioxide permeation when the carbon dioxide partial pressure decreased, and this was compared with the reference test using helium instead of oxygen.

It can be noted from the results shown in Fig. 6.10 that the carbon dioxide permeation decreased from 0.7% to 0.02% when the partial pressure of carbon dioxide in the feed side was diluted by helium from 50% to 10%, but it was obviously a different situation when it was diluted by 20% oxygen, as the carbon dioxide partial pressure decreased from 50% to 12%, while the carbon dioxide permeation increased a small amount and almost maintained the carbon dioxide permeation. Even at 10% partial pressure of carbon dioxide in the feed side, the permeated carbon dioxide was still higher than 0.8%, while the permeated carbon dioxide, which was also fed 10% carbon dioxide, but with helium, was only 0.02%. This confirmed that the oxygen partial pressure gradient that provided the driving force for carbon dioxide permeation was much higher than the driving force from the carbon dioxide partial pressure difference.

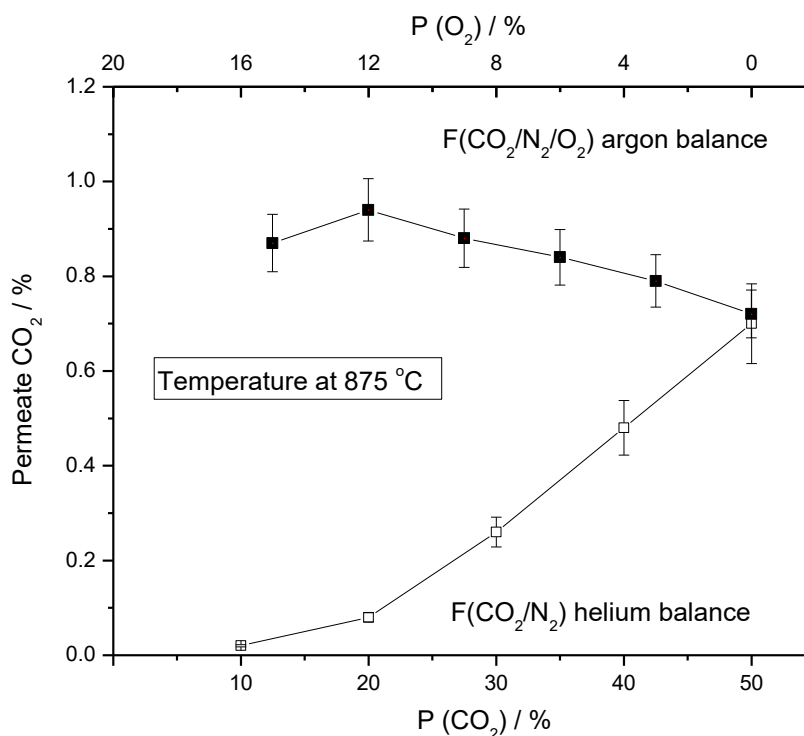


Figure 6.10 CO₂ mole fraction in the permeate side of the membrane with different O₂ partial pressures in the feed side and the CO₂ mole fraction in the permeate side with helium replacing O₂ in the feed side; ■ indicates the permeated CO₂ ($\pm 7\%$ error) when CO₂ in the feed side was diluted by O₂; □ indicates the permeated CO₂ ($\pm 12\%$ error) when CO₂ in the feed side was diluted by helium.

6.4 Discussion

Oxygen ion transportation as the main driving force for CO₂ permeation in the LSCF-carbonate membrane was investigated, and the mechanism of O₂ and CO₂ co-permeation at 890 °C is presented in Fig. 6.11. The CO₂ reacts with oxygen ions on LSCF lattice sites (structural oxygen) and forms carbonate ions and oxygen vacancies; these oxygen vacancies become oxygen ions on the lattice again when the carbonate released CO₂ in the permeate side. When O₂ is provided in the feed side, the O₂ can take the oxygen vacancies and become oxygen ions on the lattice, and this increases the number of oxygen ions in the LSCF, the increasing of oxygen ions on the lattice accelerates the reaction between CO₂ and oxygen ions in step 1 in the interface between the feed-side gas and the molten carbonate phase. The oxygen ions release gas-phase O₂ in the permeate side and produce oxygen vacancies at the same time. An oxygen vacancy is one of the reactants of a reaction between CO₃²⁻ and an oxygen vacancy (V_O^{••}); therefore, the reaction step 2 in the molten phase shown in Fig. 6.11 is accelerated. It can be concluded that both reaction step 1 (CO₂ and O_O^X) and reaction step 2

(CO_3^{2-} and $V_{\ddot{O}}$) are accelerated by increasing O_O^X and $V_{\ddot{O}}$ in step 1 and step 2, respectively. If only the CO₂ mole fraction increased, reaction step 1 shown in Fig. 6.11 will be accelerated but step 2 will not be accelerated without oxygen. The experiments in this chapter also showed that O₂ in the feed side increases the CO₂ permeation rate significantly and even decreases the CO₂ partial pressure gradient. The O₂ can accelerate both reaction step 1 and step 2 by increases in O_O^X and $V_{\ddot{O}}$; if the CO₂ partial pressure gradient is increase without introducing O₂, only step 1 can be accelerated.

It also can be concluded that the transfer rate (bulk diffusion; see Fig. 2.6 in Chapter 2) of the oxygen ions on lattice O_O^X and the oxygen vacancy $V_{\ddot{O}}$ are the critical factors that determine the CO₂ permeation.

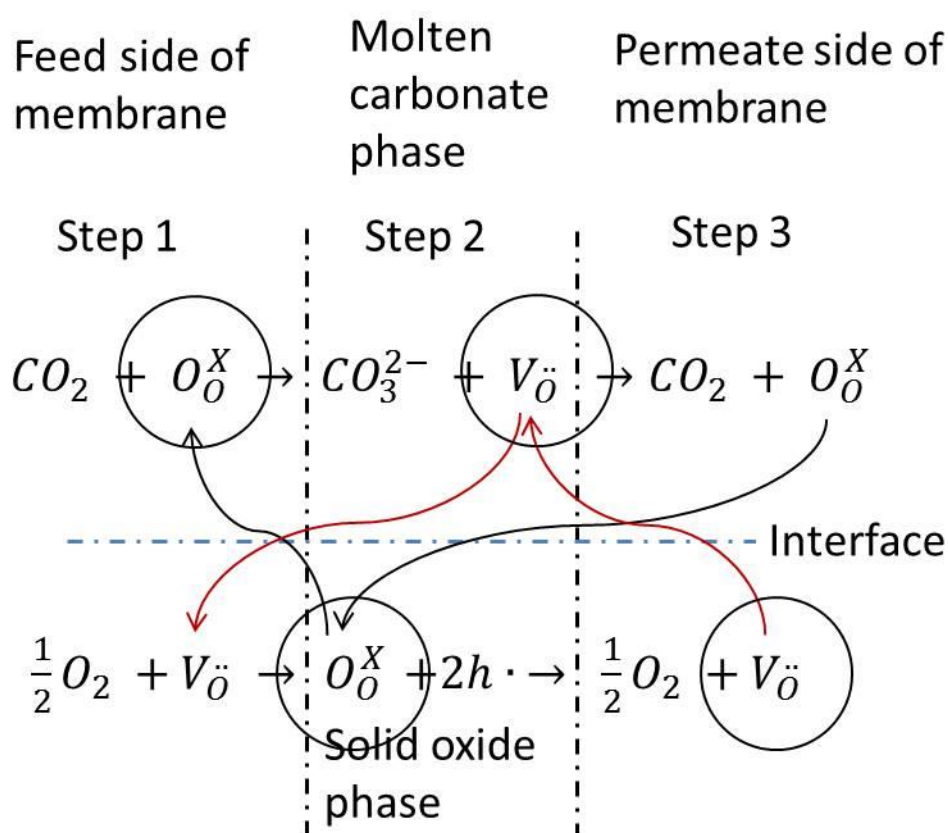


Figure 6.11 The mechanism of CO₂ and O₂ co-permeation at 890°C; the O₂ in the feed side was found to have the ability to accelerate the CO₂ permeation rate.

There is another mechanism for CO₂ permeation at lower temperatures such as 600°C. The reaction between oxygen ions and oxygen vacancies is limited and can be ignored at 600°C; the LSCF membrane works as an electron-conducting membrane. Fig. 6.12 below shows the mechanism of CO₂ and O₂ co-permeation at 600°C; it is similar to Fig. 6.11, but only carbonate ions are formed in molten phase carbonate. O₂ can still increase the CO₂ permeation rate, but the electron conductivity is the limiting step to form O^{2-} .

Chapter 7 introduces the up-hill CO₂ permeation using this mechanism at 600°C and creates an O₂ partial pressure gradient against a CO₂ partial pressure gradient. Both Fig. 6.11 and Fig. 6.12 can achieve CO₂ and O₂ co-permeation, but Fig. 6.12 works at lower temperatures and has a simpler process than Fig. 6.11.

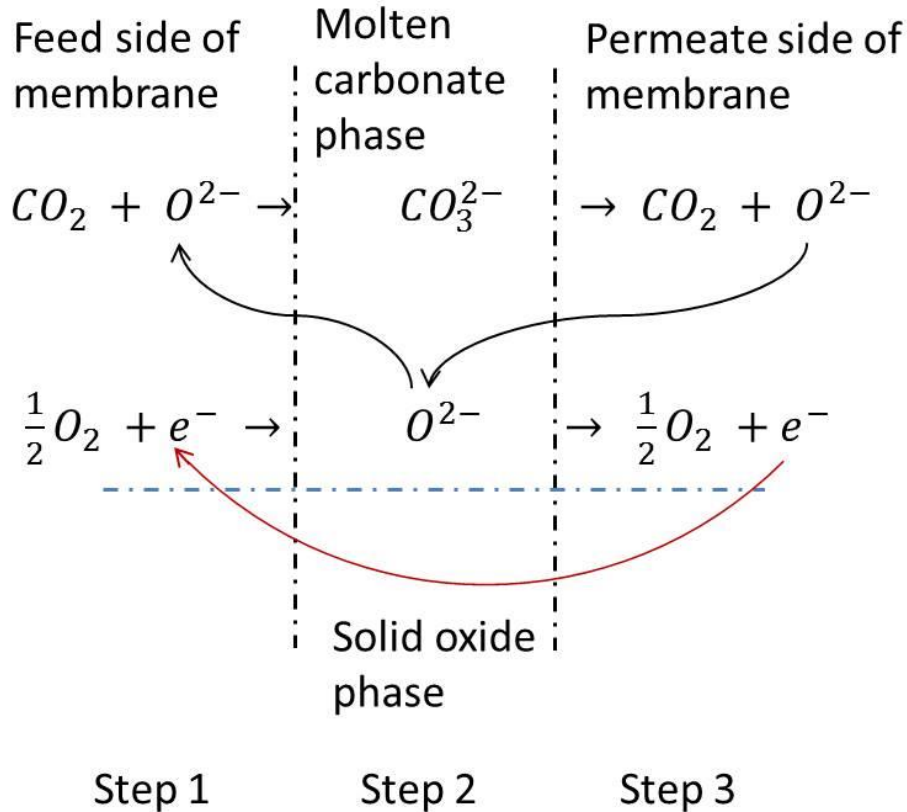


Figure 6.12 The mechanism of CO₂ and O₂ co-permeation at 600°C.

6.5 Conclusion

The partial pressure of oxygen $P(\text{O}_2)$ played an important role in the CO₂ permeation experiments at high temperatures. The structural oxygen (oxygen ion on LSCF lattice site) becomes mobile at temperatures over 700°C, and there are two states on the LSCF lattice that involve oxygen ions: structural oxygen ions O_O^\times (mobile) and oxygen vacancies $\text{V}_\text{O}^\bullet$. O_O^\times will react with CO₂ and $\text{V}_\text{O}^\bullet$ with O₂, respectively. $P(\text{O}_2)$ increases O_O^\times on the surface of the membrane in the feed side and reacts with CO₂ to produce CO_3^{2-} and $\text{V}_\text{O}^\bullet$. It can be concluded that the oxygen accelerated CO₂ permeation by increasing

Chapter 6. Kinetics and the limiting step for CO₂ permeation

O_O^X inside the LSCF lattice at the temperature that structural oxygen ions become mobile.

At low temperatures, when the mobility of structural oxygen ions is not activated, the CO₂ and O₂ co-permeation is limited by the electron conductivity of the membrane substrate material, as Fig. 6.12 presented. The CO₂ permeation can be accelerated by increasing $P(O_2)$ in the feed side or increasing electron conductivity; both methods can increase O²⁻ ions in the feed side of the membrane and make the reaction $CO_2 + O^{2-} \leftrightarrow CO_3^{2-}$ move from left to right.

Chapter 7 Up-hill CO₂ permeation

7.1 Introduction

The up-hill permeation experiments are described in this chapter. These experiments were carried out at one atmosphere pressure with continuous gas flow supplied by mass flow controllers to the membrane system. The gas composition was considered uniform because of the small membrane area of about 0.5 cm², and there was no great change in gas composition and gas volume in the outlet from either the feed side or permeate side of the membrane. That is, the gas flow rate for both sides of the membrane was constant; as the permeated carbon dioxide volumetric flow from the feed side to the permeate side was extremely small compared to the total flow rate, the outlet flow rates from both sides of the membrane were considered equivalent to the inlet flow rate for the permeability calculation. However, when a large membrane area is subjected to the same gas flow rate, there would be a different situation for calculating permeability because of the change in the gas composition and the volume increase of permeated carbon dioxide in the permeate side. For this experiment, the gas composition feeds to both sides of the membrane with 1% carbon dioxide and flow rates were controlled by a mass flow controller; different from a normal down-hill permeation, two mass spectrometers of similar type and condition were used to analyse the gas composition from the outlet of the feed side and the permeate side, respectively. The permeated carbon dioxide can be clearly demonstrated by decrease in the mole fraction in the feed side and a corresponding increase in the permeate side of the membrane. The down-hill permeation membrane experiment analyses only the permeate side of the membrane because the permeation requires a large potential gradient. The feed-side gas inlet composition normally contains a significant mole fraction of carbon dioxide, and a tiny change can be detected easily only from the permeate side of the membrane, where pure helium or argon is normally used as a carrier gas with free carbon dioxide. The experiments clearly demonstrated dynamic gas composition changes from both the feed side and permeate side of the membrane.

Moreover, symmetric switching to a non-permeation condition was also applied to the feed side during the experiment to investigate and demonstrate up-hill permeation; that

is, the feed-side inlet was switched to the same condition (the same component and mole fraction as the permeate inlet gas) as the permeate side during up-hill permeation. Correspondingly, a gas composition change could be detected in the permeate side of the membrane, which involves the feed side switching to a symmetric condition; the carbon dioxide mole fraction change in the permeate side of the membrane is considered the up-hill permeated carbon dioxide. During the symmetric condition, there was no up-hill permeation, and it could be considered a reference condition to the up-hill permeation step. The difference in carbon dioxide mole fractions between the symmetric condition and the up-hill condition could be calculated to estimate the permeability of the membrane. The measurements were very accurate compared to those in other literature because of the reference condition applied, and the data points collected from both the feed-side outlet and the permeate-side outlet are at the same time with the known inlet composition. To demonstrate the up-hill permeation clearly, a relatively high ratio of oxygen to carbon dioxide in a 20:1 mole fraction gas mixture was prepared and used for the feed-side inlet of the membrane, which is 20% oxygen with 1% carbon dioxide. Here, extremely high carbon dioxide permeation was performed with the permeance on the order of $10^{-6} \text{ mol m}^{-2} \text{ s}^{-1} \text{ Pa}^{-1}$ in an experiment that operated for over 200 hours.

This experiment demonstrated up-hill permeation conclusively and proved the mechanism.

7.2 Experimental equipment

Porous La_{0.6}Sr_{0.4}Co_{0.2}Fe_{0.8}O_{3- δ} (LSCF6428) membrane substrates were prepared for CO₂ up-hill permeation. The membrane fabrication, infiltration, and sealing methods had been studied previously. The prepared membrane was polished to 1 mm thick, and the final membrane area for permeation was 0.5 cm². Each experiment was performed with a fresh membrane.

The permeation cell (Fig. 7.1) comprised a feed-side chamber and permeate-side chamber. All permeation experiments were carried out at atmospheric pressure.

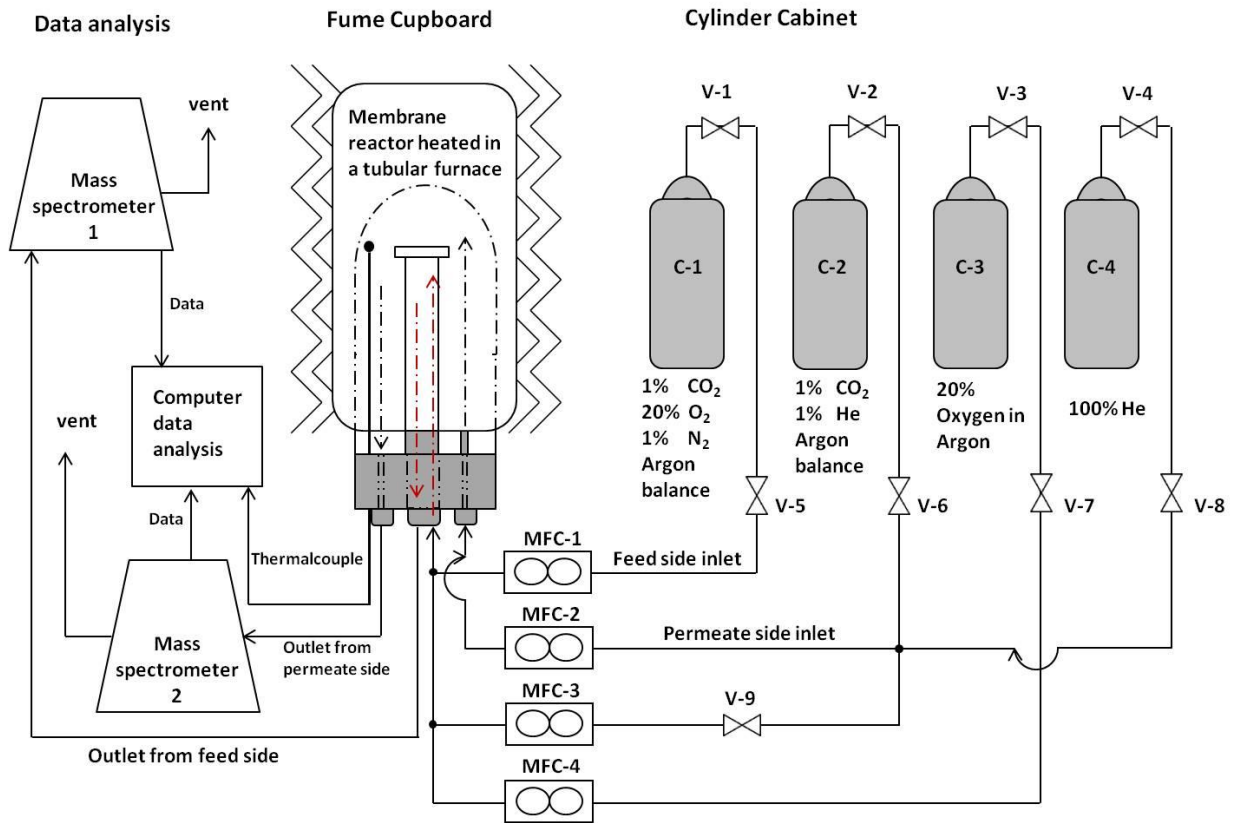


Figure 7.1 Schematic of the high-temperature CO₂ permeation setup.

The gases used for the permeation experiments and provided by BOC (certified gases, compositions on a molar basis) were 0.99% CO₂/1.03% N₂/19.45% O₂ in Ar (cylinder 1, C-1), 1.03% CO₂ in Ar (cylinder 2, C-2), 20% O₂ in Ar (cylinder 3, C-3), and pure Ar (cylinder 4, C-4). The nitrogen in cylinder 1 at approximately 1% was introduced to reveal cross-chamber leaks and in particular was chosen to be of a similar mole fraction to that of carbon dioxide in cylinder 1 to estimate any carbon dioxide leak rate from the feed side to the permeate side. During up-hill permeation, carbon dioxide was transported from low concentration to high concentration. Therefore, any leaks would counter the membrane transport of carbon dioxide and lead to an underestimate of membrane performance; unlike conventional down-hill permeation, the up-hill CO₂ permeation rate in the downstream side is unlikely to lead to misinterpretation owing to its opposite CO₂ potential.

The flows on both the feed and permeate sides were maintained at 20 cm³ (STP)/min ($1.49 \times 10^{-5} \text{ mol s}^{-1}$). The outlet gases from the feed and permeate sides were analysed using two identical mass spectrometers (HIDEN, HALO 100-RC), MS-1 on the feed-side outlet and MS-2 on the permeate-side outlet. Both mass spectrometers were calibrated prior to the experiments and appeared to have linear responses for

carbon dioxide mole fractions in the range of 0.5% to 1.5%. The carbon dioxide measured before starting experiment 1 was 0.97 for C-1 (using MS-1) and 1.04% for C-2 (using MS-2). It was noted that MS-1 measured the carbon dioxide mole fraction as low by 0.02% while MS-2 measured high by 0.01%. In addition, the resolution of the mass spectrometers was 0.01%.

To demonstrate clearly and conclusively the up-hill permeation experiment, we developed a way of switching gases in the feed side between an asymmetrical permeate condition and a symmetrical non-permeate condition. The composition of the permeate-side inlet gas was not changed during the experiment; by doing this, we could get the accurate permeation rate from the change in the permeate-side outlet gas composition.

7.3 Results and discussion

7.3.1 CO₂ permeation experiments

Experiment 1: CO₂ up-hill permeation from 0.90% to 1.15% at 600 °C

Gases from cylinder 1 (0.99% CO₂/1.03% N₂/19.45% O₂ in Ar) were introduced to the feed side and the gases from cylinder 2 (1.03% CO₂ in Ar) were introduced to the permeate side of the membrane; the furnace heating ramp was 2°C/min, starting from room temperature and increasing to 600°C. The asymmetrical condition in Fig. 7.2 led to up-hill permeation.

During the heating condition, there was CO₂ evolution from both sides of the membrane; starting from point t₁; at about t₁', a large CO₂ peak and a tiny N₂ peak could be observed in the feed side, followed by a dramatic decrease in the CO₂ mole fraction when the temperature reached 600°C because of the CO₂ permeation. At the time t₂ when the CO₂ in the permeate side stabilised (giving the same reading for 15 minutes), the CO₂ mole fraction in the feed-side outlet was 0.90% and below the inlet CO₂ mole fraction (0.97 ± 0.2); the 1.15% CO₂ in the outlet of the permeate side was above the inlet CO₂ mole fraction (1.04 ± 0.2). These mole fraction differences in both sides of the membrane cannot be attributed to uncertainty or error in the reading of the mass spectrometer system. The difference in systematic readings of the mass spectrometer in this mole fraction for the experiment was 0.03%, and there was a resolution of 0.01%. The CO₂ mole fraction in the feed-side chamber declined to a level below its inlet mole

fraction and in the other side above the CO₂ permeate inlet. Thus, it can be concluded that CO₂ permeation was taking place at this time.

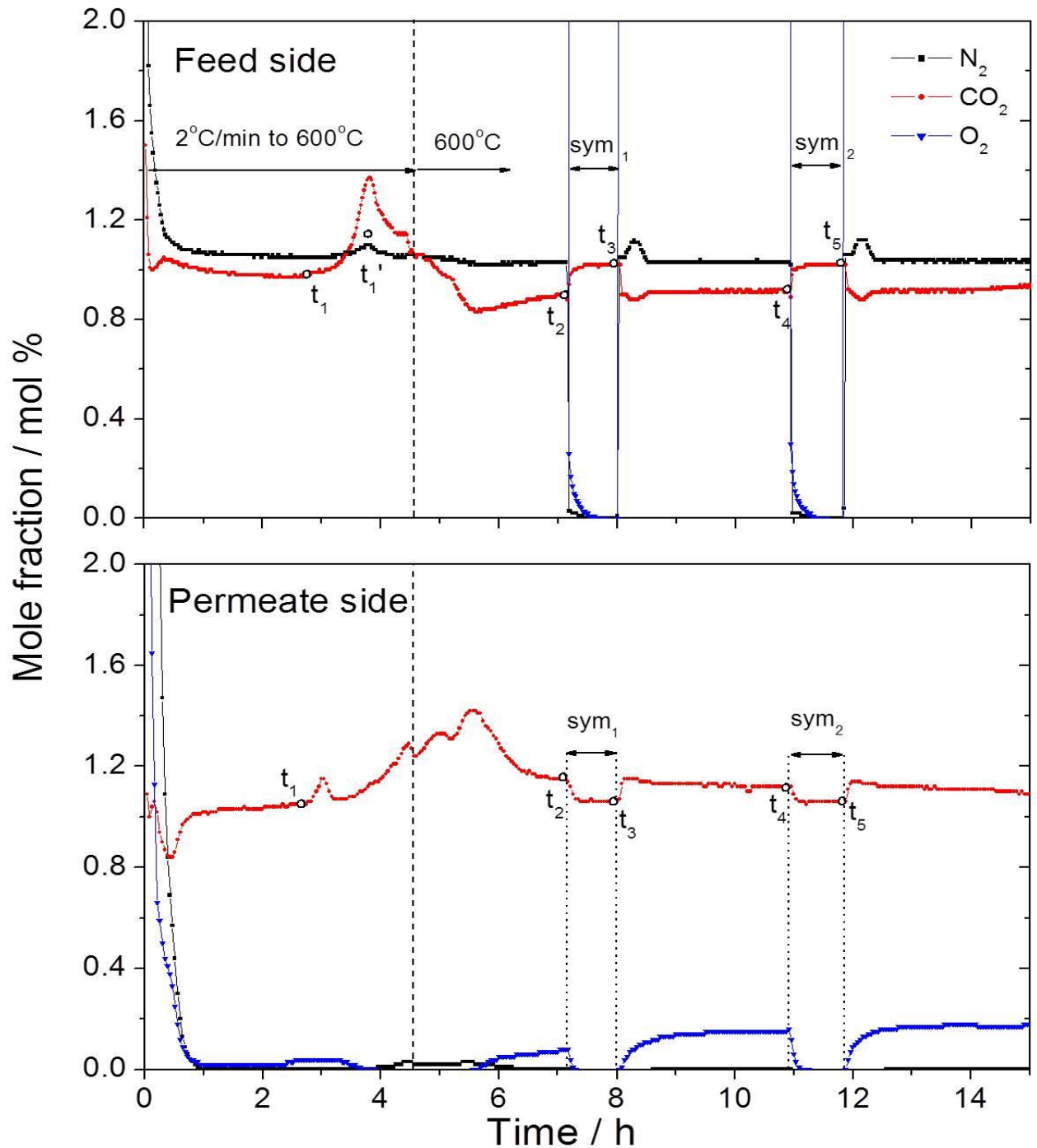


Figure 7.2 Mole fractions of gases in both the feed-side and permeate-side outlets for experiment 1. During asymmetrical operation: feed-side inlet: 0.99% CO₂/1.03% N₂/19.45% O₂ in Ar, permeate-side inlet: 1.03% CO₂ in Ar. During symmetrical operation: feed- and permeate-side inlets: 1.03% CO₂ in Ar. Note that the value for the oxygen mole fraction in the feed-side outlet during asymmetric operation is off scale.

Starting from time t_2 , an interrupt gas switching in the feed side was carried out and C-1 in the feed side was changed to C-2; by doing this, both sides of the membrane were fed with the same C-2 gas (symmetrical condition). During the symmetrical condition (as

indicated by 'sym₁' in Fig. 7.2), the CO₂ mole fraction in the outlet from the feed side of the membrane increased to 1.02%; as the figure shows, while the CO₂ mole fraction in the permeate-side outlet decreased to 1.06%. This can be considered the cessation of CO₂ permeation given the characteristics of gas analysis. In addition, the oxygen mole fraction decreased to zero, as no oxygen was fed to the feed-side. It should be noted that there was no gas composition change for the inlet of the permeate side. However, the CO₂ mole fraction in the outlet of the permeate side clearly shows that permeation occurred before t₂ and stopped shortly under non-permeation conditions.

After restoring the feed-side inlet gas from C-2 to C-1 at t₃, the CO₂ and N₂ mole fraction values on both sides of the membrane returned to values similar to those at t₂. Some nitrogen evolution on the feed side of the membrane following t₃ could be observed, which may be due to the loss of occupied gas from the pore network.

The CO₂ permeation rate of this experiment could be determined by the data at time t₄ and t₅, which was $9 \pm 2 \times 10^{-9}$ mol s⁻¹, or flux of $1.8 \pm 0.3 \times 10^{-4}$ mol m⁻² s⁻¹. During the CO₂ permeation condition between time t₃ and t₄, 0.15% oxygen could be observed in the permeate-side outlet; this is much higher than would be expected if the oxygen were only from carbonate ions (CO₃²⁻) across the membrane during CO₂ permeation according to the mechanism, and there was no neutral CO₂ and oxygen mobility in the membrane at this temperature. It could also be noted that the LSCF6428 membrane had large oxygen permeation that could be observed when the temperature was over 700°C. However, it has been found by other researchers that CO₂ on the surface of the condensed molten carbonate could be absorbed and form C₂O₅²⁻ species and be able to diffuse within the molten phase carbonate [98]. We have already studied and understood the mechanism of CO₂ separation in the dual-phase membrane system. It could also be supposed that C₂O₅²⁻ inside molten carbonate transports CO₂ as it is by CO₃²⁻; the difference is C₂O₅²⁻ formation without gaseous O₂. Because the up-hill CO₂ permeation created a CO₂ potential, CO₂ diffusion against up-hill permeation could occur. If the CO₂ that separated to the permeate side went back to the feed side without co-diffusion with oxygen, the CO₂ permeation would decline and oxygen in the permeate side would increase. Fig. 7.2 shows that CO₂ permeation was decreasing before t₂ and stabilised at the time between t₃ and t₄; oxygen in the permeate side increased during the CO₂ permeation decline.

Experiment 2: 216-hour long-term CO₂ up-hill permeation

Experiment 2 started with the symmetrical condition, as indicated by sym₁ in Fig. 7.3(a), and the gas from cylinder C-2 (1.03% CO₂ in Ar) was fed to both sides of the membrane. The experiment operated at 1 atmosphere pressure. The CO₂ mole fraction at steady state measured in the outlet of the feed side was 1.02%, while the CO₂ mole fraction in the permeate side was measured at 1.06%. This measurement was taken at 600°C, and no permeation occurred because a symmetrical condition was applied. The heating steps from room temperature to 600°C, similar to that of experiment 1, are not shown.

After introducing gases from cylinder C-1 (0.99% CO₂/1.03% N₂/19.45% O₂ in Ar) to the feed side of the membrane at time t_1 , in the outlet of the feed side and the permeate side, the change in the value of the CO₂ mole fraction was measured to 0.91% and 1.12%, respectively. Similar to experiment 1, the CO₂ mole fraction overshoot its steady-state value in the permeate side when switching gas in the feed side from symmetrical to asymmetrical condition. Nitrogen evolution could also be detected at the same time. The whole experiment started with the symmetrical condition showing a similar CO₂ permeation rate to that of experiment 1, beginning with an asymmetrical condition, and the results cannot be attributed to measurement uncertainty or systematic error, although the CO₂ permeation rate in the mole fraction values are close to the resolution. A the CO₂ permeation rate of $9 \pm 2 \times 10^{-9}$ mol s⁻¹ can be calculated from t_2 and t_3 . The permeation rate from this experiment was used to determine the CO₂ permeance of -1.1×10^{-6} mol m⁻² s⁻¹ Pa⁻¹. The permeance value calculated here was negative because, in up-hill permeation, CO₂ transport across the membrane against its own partial pressure difference of -170 Pa between the feed side and permeate side and the CO₂ mole fraction difference was about 0.17%.

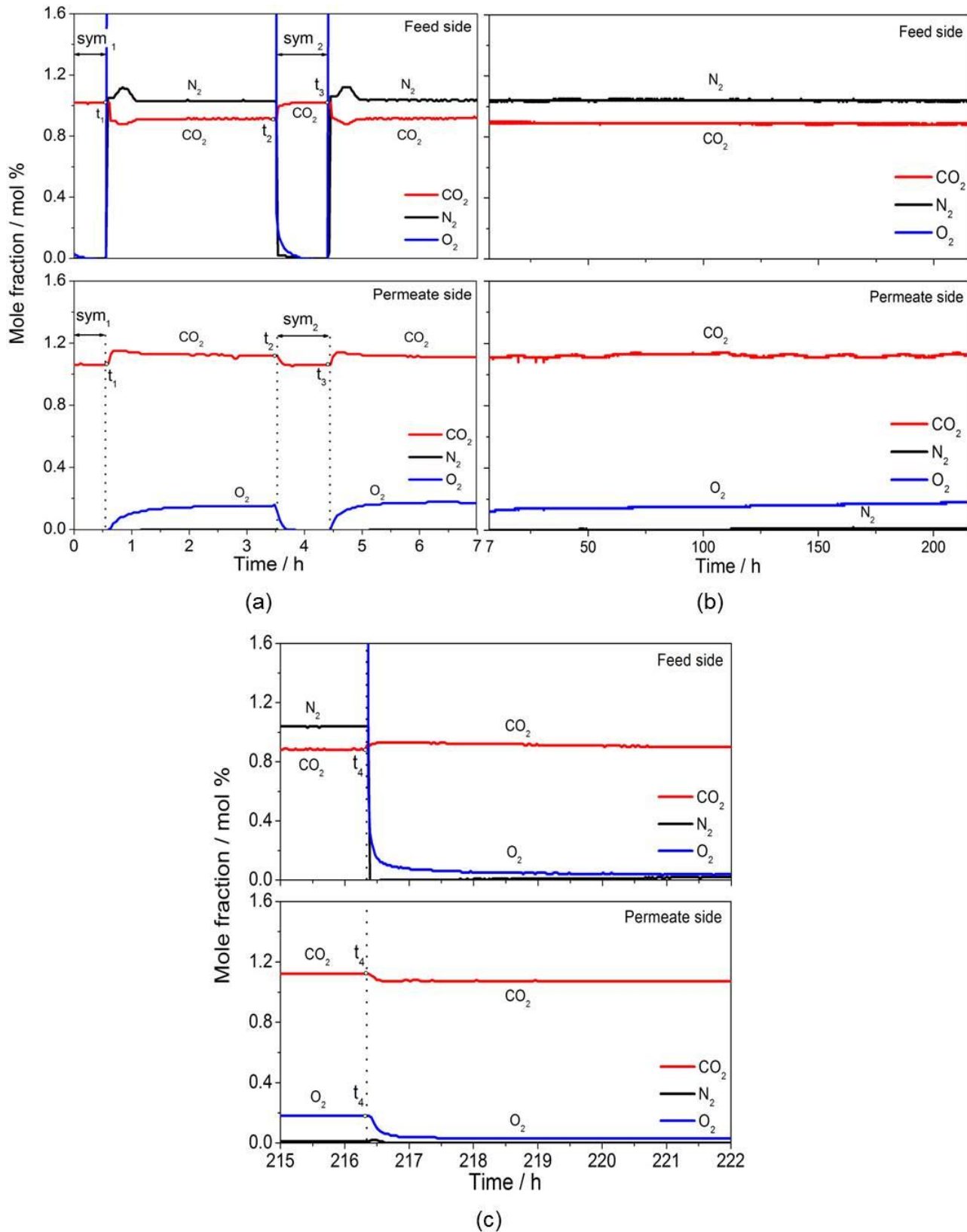


Figure 7.3 Mole fractions of gases in both feed-side and permeate-side outlets for experiment 2. (a) During asymmetrical operation: feed-side inlet: 0.99% CO₂/1.03% N₂/19.45% O₂ in Ar, permeate-side inlet: 1.03% CO₂ in Ar. During symmetrical operation: feed- and permeate-side inlets: 1.03% CO₂ in Ar. A flux of $1.8 \pm 0.3 \times 10^{-4}$ mol m⁻² s⁻¹ was determined at time t₃. (b) Uphill permeation performed over 216 hours (different timescale used) during asymmetrical operation with no apparent drop in flux or appearance of a trans-membrane leak and (c) return to symmetrical operation. (The

value for the oxygen mole fraction in the feed-side outlet during asymmetric operation is off scale).

Similar results could be obtained by repeating the experiment with a fresh membrane; experiment 2 continued to perform for 216 hours (Fig. 7.3(b)) without a decrease in flux. There was also no appearance of cross-chamber leakage between the feed and permeate sides, as indicated by the nitrogen indicator (1% N₂ in the feed side and no N₂ in the permeate side). A very slight variation in the CO₂ mole fraction in the permeate side could be seen (Fig. 7.3(b)) because of the temperature change in the laboratory. Fig. 7.3(c) shows that, at the time t_4 , the CO₂ mole fraction value reached 0.89% in the feed side and 1.12% in the permeate side, respectively. The CO₂ permeation rate after 216 hours of operation at t_4 was very similar to the result calculated and described before. At the time t_4 , the feed side had returned from C-1 to a symmetrical condition with cylinder C-2 and, after that, both the feed side and permeate side were fed with C-2. After the 216-hour CO₂ permeation, the molar amount of carbon that the membrane permeated was one order of magnitude greater than the molar carbonate held inside the membrane (the membrane contained 0.08 g of carbonate at an average molecular weight of 100 g mol⁻¹ or 8×10^{-4} moles of carbonate compared to a permeation rate of $\sim 10^{-8}$ mol s⁻¹ over 8×10^5 seconds or 8×10^{-3} moles of carbon dioxide).

Experiment 3: CO₂ up-hill permeation from about 0.5% to 1% at

600 °C

Experiment 3 was started under symmetrical conditions (sym₁) with the gas from cylinder C-2 (1.03% CO₂ in Ar) fed to both sides of the membrane (Fig. 7.4). At time t_1 , the feed-side inlet gas was switched to the mixture of C-1 (0.99% CO₂/1.03% N₂/19.45% O₂ in Ar) and C-3 (20% O₂ in Ar) in a molar ratio of 1:1, in such a way that the CO₂ mole fraction in the feed side became 0.51% (calibrated and checked prior to the experiment) and the oxygen mole fraction in the feed-side inlet was still 20%. The nitrogen was measured at 0.57% in the feed-side inlet to indicate any cross-chamber leakage of CO₂ in this experiment. About half an hour later, after switching the gas at t_1 , there was a large CO₂ permeation, which then declined, possibly because of the back diffusion of CO₂ from the permeate side to the feed side. At time t_2 , a symmetrical condition (sym₂) was applied again, both sides were fed with cylinder C-2, and there was no CO₂ permeation during this symmetrical period between t_2 and t_3 ; again at time t_3 , it switched to an asymmetrical condition to permeate CO₂ in a steady-state operation.

Chapter 7. Up-hill CO₂ permeation

The data from t_3 and t_4 were used to determine the CO₂ permeation rate. The permeate-side inlet gas was not changed during symmetrical or asymmetrical conditions; the CO₂ mole fraction difference between these two conditions gave a CO₂ flux of $1.5 \pm 0.3 \times 10^{-4}$ mol m⁻² s⁻¹ at time t_3 . It is clear that CO₂ permeated up-hill from around a 0.5% CO₂ environment to about a 1% CO₂ environment at 1 atmosphere of pressure. The CO₂ mole fraction in the feed-side outlet was 0.41% at t_4 , compared to 0.38% at the time around t_1 ; this indicates that the CO₂ permeation would have been much greater if there had been less CO₂ back diffusion through the membrane.

A further experiment, 3.1, was carried out to repeat CO₂ permeation from about a 0.5% mole fraction to approximately 1% without using a symmetrical condition; thus, there was no gas switching between the feed and permeate sides during the experiment. To show the CO₂ permeation clearly, an extra line was added to indicate the CO₂ mole fraction under non-permeation conditions at room temperature.

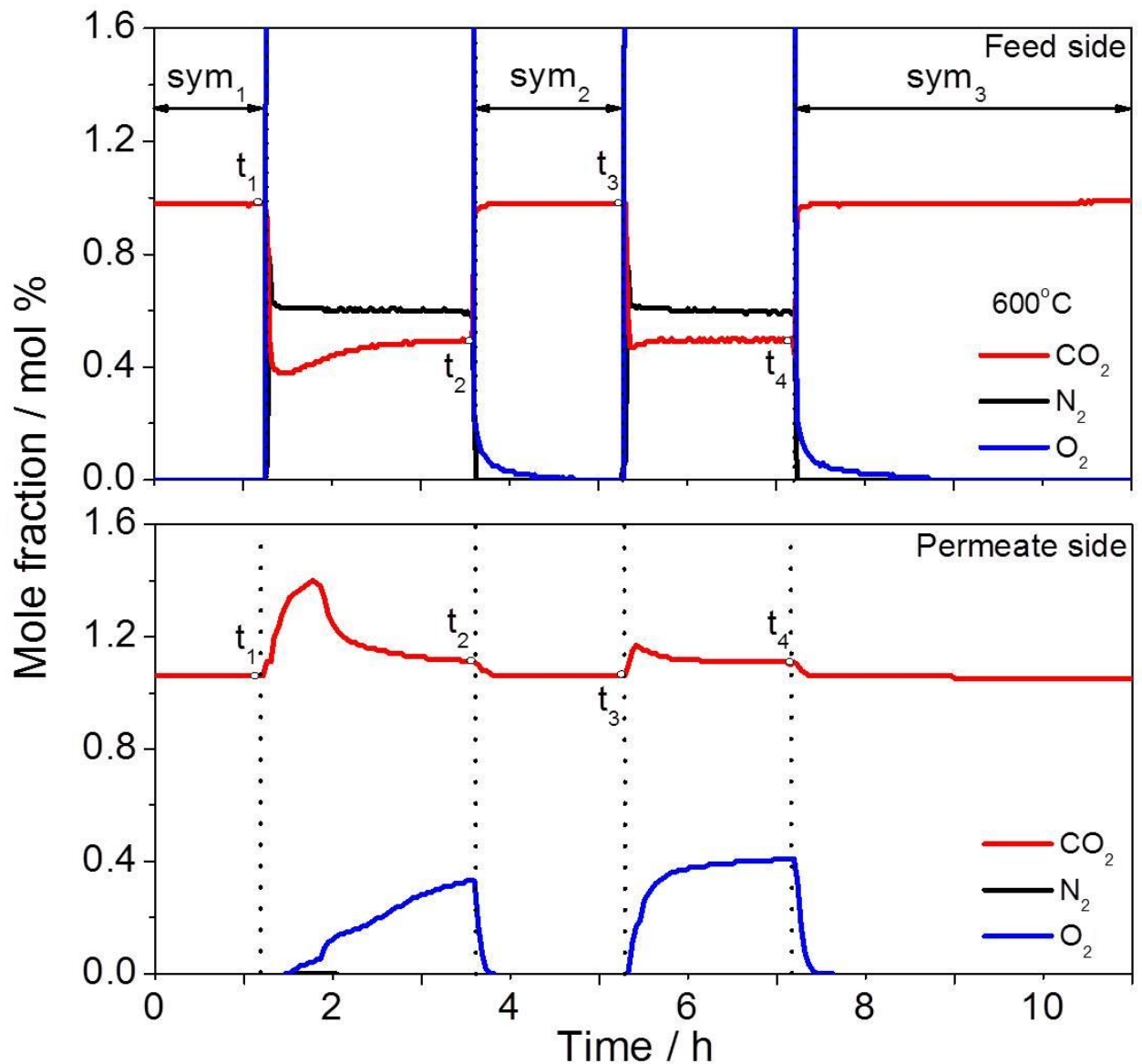


Figure 7.4 Mole fractions of gases in both feed- and permeate-side outlets for experiment 3. During symmetrical operation: feed- and permeate-side inlets: 1.03% CO₂ in Ar. During asymmetrical operation: feed-side inlet: 0.51% CO₂/0.57% N₂/19.5% O₂ in Ar, permeate-side inlet: 1.03% CO₂ in Ar. A flux of $1.5 \pm 0.3 \times 10^{-4} \text{ mol m}^{-2} \text{ s}^{-1}$ was determined at time t_4 . Note that the value for the oxygen mole fraction in the feed-side outlet during asymmetric operation is off scale.

Experiment 3.1: CO₂ up-hill permeation from 0.5% to 1% without symmetrical gas switching

Experiment 3.1 was started under the asymmetrical condition without any gas switching during the experiment; a mixture of C-1 (0.99% CO₂/1.03% N₂/19.45% O₂ in Ar) and C-3 (20% O₂ in Ar) in a molar ratio of 1:1 was fed to the feed side. The mole fraction of CO₂ in the feed side was 0.54%, and it was 1.04% in the permeate-side. It can be noted in Fig. 7.5 that the CO₂ permeation started in the feed side when the temperature was close to 600°C; as for experiment 3, which started with a symmetrical condition, the

Chapter 7. Up-hill CO₂ permeation

CO₂ mole fraction in the feed side decreased to a value below the non-permeation CO₂ mole fraction, which indicates that up-hill permeation had occurred. There is a line (Fig. 7.5) in both the feed side and the permeate side to indicate the CO₂ mol fraction under non-permeation conditions (0.54% in the feed side and 1.04% in the permeate side). The CO₂ permeation decreased to a steady state gradually after 8 hours (in the permeate side); the CO₂ permeation rate could be calculated at 10 hours and the value of flux was similar to that of experiment 3, which is about $1.5 \pm 0.3 \times 10^{-4} \text{ mol m}^{-2} \text{ s}^{-1}$. The CO₂ gas out from the membrane during heating for around 3.5 hours was about one-tenth of the infiltrated carbonate ($\sim 10^{-5}$) in molar percent. This experiment started with an asymmetrical condition but showed similar CO₂ permeation behaviour to that in experiment 3, with symmetrical conditions applied at the beginning.

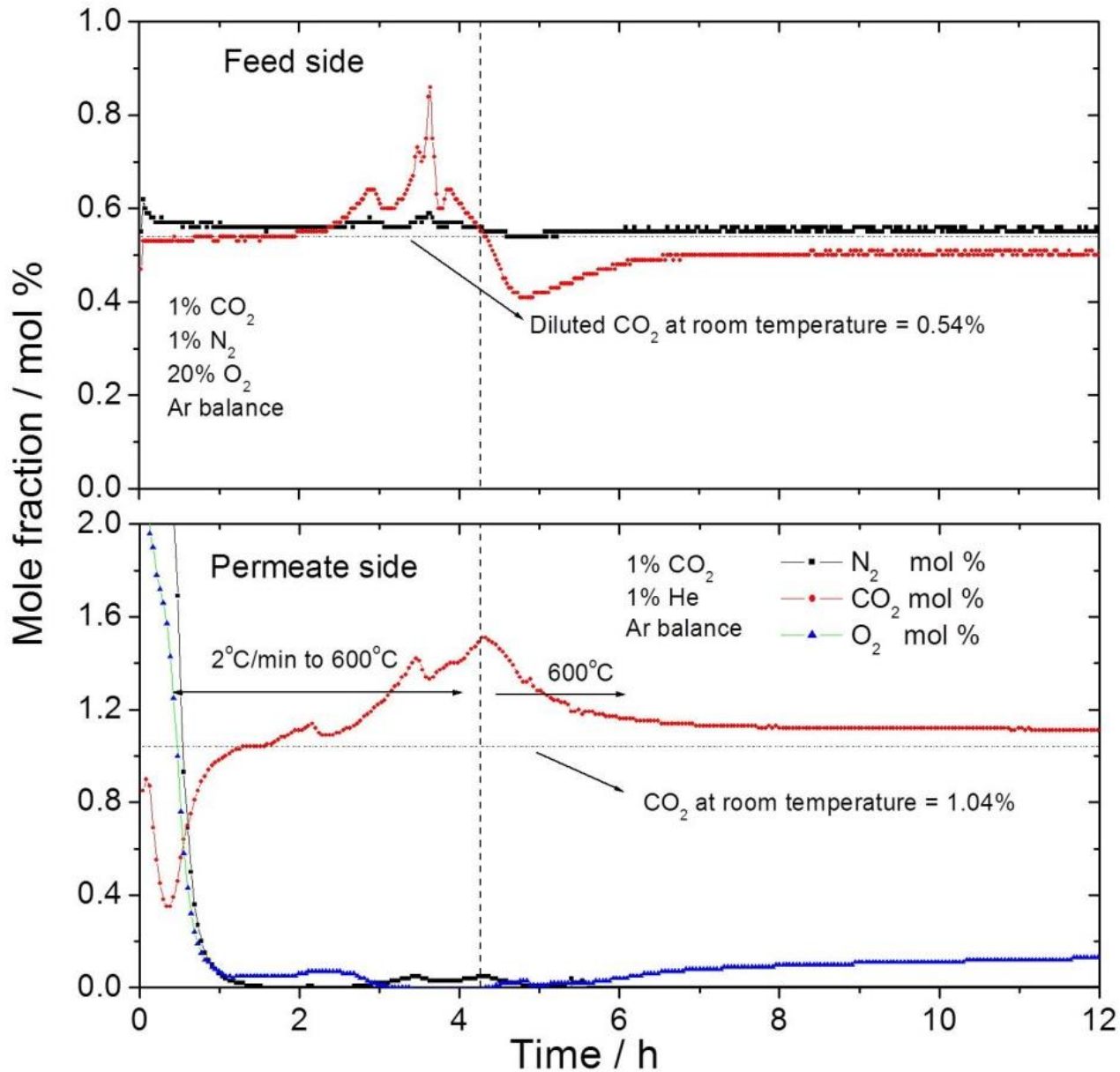


Figure 7.5 Mole fractions of gases in both feed- and permeate-side outlets for experiment 3.1. Feed-side inlet: 0.54% CO₂/0.56% N₂/19.5% O₂ in Ar, permeate-side inlet: 1.04% CO₂ in Ar. A flux of $1.4 \pm 0.3 \times 10^{-4} \text{ mol m}^{-2} \text{ s}^{-1}$ was determined after 10 hours.

Experiment 3.2L CO₂ permeation without O₂ in the feed side at 600 °C

To test whether carbon dioxide could permeate across the membrane by itself without gas phase oxygen at 600°C, experiment 3.2 was carried out and started with a symmetrical condition (sym₁ in Fig. 7.6) using gas cylinder C-2 (1.03% CO₂ in Ar) fed to both sides of the membrane. Following the CO₂ and O₂ mole fractions on both sides of the membrane during heating, the CO₂ evolution in the permeate side ceased when the temperature was around 600°C and appeared at a steady state before t_1 . At time t_1 , the permeate-side inlet was fed with a gas mixture of C-1 and C-4 in a molar ratio of

approximately 1:1, in such a way that the permeate-side inlet gas decreased from approximately 1% to about 0.6%. The CO₂ permeation was determined by the consumption of CO₂ in the feed side. CO₂ down-hill permeation appeared to occur during the time between t_1 and t_2 at the very limit of resolution, at a flux of $3 \times 10^{-5} \text{ mol m}^{-2} \text{ s}^{-1}$. The mole fraction of permeated CO₂ was about 0.01%, which is equal to the resolution of the mass spectrometer.

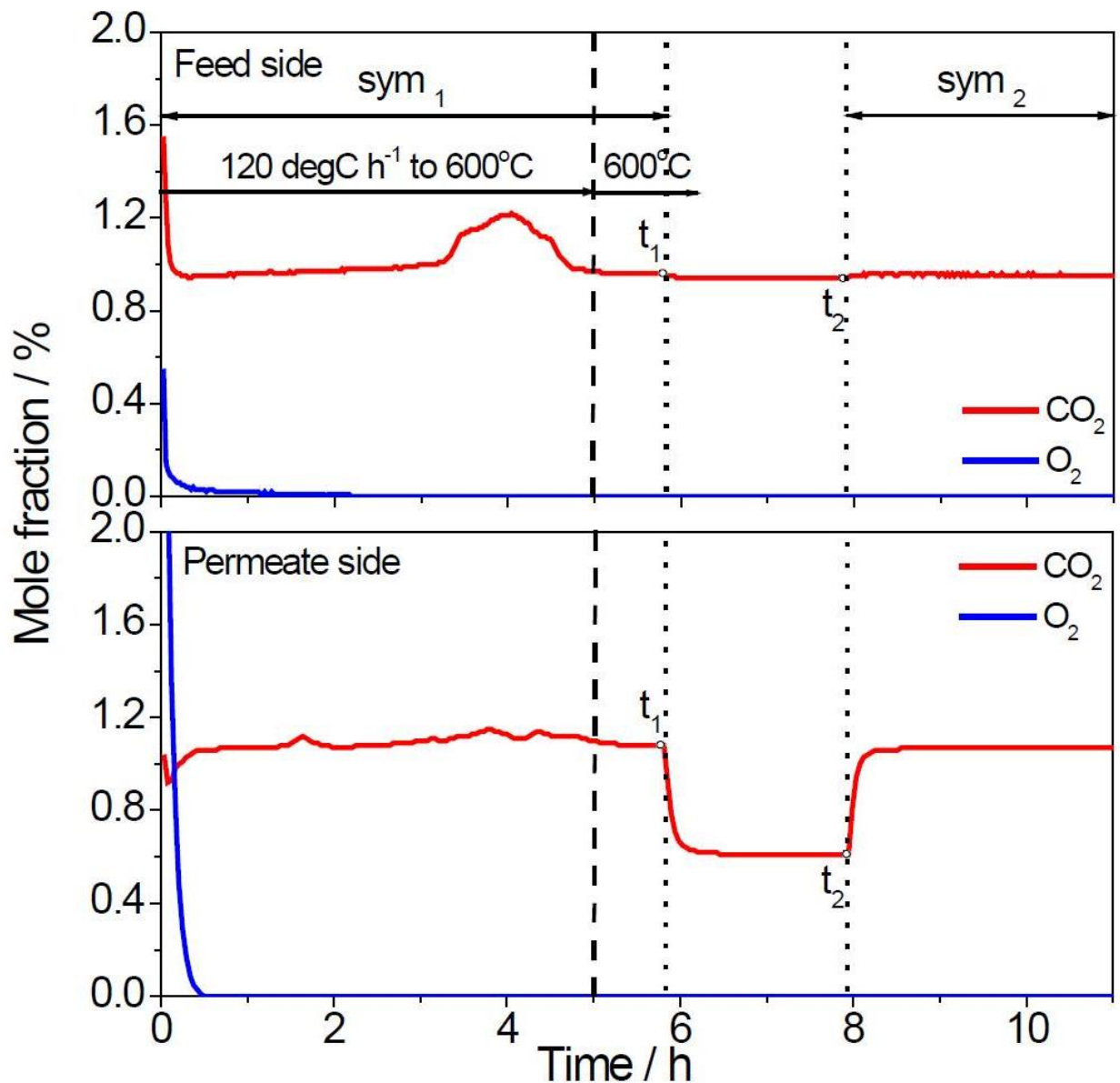


Figure 7.6 Mole fractions of gases in both feed- and permeate-side outlets for experiment 3.2. During symmetrical operation: feed- and permeate-side: 1.03% CO₂ in Ar. During asymmetrical operation: feed-side inlet: 1.03% CO₂ in Ar, permeate-side inlet: approximately 0.6% CO₂ in Ar

Experiment 3.3: O₂ permeation without CO₂ in the feed side at 600 °C

Experiment 3.3 was performed to test whether the oxygen could permeate across the membrane in the absence of CO₂. The membrane was heated under a symmetrical condition at the beginning ('sym' in Fig. 7.7) and fed with cylinder C-2 (1.03% CO₂ in Ar) on both sides of the membrane. After CO₂ degassing at about 5 hours during the heating, the CO₂ mole fraction became stable and the value reached 1.07% in the permeate-side outlet and 0.95% in the feed-side outlet. At time t_1 , the feed-side inlet gas was switched to cylinder C-3 (20% O₂ in Ar) and the inlet of the permeate side was switched to cylinder C-4 (pure Ar). After this, O₂ appeared in the feed-side outlet and there was no measurable O₂ in the permeate-side outlet. The CO₂ in the permeate-side outlet may have been due to the degassing of the molten carbonate in a pure argon atmosphere.

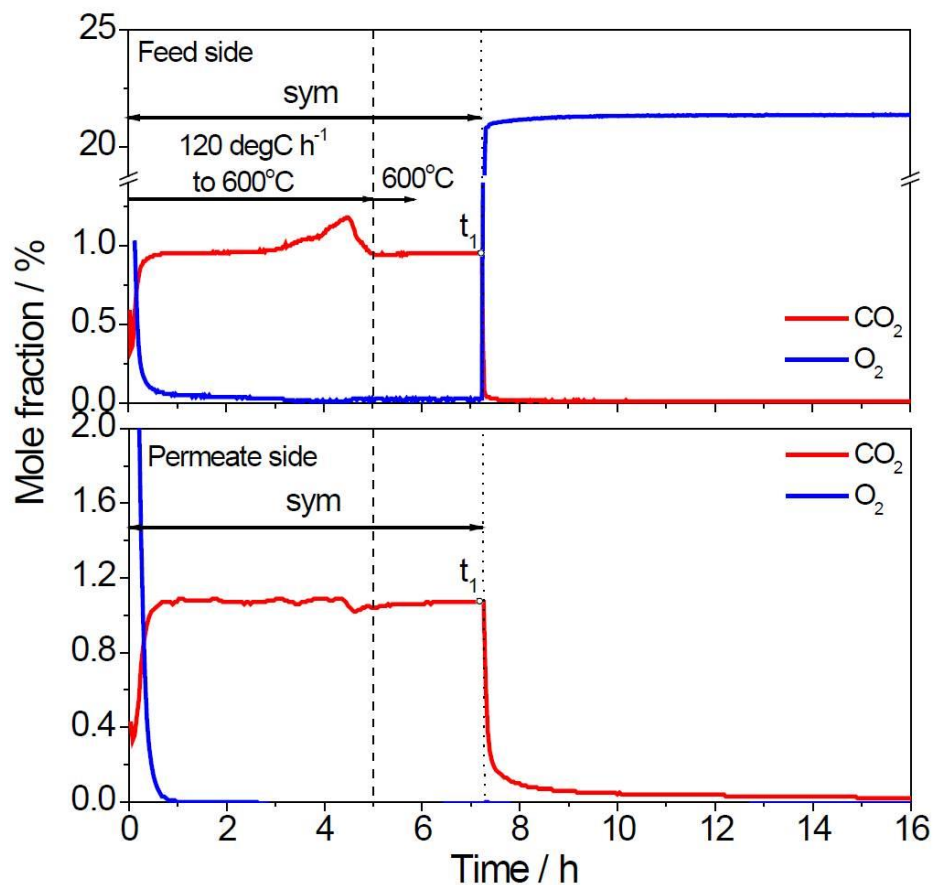


Figure 7.7 Mole fractions of gases in both feed- and permeate-side outlets for experiment 3.3. During symmetrical operation: feed- and permeate-side: 1.03% CO₂ in Ar. During asymmetrical operation: feed-side inlet: 20% O₂ in Ar, permeate-side inlet: pure Ar. There is a break in the scale of the y-axis for the feed-side graph.

7.3.2 Membrane characterisation

The morphology, microstructure, phase structure, and elemental analysis of the membrane were characterised by scanning electron microscope (SEM), energy dispersive x-ray spectroscopy (EDS) (Rontec Quantax 1.2 FEI XL30 ESEM-FEG), and X-ray diffraction (XRD) (PANalytical Empyrean Diffractometer operated in reflection mode, CuK α). It is important to note that these techniques were not employed in-situ and that the carbonate was in the solid state and no longer molten at the time of characterisation.

The LSCF6428 membranes were analysed by SEM micrographs, and the results showed the morphology of the external membrane surfaces before and after infiltration with molten carbonate; in particular, the membrane surface after permeation for 216 h was recorded. Note that only the feed-side images are shown here because there were no significant differences between feed-side and permeate-side SEMs. Figure 7.8(a) shows the membrane before infiltration. Figure 7.8(b) shows the membrane after infiltration without any permeation experiments started. Figure 7.8(c) shows the membrane after 216 h of continuous up-hill permeation (used membrane). EDS analysis (not shown) of the infiltrated membrane (fresh and used) indicated the presence of sodium and potassium over the entire surface of the membrane (lithium is too light to be detected). A discernible change was observed between the fresh membrane and the used membrane, which, after long-term operation, showed elongated carbonate crystals.

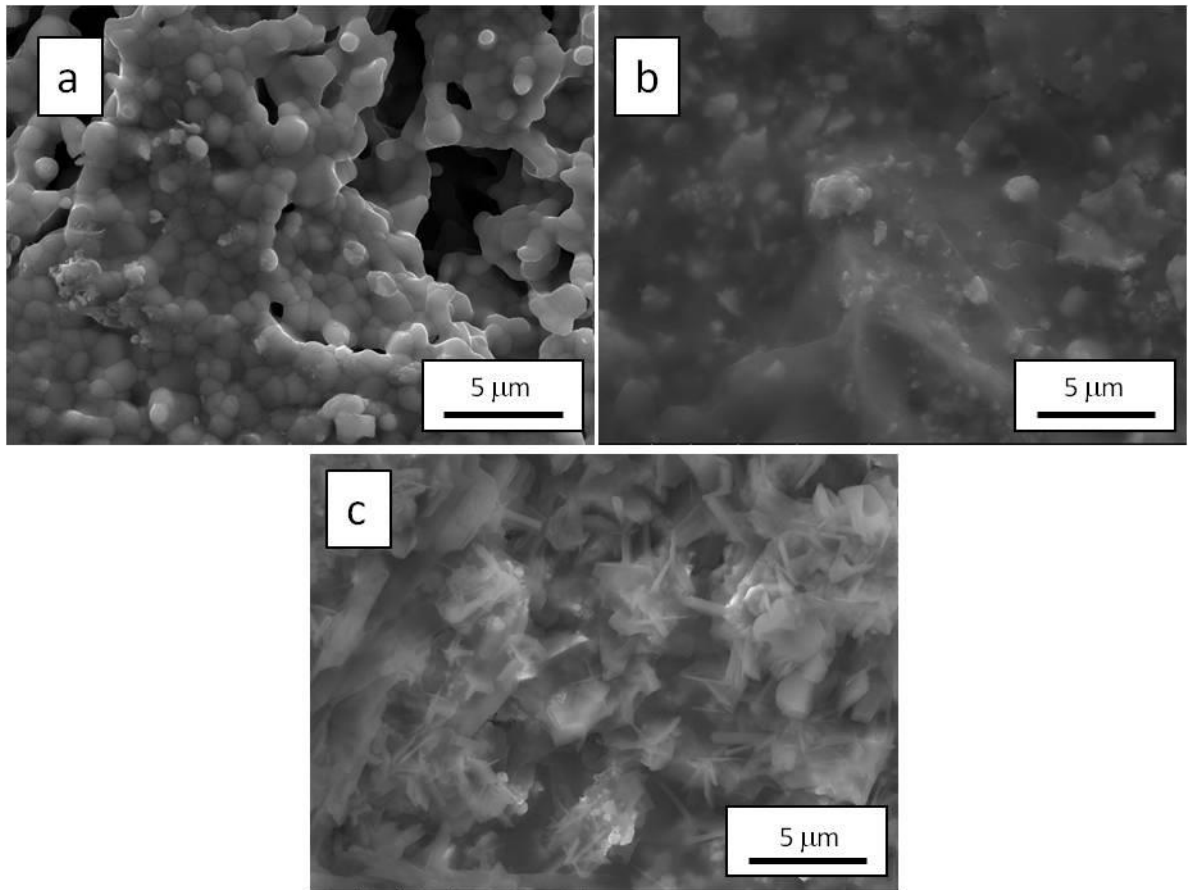


Figure 7.8 SEM micrographs of the external surfaces of an LSCF6428 membrane (a) before infiltration with molten carbonate; (b) after infiltration with molten carbonate; and (c) after permeation for 216 h

XRD diffractograms of the fresh and used membranes are shown in Figure 7.9. Data were acquired for 2θ values from 20° to 80° at a step size of 0.017° with a dwell time of 1 s. Both diffractograms show a fully developed perovskite-like structure and peaks indicative of molten carbonate at 2θ values of 29.4° and 37.3° . Note that the relative intensity of the molten carbonate peaks was quite low compared to the LSCF peaks and that carbonate peak intensity was decreased after permeation. Both of these findings were also reported in [25]. Some additional peaks may have been a result of the formation of interfacial species.

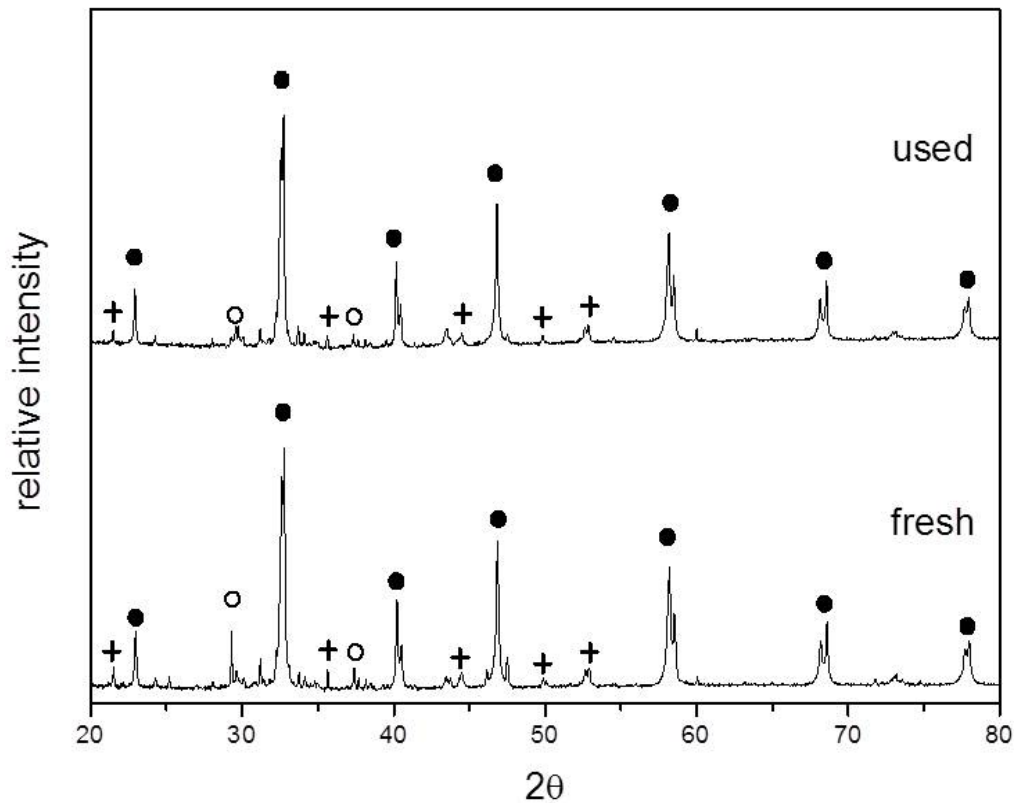


Figure 7.9 XRD diffractograms of the fresh and used membranes. Both diffractograms show a fully developed perovskite-like structure (indicated by ●) and peaks indicative of molten carbonate (indicated by ○). Some additional peaks may be due to the formation of interfacial species (indicated by +).

7.4 Conclusions

In this chapter, up-hill CO₂ permeation based on the dual-phase membrane system has been demonstrated successfully. The experiments have shown that CO₂ can permeate across the membrane system against its own chemical potential without energy penalty, which is important for an advanced CO₂ capture process. The driving force of this up-hill process is the oxygen partial pressure gradient; however, the extra oxygen more than the up-hill process requires found (a higher stoichiometric ratio of O₂/CO₂) in the permeate side. This limits the driving force for CO₂ permeation, and neither CO₂ nor O₂ alone can permeate at 600°C. The up-hill process partially depends on the electronic conductivity of the membrane support materials, and the carbonate diffusion is also a factor in this process.

A membrane permeance on the order of 10^{-6} mol m⁻² s⁻¹ Pa⁻¹ under asymmetric conditions (a permeability some four orders of magnitude greater than polymeric gas separation membranes of similar carbon dioxide/nitrogen separation factor) was

achieved at 600°C. Membrane performance was stable over more than 200 hours of operation. This value of permeability and the orders of magnitude for carbon dioxide separation are greater than those of other membrane technologies in this field at the moment (Fig. 7.10).

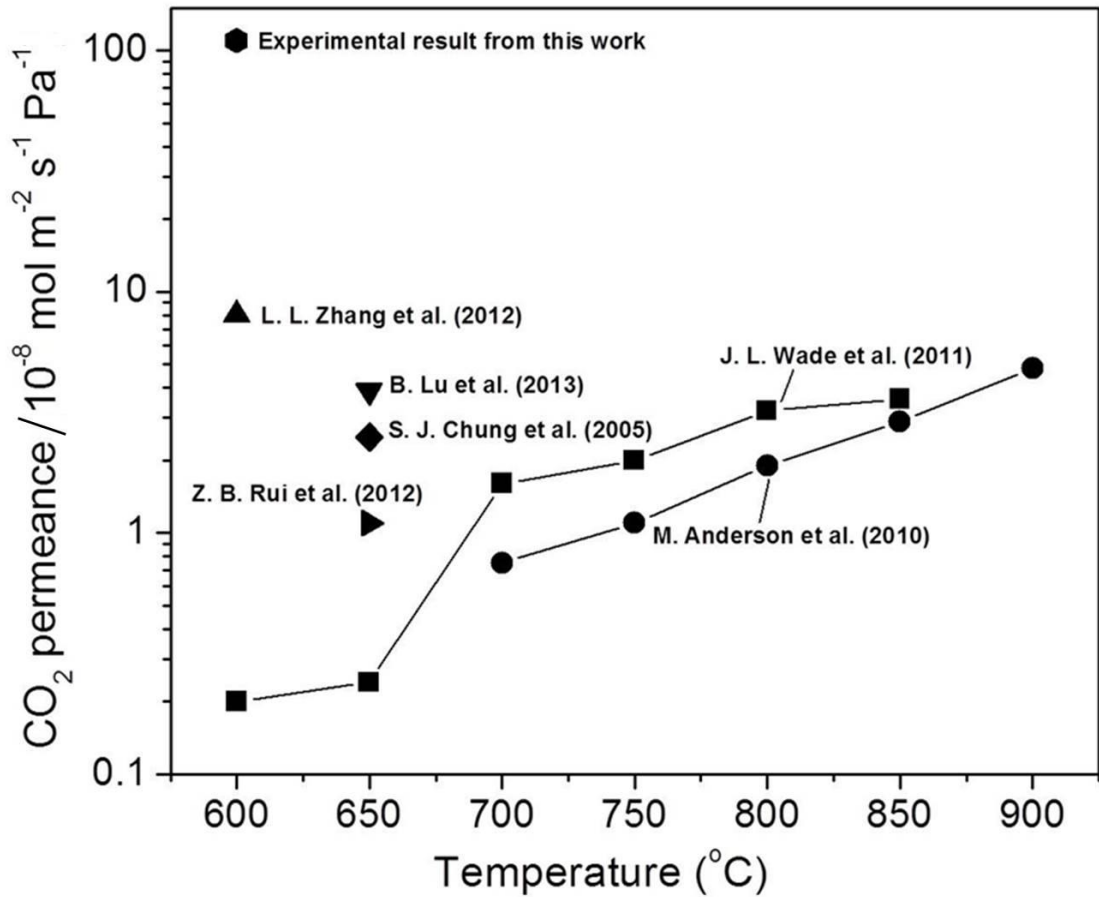


Figure 7.10 Carbon dioxide permeances as a function of temperature from references. Only the best-performing system is shown.

Chapter 8 Summary and future work

8.1 Conclusions and future work

8.1.1 Summary of the project

The current project studied the fabrication of LSCF-molten alkali metal carbonate dual-phase membranes and conducted CO₂ permeation experiments. Various pore formers were tested to create a porous structure inside membranes, and cornstarch was finally selected as the pore former material to fabricate the dual-phase membrane support. Another research group [25] made such a membrane using very similar material by partially sintering a fresh LSCF pellet. However, the porosity of such a membrane cannot be controlled and the mechanical stability of the partially sintered membrane is less than that of a fully sintered LSCF membrane using cornstarch as the pore former.

Sealing of the membrane at intermediate temperatures (500 to 700 °C) and high temperatures (>700 °C) were also discussed and a new reactor design was used to improve membrane sealing. Although some researchers [26] have studied dense membrane sealing methods and applied them to oxygen permeation membranes, very few works have discussed dual-phase membrane sealing for gas separation at high temperatures. The sealing method is critical for CO₂ permeation experiments, as leakage could cause permeation experiments to fail. The problem in sealing a dual-phase membrane is that the contact area between the membrane and support tube is unique; at room temperature, the membrane surface is solid, and the contact area with an alumina tube becomes a mixture of molten carbonates and solid LSCF at high temperatures above the melting point of carbonates, so the membrane sealing could easily fail during the change from the solid to molten phase. The different thermal expansion between the membrane material and the alumina tube support is another barrier to sealing the membrane because the membrane is sealed at room temperature and used at high temperatures. The current project spent more than a year to solve the problem until finally the CO₂ permeation experiments could be performed successfully; the leak rate for CO₂ permeation experiments at the beginning were more than 1% and finally dropped to less than 0.1%.

Chapter 8. Summary and future work

CO₂ and O₂ co-permeation experiments were performed; the results showed that 4% O₂ in the feed side can accelerate the CO₂ permeation significantly at 890°C. The CO₂ permeation rate as a function of O₂ and CO₂ partial pressure gradients between the two sides of the membrane were tested. Both CO₂ and O₂ partial pressure gradients affected the CO₂ permeation rate, which increased as the CO₂ or O₂ partial pressure gradient increased. It is important that the CO₂ permeation rate decreases when the O₂ partial pressure gradient decreases, even if the CO₂ partial pressure gradient increases significantly. It indicates that the O₂ partial pressure gradient has a greater driving force than the CO₂ partial pressure gradient. The limiting step for the CO₂ permeation process was also discussed, and the formation and transportation process of oxygen ions on lattice sites of the LSCF structure (O_O^X) (bulk diffusion) is considered the limiting step for CO₂ permeation at about 890°C. At a lower temperature of about 600°C, LSCF6428 is not an oxygen conductor (not activated under 650 °C). The LSCF dual-phase membrane can also be used as an electron-conducting material to co-permeate CO₂ and O₂, and this is the mechanism by which up-hill permeation can be achieved at 600°C.

Finally, CO₂ up-hill permeation was achieved at 600°C with permeability on the order of $10^{-6} \text{ mol m}^{-2} \text{ s}^{-1} \text{ Pa}^{-1}$ (oxygen ion conducting is not activated at this temperature), the membrane solid-phase LSCF performed as the electron conductor. The CO₂ permeance in the current project is greater than that of similar works in the literature, as show in Fig. 7.10. It is noted that Chung et al. [24] also used an electron-conducting material, stainless steel, as the membrane support to permeate CO₂, but Fe is significantly corrupted by molten carbonates, especially lithium carbonate. The concept of up-hill CO₂ permeation at 600°C is new, and the permeability and stability of the membrane can be improved in future work by further study and understanding of the CO₂ transport mechanism. The CO₂ up-hill permeation can be achieved also from a thermodynamic view; the total chemical potential of the feed-side μ' (molar Gibbs free energy) is greater than the chemical potential in the permeate-side φ'' . The process can shift from left to right, as Fig. 8.1 shows.

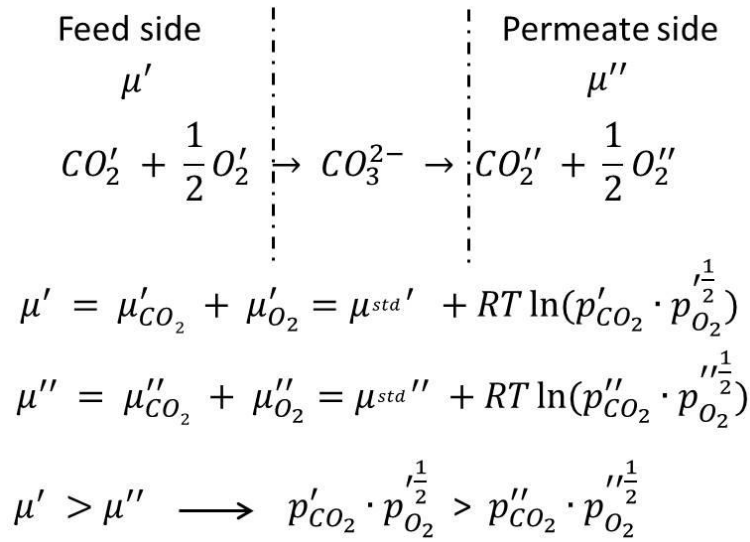


Figure 8.1 The driving force of up-hill CO₂ permeation, chemical potential gradient.

8.1.2 Achievement

In the current project, micro-porous structured La_{0.6}Sr_{0.4}Co_{0.2}Fe_{0.8}O₃ (LSCF6428)/La_{0.2}Sr_{0.8}Co_{0.8}Fe_{0.2}O₃ (LSCF2882) and yttria-stabilised zirconia (YSZ) membranes have been successfully sintered. The temperature ramping rate of 1 °C min⁻¹ from room temperature to 200 °C was found to combust pore formers and create uniform porosity in the membrane, but the sintering of such a porous membrane could fail if the ramping rate is more than 5 °C min⁻¹ or the temperature for combusting the pore former is more than 250 °C. The porous LSCF membrane substrate was successfully sintered at 1,200 °C following pore former combustion and it can work at the temperature up to 950 °C without cracking during heating, permeation, and cooling. Membranes made by this method were tested by SEM and used for CO₂ permeation experiments.

The sealing of the dual-phase membrane was improved significantly after applying pressure to membrane edge towards the support tube and using silver paste as the membrane sealant. It is important to dry the sealant carefully before starting the experiments. The experimental data showed that the silver sealant did not react with the dual-phase membrane because no silver is found inside the membrane and the other side of the membrane.

The CO₂ permeation experiments in Chapter 6 clearly showed that both O₂ and CO₂ partial pressure in the feed side of the membrane influenced the permeability of CO₂ and the mobile oxygen ions dominate the CO₂ permeation process, as it can drive the

CO₂ permeate across the membrane against the CO₂ partial pressure gradient. Lin [25, 27] also confirmed that the oxygen ion transportation is the limiting step for CO₂ permeation. The work in Chapter 6 found that the CO₂ permeation rate can still be maintained by decreasing the CO₂ partial pressure and increasing the O₂ partial pressure in the feed side.

The experimental data from up-hill CO₂ permeation at 600°C were presented in Chapter 7. The up-hill CO₂ permeation concept and the experiments were first described and presented in the CO₂ permeation ceramic membrane field with membrane permeance on the order of 10⁻⁶ mol m⁻² s⁻¹ Pa⁻¹ under asymmetric conditions.

8.13 Conclusions

The mobile oxygen transportation is considered the main driving force for CO₂ permeation in the LSCF-carbonate membrane, and it was investigated by kinetic experiments. The outcome showed that P(O₂) in the feed side accelerated CO₂ permeation significantly. The mechanism of O₂ and CO₂ co-permeation at 890°C was discussed in Chapter 6, and the outcomes of the experiments support the permeation model (Fig. 6.11).

At the temperature range of 700 to 900°C, the CO₂ reacts with oxygen ions (O²⁻) on LSCF lattice sites (structural oxygen) and form carbonate ions (CO₃²⁻) and oxygen vacancies. These oxygen vacancies become oxygen ions on the lattice again when the carbonate releases CO₂ in the permeate side. There are peroxide ions (O₂²⁻) in the carbonate melt (6 mol % at a temperature of 1,000K) [40], and the peroxide ions can also react with CO₂ to form CO₃²⁻ (there are no superoxide ions in eutectic because the Li contained in the melt). When P(O₂) is provided in the feed side, the O₂ can take the oxygen vacancies and become oxygen ions on the lattice, and this increases the number of oxygen ions in LSCF; the increasing of oxygen ions on the lattice accelerates the reaction between CO₂ and O²⁻.

The up-hill process can be achieved at 600°C because of the P(O₂) in the feed side and partially depends on the electronic conductivity of the membrane substrate materials; the carbonate diffusion is also a factor in this process. The conductivity is considered the limiting step for CO₂ and O₂ transportation at low temperatures (<650°C), and the CO₂ is difficult to permeate on its own without P(O₂) at temperatures under 650°C.

From the mechanism study, it can be concluded that a thin membrane can accelerate CO₂ permeation by shortening the carbonate diffusion path. A membrane support material with high electron conductivity can also increase the CO₂ permeation rate.

8.1.4 Future work

Future work on the dual-phase membrane separation technology will mainly focus on developing and manufacturing long tubular membrane modules and improving CO₂ permeability. The membrane thickness can be thinner than that of the current membrane pellet to increase permeation rate. However, the mechanical stability and thermal expansion of such a long tubular membrane needs to be considered because the system will work at high temperatures over 500°C, and this may cause the tube membrane to break during heating. The advantage of the tube membrane is that it can be cold sealed, and both the inlet and outlet of the tube membrane can be outside the furnace. The surface area of a tubular membrane is also much greater than that of a disk membrane; which can increase the gas permeation rate significantly.

In addition, a great deal of work will be required to examine the high-temperature stability of the membrane, especially in a long-term membrane system that can operate in an actual flue gas environment for several thousand to tens of thousands of hours. The long-term stability of membrane sealing is also important during the permeation process; however, very few studies have addressed the stability of sealing and leak development during permeation experiments. Most work will focus on permeability and membrane stability.

It is desirable to find cost-effective membrane materials to replace expensive LSCF or other rare earth materials. An idea is to use noble metal deposition technology to form a non-corrodible thin film on the surface of a porous membrane support such as porous alumina, and this can solve the corrosion problem of the stainless steel used by Chung [24]. To make the film continuous and not block the pores, it is necessary to immerse a porous alumina membrane in a 5% phosphoric acid solution for 10 to 30 minutes (depending on pore size) before deposition; this is an empirical method to expand the pore diameter slowly to prevent thick film from blocking the pores of the alumina membrane.

Chapter 8. Summary and future work

Moreover, molten salts other than carbonates can be infiltrated into a porous membrane and used for gas separation, such as molten nitrate for NO_x separation and molten sulphate for SO_x separation. For a wider application, non-corrosive materials need to be applied as the membrane substrate.

References

1. UN, *Kyoto protocol to the United Nations framework convention on climate change*. United Nations, 1998.
2. Lee, Z.H., et al., *Post-combustion carbon dioxide capture: Evolution towards utilization of nanomaterials*. Renewable and Sustainable Energy Reviews. **16**(5): p. 2599-2609.
3. Merkel, T.C., et al., *Power plant post-combustion carbon dioxide capture: An opportunity for membranes*. Journal of Membrane Science, 2009. **359**(1-2): p. 126-139.
4. EIA, U.S., *Emissions of greenhouse gases in the United States*. U.S. Energy Information Administration, 2009: p. 1-68.
5. C. Le Quéré, G.P.P., R. J. Andres, R. M. Andrew, et al, *Global Carbon Budget 2013*. Earth System Science Data, 2013. **Section 4. Discuss**: p. 256-258.
6. Thiruvenkatachari, R., et al., *Post combustion CO2 capture by carbon fibre monolithic adsorbents*. Progress in Energy and Combustion Science, 2009. **35**(5): p. 438-455.
7. Moriarty, P. and D. Honnery, *A human needs approach to reducing atmospheric carbon*. Energy Policy, 2009. **38**(2): p. 695-700.
8. Solomon DQ, M.M., *Climate change 2007*. Intergovernmental Panel on Climate Change (IPCC), 2007: p. 996.
9. Hansen J, S.M., Kharecha P, Beerling D, Berner R, Masson-Delmotte V, Pagani M, et al, *Target atmospheric CO2: where should humanity aim?* Open Atmosphere Science Journal, 2008. **2**(217): p. 31.
10. IPCC, *Climate Change 2007: Synthesis report*. Intergovernmental Panel on ClimateChange, 2007.
11. T.J, H., *Impact of electric power generation on green house gas emissions in Europe: Russia, Greece, Italy and views of the EU power plant supply industry* "A critical analysis". International Journal of Electrical Power & Energy Systems, 2006. **28**(8): p. 548-564.
12. Calin-Cristian, C., *Evaluation of power generation schemes based on hydrogen-fuelled combined cycle with carbon capture and storage (CCS)*. International Journal of Hydrogen energy, 2011. **36**(5): p. 3726-3738.
13. Elwell L C, G.W.S., *Technology options for capturing CO2-Special Reports*. Power, 2006. **150**: p. 8.
14. Figueroa, J.D., et al., *Advances in CO2 capture technology—The U.S. Department of Energy's Carbon Sequestration Program*. International Journal of Greenhouse Gas Control, 2008. **2**(1): p. 9-20.
15. Feron P H M, H.C.A., *CO2 capture process principles and costs*. Oil and Gas Science and Technology-Rev, 2006. **60**(3): p. 451-459.
16. Hongqun Yang, et al., *Progress in carbon dioxide separation and capture: A review*. Journal of Environmental Sciences, 2008. **20**(2008): p. 14-27.
17. Ryd'en M, L.A., *Using steam reforming to produce hydrogen with carbon dioxide capture by chemical-looping combustion*. International Journal of Hydrogen Energy, 2006. **31**: p. 1271-1283.
18. Bounaceur, R., et al., *Membrane processes for post-combustion carbon dioxide capture: A parametric study*. Energy, 2006. **31**(14): p. 2556-2570.
19. Eric, F., *Membrane processes and postcombustion carbon dioxide capture: Challenges and prospects*. Chemical Engineering Journal. **171**(3): p. 782-793.
20. Zebao Rui, H.J., Y.S. Lin, *Modeling and analysis of ceramiccarbonate dual-phase membrane reactor for carbon dioxide reforming with methane*. International Journal of Hydrogen Energy, 2011. **36**(2011): p. 8292-8300.

References

21. Kazuya Goto, Katsunori Yogo, and T. Higashii, *A review of efficiency penalty in a coal-fired power plant with post-combustion CO₂ capture*. Applied Energy, 2013. **111**: p. 710-720.
22. Kurt Zenz House, C.F.H., Michael J. Aziz, Daniel P. Schrag, *The energy penalty of post-combustion CO₂ capture & storage and its implications for retrofitting the U.S. installed base*. Energy & Environmental Science, 2009. **2**: p. 143-147.
23. Jennifer L. Wade, C.L., Alan C. West, Klaus S. Lackner, *Composite electrolyte membranes for high temperature CO₂ separation*. Journal of Membrane Science, 2011. **369**(2011): p. 20-29.
24. S. J. Chung, J.H.P., D. Li, J.-I. Ida, I. Kumakiri, and Jerry Y. S. Lin, *Dual-Phase Metal-Carbonate Membrane for High-Temperature Carbon Dioxide Separation*. Industrial & Engineering Chemistry Research, 2005. **44**(21): p. 7999-8006.
25. Matthew Anderson, Y.S.L., *Carbonate-ceramic dual-phase membrane for carbon dioxide separation*. Journal of Membrane Science, 2010. **357**(2010): p. 122-129.
26. Qi, X., F.T. Akin, and Y.S. Lin, *Ceramic - glass composite high temperature seals for dense ionic-conducting ceramic membranes*. Journal of Membrane Science, 2001. **193**(2): p. 185-193.
27. Zebao Rui, M.A., Y.S. Lin, Yongdan Li, *Modeling and analysis of carbon dioxide permeation through ceramic-carbonate dual-phase membranes*. Journal of Membrane Science, 2009. **345**(2009): p. 110-118.
28. M. Benamira, A.R., V. Albin, R.-N. Vannier, L. Hildebrandt, C. Lagergren, M. Cassir, *Gadolinia-doped ceria mixed with alkali carbonates for solid oxide fuel cell applications: I. A thermal, structural and morphological insight*. Journal of Power Sources, 2011. **196**(2011): p. 5546-5554.
29. Yongdan Li, Z.R., Chun Xia, Matthew Anderson, Y.S. Lin, *Performance of ionic-conducting ceramic/carbonate composite material as solid oxide fuel cell electrolyte and CO₂ permeation membrane*. Catalysis Today, 2009. **148**(2009): p. 303-309.
30. Chun Xia, Y.L., Ye Tian, Qinghua Liu, Yicheng Zhao, Lijun Jia, Yongdan Li, *A high performance composite ionic conducting electrolyte for intermediate temperature fuel cell and evidence for ternary ionic conduction*. Journal of Power Sources, 2009. **188**(2009): p. 156-162.
31. Takeo Yamaguchi, T.N., Balagopal N. Nair, Kazuaki Nakagawa, *Lithium silicate based membranes for high temperature CO₂ separation*. Journal of Membrane Science, 2007. **294**(2007): p. 16-21.
32. Wei Liu, Y.L., Bin Li, Taylor D. Sparks, Xi Wei, Wei Pan, *Ceria (Sm³⁺, Nd³⁺)/carbonates composite electrolytes with high electrical conductivity at low temperature*. Composites Science and Technology, 2010. **70**(2010): p. 181-185.
33. K. H. Stern, E.L.W., *High Temperature Properties and Decomposition of Inorganic Slats. Carbonates*, United States Department of Commerce, 1969. **Part 2**.
34. S.V. Devyatin, A.D.P., V.I. Shapoval, *Chemical and electrochemical behavior of carbonate melts containing silicon oxide*. Russian Journal of Applied Chemistry 2002. **75**(4): p. 562-564.
35. A.N. Timoshevskii, M.G.K., V.A. Emel'kin, B.A. Pozdnyakov, A.P. Zamyatin,, *High-temperature decomposition of lithium carbonate at atmospheric pressure*. High Temperature, 2008. **46**(3): p. 414-421.
36. R. Lehman, J.G., N. Glumac, *Thermal stability of potassium carbonate near its melting point*. Thermochemica Acta, 1998. **316**(1998): p. 1-9.
37. Sangcho Lee, M.K., Munkyeong Hwang, Kyubo Kim, Chunghwan Jeon, Juhun Song, *Thermal stability and viscosity behaviors of hot molten carbonate mixtures*. Experimental Thermal and Fluid Science 2013. **49**(2013): p. 94-104.
38. Rene I. Olivares, C.C., Steven Wright, *The Thermal Stability of Molten Lithium-Sodium-Potassium Carbonate and the Influence of Additives on the Melting Point*. Journal of Solar Energy Engineering, 2012. **134**.

References

39. Richard L. Lehmana, J.S.G., Nick G. Glumac, *Thermal stability of potassium carbonate near its melting point*. *Thermochimica Acta*, 1998. **316**(1998): p. 1-9.
40. Michel Cassir, G.M., Jacques Devynck, *Stability and Characterization of Oxygen Species in Alkali Molten Carbonate: A Thermodynamic and Electrochemical Approach*. *Journal of The Electrochemical Society*, 1993. **140**(11): p. 3114-3122.
41. A.J. Appleby, S.B.N., *Journal of The Electrochemical Society*, 1972. **53**(104).
42. Bhasker B. Dave, R.E.W., Supramaniam Srinivasan, A. John Appleby, *Impedance Analysis for Oxygen Reduction in a Lithium Carbonate Melt: Effects of Partial Pressure of Carbon Dioxide and Temperature* *Journal of The Electrochemical Society*, 1993. **140**(8): p. 2139-2145.
43. D. Chery, V.L., M. Cassir, *CO₂ electrochemical reduction into CO or C in molten carbonates: a thermodynamic point of view*. *Electrochimica Acta* 2015. **160**(2015): p. 74-81.
44. Haile, Z.S.S.M., *A high-performance cathode for the next generation of solid-oxide fuel cells*. *Nature*, 2004. **431**: p. 170-173.
45. Dusastre V, K.J., *Optimisation of composite cathodes for intermediate temperature SOFC applications*. *Solid State Ionics*, 1999. **126**: p. 163-174.
46. Serra JM, V.V., Buchler O, Meulenberg WA, Buchkremer HP, *IT-SOFC supported on mixed oxygen ionic–electronic conducting composites*. *Chemistry Materials*, 2008(20): p. 3867–3875.
47. Weishen Yang, H.W., Xuefeng Zhu, Liwu Lin, *Development and Application of Oxygen Permeable Membrane in Selective Oxidation of Light Alkanes*. *Topics in Catalysis*, 2005. **35**(1): p. 155-167.
48. Hatim, M.D.I., et al., *Catalytic Dehydrogenation of Methylcyclohexane (MCH) to Toluene in a Palladium/Alumina Hollow Fibre Membrane Reactor*. *Procedia Engineering*, 2012. **53**(0): p. 71-80.
49. Akin FT, L.Y., *Oxidative Coupling of Methane in Dense Ceramic Membrane Reactor with High Yields*. *AIChE Journal*, 2002. **48**: p. 2298–2306.
50. Teraoka Y, Z.H., Furuka S, Yamazoe N, *Oxygen permeation through perovskite-type oxides*. *Chemistry Letters*, 1985. **11**: p. 1743–1746.
51. Kharton VV, N.E., Nikolaev AV, *Materials of high-temperature electrochemical oxygen membranes*. *Journal of Membrane Science*, 1996. **111**: p. 149–157.
52. Sunarso, J., et al., *Mixed ionic - electronic conducting (MIEC) ceramic-based membranes for oxygen separation*. *Journal of Membrane Science*, 2008. **320**: p. 13-41.
53. Priscila Lemes-Rachadel, et al., *Current developments of mixed conducting membranes on porous substrates*. *Materials Research*, 2014. **17**(1): p. 242-249.
54. Sunarso J, B.S., Serra JM, MeulenbergWA, Liu S, Lin YS, Dinizda Costa JC, *Mixed ionic–electronic conducting (MIEC) ceramic-based membranes for oxygen separation*. *J Membr Sci*, 2008. **320**: p. 13-41.
55. Xuefeng Zhu, et al., *Permeation Model and Experimental Investigation of Mixed Conducting Membranes*. *AIChE Journal*, 2012. **58**(6): p. 1744-1754.
56. Badwal SPS and C. FT, *Ceramic membrane technologies for oxygen separation*. *Advanced Materials*, 2001. **13**(12-13): p. 993-996.
57. Burggraaf AJ and C. L, *Fundamentals of Inorganic Membrane Science and Technology*. New York: Elsevier, 1996.
58. VM, G., *Geochemische Verteilungsgesetze der Elemente*. Oslo: Norske Videnska, 1927.
59. Arumugam Manthiram, et al., *Crystal chemistry and properties of mixed ionic-electronic conductors*. *Journal of Electroceramics* 2011. **27**: p. 93-107.
60. Adler, S.B., X.Y. Chen, and J.R. Wilson, *Mechanisms and rate laws for oxygen exchange on mixed-conducting oxide surfaces*. *Journal of Catalysis*, 2007. **245**(1): p. 91-109.
61. Hashim, S.M., A.R. Mohamed, and S. Bhatia, *Current status of ceramic-based membranes for oxygen separation from air*. *Advances in Colloid and Interface Science*, 2010. **160**(1&2): p. 88-100.

References

62. Wang, H., Y. Cong, and W. Yang, *Oxygen permeation study in a tubular Ba_{0.5}Sr_{0.5}Co_{0.8}Fe_{0.2}O_{3- δ} oxygen permeable membrane*. Journal of Membrane Science, 2002. **210**(2): p. 259-271.
63. Lane, J.A. and J.A. Kilner, *Oxygen surface exchange on gadolinia doped ceria*. Solid State Ionics, 2000. **136-137**(0): p. 927-932.
64. Ruiz-Trejo, E., et al., *Oxygen ion diffusivity, surface exchange and ionic conductivity in single crystal Gadolinia doped Ceria*. Solid State Ionics, 1998. **113**: p. 565-569.
65. Lin, Y., *Microporous and dense inorganic membranes: current status and prospective*. Separation and Purification Technology 2001. **25**: p. 39-55.
66. Zeng Y, L.Y., Swartz SL, *Perovskite type ceramic membranes: synthesis, oxygen permeation and membrane reactor performance for oxidative coupling of methane*. Journal of Membrane Science 1998. **150**: p. 87-98.
67. Balachandran U, K.M., Kobylinski TP, Morissette SL, Pei S, *Oxygen ionconducting dense ceramic membranes*. Assigned to Amoco Co. US Patent 5,639,437, 1997.
68. Schwartz M, W.J., Sammels AF, *Solid state oxygen anion and electronmediating membrane and catalytic membrane reactors containing them*. Assigned to Eltron Research, Inc., US Patent, 6,033,632;, 2000.
69. Chen CC, P.R., Gottzmann CF, *Solid electrolyte membrane with porous catalytically-enhancing constituents*. Assigned to Praxair Technology, US Patent 5,938,822;, 1999.
70. Lin, J.K.a.Y.S., *Synthesis and Oxygen-Permeation Properties of Thin YSZ/Pd Composite Membranes*. AIChE Journal, 2000. **46**(8): p. 1521-1529.
71. M.A. Habib, R.B.M., M.A. Nemit-allah, *Modeling of oxygen permeation through a LSCF ion transport membrane*. Computers & Fluids, 2013. **76**(1-10).
72. Atsushi Mineshige, J.I., Maiko Nakamura, Kengo Nigaki, Jiro Abe, Masafumi Kobune, Satoshi Fujii, Tetsuo Yazawa, *Introduction of A-site deficiency into La_{0.6}Sr_{0.4}Co_{0.2}Fe_{0.8}O_{3- δ} and its effect on structure and conductivity*. Solid State Ionics, 2005. **176**(2005): p. 1145-1149.
73. L.-W. Tai, M.M.N., H.U. Anderson, D.M. Sparlin, S.R. Sehlin, *Structure and electrical properties of La_{1-x}Sr_xCo_{1-y}Fe_yO₃. Part 2. The system La_{1-x}Sr_xCo_{0.2}Fe_{0.8}O₃*. Solid State Ionics, 1995. **76**(1995): p. 273-283.
74. L.-W. Tai, M.M.N., H.U. Anderson, D.M. Sparlin, S.R. Sehlin, *Structure and electrical properties of La_{1-x}Sr_xCo_{1-y}Fe_yO₃. Part 1. The system La_{0.2}Sr_{0.8}Co_{1-y}Fe_yO₃*. Solid State Ionics, 1995. **76**(1995): p. 259-271.
75. L-W. Tai, M.M.N., and H. U. Anderson, *Thermochemical stability, Electrical Conductivity, and Seebeck Coefficient of Sr-Doped LaCo_{0.2}Fe_{0.8}O_{3- δ}* . Journal of Solid State Chemistry, 1995. **118**(1995): p. 117-124.
76. Y. Teraoka, H.M.Z., K. Okamoto, N. Yamazoe, *Mixed Ionic-Electronic Conductivity of La_{1-x}Sr_xCo_{1-y}Fe_yO_{3- δ} Perovskite-Type Oxides*. Materials Research Bulletin, 1988. **23**(1): p. 51-58.
77. Mingyi, L., et al., *Influence of pore formers on physical properties and microstructures of supporting cathodes of solid oxide electrolysis cells*. International Journal of Hydrogen energy, 2010. **35**(7): p. 2670-2674.
78. Sadao Araki, Y.H., Satoshi Hamakawa, Susumu Hikazudani, Fujio Mizukami, *Synthesis and characterization of mixed ionic–electronic conducting Ca_{0.8}Sr_{0.2}Ti_{0.7}Fe_{0.3}O_{3- α} thin film*. Solid State Ionics, 2008. **178**(2008): p. 1740-1745.
79. Grégory Etchegoyen, T.C., Pascal Del-Gallo, *An architectural approach to the oxygen permeability of a La_{0.6}Sr_{0.4}Fe_{0.9}Ga_{0.1}O_{3- δ} perovskite membrane*. Journal of the European Ceramic Society, 2006. **26**(2006): p. 2807-2815.
80. Grégory Etchegoyen, T.C., Aurélie Julian, Pascal Del-Gallo, *Microstructure and oxygen permeability of a La_{0.6}Sr_{0.4}Fe_{0.9}Ga_{0.1}O_{3- δ} membrane containing magnesia as dispersed second phase particles*. Journal of Membrane Science, 2006. **268**(2006): p. 86-95.

References

81. Isobe, T., et al., *Gas permeability and mechanical properties of porous alumina ceramics with unidirectionally aligned pores*. Journal of the European Ceramic Society, 2007. **27**(1): p. 53-59.
82. Franciscus, M., *Method of connecting ceramic material to another material*. US Patent 5,139,191, 1992.
83. O.C. Paiva, M.A.B., *Production, bond strength and electrochemical behavior of commercially pure Ti/Al₂O₃ brazed joints*. Journal of Materials Science 1992. **32**: p. 653.
84. Y. Teraoka, H.M.Z., S. Furukawa, N. Yamazoe, *Oxygen permeation through perovskite-type oxides*. Chemistry Letters 1985: p. 1743.
85. S. Carter, A.S., R.J. Chater, J. Kajda, J.A. Kilner, B.C.H. Steele, *Oxygen transport in selected non-stoichiometric perovskite-structure oxides*. Solid State Ionics. **597**(1992): p. 53-56.
86. Y. Zeng, Y.S.L., S.L. Swartz, *Perovskite-type ceramic membranes: synthesis, oxygen permeation and membrane reactor performance for oxidative coupling of methane*. Journal of Membrane Science **150**(1998): p. 87.
87. L. Qiu, T.H.L., L.M. Liu, Y.L. Yang, A.J. Jacobson, *Oxygen permeation studies of SrCo_{0.8}Fe_{0.2}O_{3-δ}*,. Solid State Ionics. **76**(1995): p. 321.
88. M.F. Carolan, P.N.D., *Ion transport membranes with catalyzed dense layer*. US Patent 5,569,633, 1996.
89. S.J. Xu, W.J.T., *Perovskite-type oxide membranes for the oxidative coupling of methane*. AIChE Journal **43 (11A)**(1997): p. 2731.
90. J.A. Lane, S.J.B., D. Waller, J.A. Kilner, *Oxygen transport in La_{0.6}Sr_{0.4}Co_{0.2}Fe_{0.8}O_{3-δ}*,. Solid State Ionics. **121**(1999): p. 201.
91. F.J. Klug, S.V., K.W. Lay, *Alumina, calcia, yttria sealing composition*. US Patent 5,321,335, 1992.
92. S. Hamakawa, T.H., H. Iwahara, *Electrochemical methane coupling using protonic conductors*. Journal of The Electrochemical Society. **14**(1993): p. 459.
93. Tyler T. Norton, J.O.-L.a.Y.S.L., *Stability of La-Sr-Co-Fe Oxide-Carbonate Dual-Phase Membranes for Carbon Dioxide Separation at High Temperatures*. Industrial & Engineering Chemistry Research, 2014. **53**(2014): p. 2432-2440.
94. Cari S. Dutcher, A.S.W.a.S.L.C., *Surface Tensions of Inorganic Multicomponent Aqueous Electrolyte Solutions and Melts*. J. Phys. Chem. A, 2010. **2010**(114): p. 12216–12230.
95. Xiancai.Fu, W.S., Tianyang.Yao, Wenhua.Hou, *Physical Chemistry (5th Edn)*. Higher Education Press (HEP), China, 2006: p. 319.
96. Lundblad, A. and B. Bergman, *Determination of Contact Angle in Porous Molten-Carbonate Fuel-Cell Electrodes*. Journal of The Electrochemical Society, 1997. **144**(3): p. 984-987.
97. Y. Teraoka, H.M.Z., K. Okamoto, N. Yamazoe, *MIXED IONIC-ELECTRONIC CONDUCTIVITY OF La_{1-x}Sr_xCo_{1-y}Fe_yO₃₋₆ PEROVSKITE-TYPE OXIDES*. Materials Research Bulletin, 1988. **23**(1): p. 55-58.
98. Daniel Peeters, Dominique Moyaux, and P. Claes, *Solubility and Solvation of Carbon Dioxide in the Molten Li₂CO₃/Na₂CO₃/K₂CO₃ (43.5:31.5:25.0 mol-%) Eutectic Mixture at 973 K*. European Journal of Inorganic Chemistry, 1999. **1999**(4): p. 589-592.

Appendix A

Calculation of flux, permeance, and permeability

The membrane permeation area is $0.5 \text{ cm}^2 = 5 \times 10^{-5} \text{ m}^2$;

Gas flow rate to both feed and permeate-side is 20 ml min^{-1} ;

Mole percent is used for each component: mol%

Permeation **flux** (in Jerry Lin's paper [93]): $\text{ml min}^{-1} \text{ cm}^{-2}$

$$\text{Flux} = \frac{\text{mol}\% \times 20 \text{ ml/min}}{100} \times \frac{1}{0.5 \text{ cm}^2}$$

Permeance: $\text{mol m}^{-2} \text{ s}^{-1} \text{ Pa}^{-1}$

$$\begin{aligned} \text{Permeance} &= \frac{\text{mol}\% \times 20 \text{ ml/min}}{100 \times 22400 \text{ ml/mol}} \times \frac{1}{0.5 \times 10^{-4} \text{ m}^2} \times \frac{1}{60 \text{ s/min}} \\ &\times \frac{1}{Pa' (CO_2) - Pa' (CO_2)} \end{aligned}$$

Permeability: $\text{mol m}^{-1} \text{ s}^{-1} \text{ Pa}^{-1}$

$$\text{Permeability} = \text{Permeance} \times \text{thickness of membrane (m)}$$

Permeation **rate:** mol s^{-1}

$$\text{Permeation rate} = \frac{\text{mol}\% \times 20 \text{ ml/min}}{100} \times \frac{1}{22400 \text{ ml/mol}} \times \frac{1}{60 \text{ s/min}}$$

Example:

50% CO₂ in the feed side and 1% CO₂ in the permeate side;

Membrane thickness is 1 mm = 10^{-3} m.

$$\text{Flux in permeate side} = \frac{1 \times 20 \text{ ml/min}}{100} \times \frac{1}{0.5 \text{ cm}^2} = 0.4 \text{ ml min}^{-1} \text{ cm}^{-2}$$

Appendix A

$$\begin{aligned} \text{Permeance} &= \frac{1 \times 20 \text{ ml/min}}{100 \times 22400 \text{ ml/mol}} \times \frac{1}{0.5 \times 10^{-4} \text{ m}^2} \times \frac{1}{60 \text{ s/min}} \\ &\times \frac{1}{101000 \times (0.5 - 0.01)} = 6 \times 10^{-8} \text{ mol m}^{-2} \text{ s}^{-1} \text{ Pa}^{-1} \end{aligned}$$

$$\text{Permeability} = 6 \times 10^{-8} \times 1 \times 10^{-3} = 3 \times 10^{-11} \text{ mol m}^{-1} \text{ s}^{-1} \text{ Pa}^{-1}$$

$$\begin{aligned} \text{Permeation rate} &= \frac{1\% \times 20 \text{ ml/min}}{100} \times \frac{1}{22400 \text{ ml/mol}} \times \frac{1}{60 \text{ s/min}} \\ &= 1.49 \times 10^{-7} \text{ mol s}^{-1} \end{aligned}$$

Appendix B

Thermodynamic calculation for thermal stability of ternary carbonate eutectic mixture

The relationship between Gibbs free energy and temperature can be expressed by the Gibbs-Helmholtz equation:

$$\left[\frac{\partial(\frac{\Delta G}{T})}{\partial T}\right]_p = -\frac{\Delta H}{T^2} \quad (1)$$

$$\text{Or } \int d\left(\frac{\Delta G}{T}\right)_p = \int -\frac{\Delta H}{T^2} dT \quad (2)$$

After indefinite integration of equation 2, it can be expressed as follows:

$$\frac{\Delta G}{T} = -\int \frac{\Delta H}{T^2} dT + I \quad (3)$$

where I is the integration constant.

To obtain the $\Delta_r G_m(T_2)$ at temperature T_2 , $\Delta_r G_m(T_1)$ at T_1 needs to be calculated from the relationship between ΔH and temperature.

First, C_p can be expressed as a function of temperature:

$$C_p = a + bT + cT^2 + dT^3 + eT^{-2} \quad (4)$$

The differential heat capacity at constant pressure between products and reactants can be expressed as follows:

$$\Delta C_p = \Delta a + \Delta bT + \Delta cT^2 + \Delta dT^3 + \Delta eT^{-2} \quad (5)$$

Therefore,

$$\begin{aligned} \Delta H &= \int \Delta C_p dT + \Delta H_0 = \int (\Delta a + \Delta bT + \Delta cT^2 + \Delta dT^3 + \Delta eT^{-2}) dT + \Delta H_0 = \\ &\Delta H_0 + \Delta aT + \frac{1}{2}\Delta bT^2 + \frac{1}{3}\Delta cT^3 + \frac{1}{4}\Delta dT^4 - \Delta eT^{-1} \end{aligned} \quad (6)$$

where ΔH_0 is the integration constant.

Appendix B

From equation 6, ΔH can be obtained and substituted in the Gibbs-Helmholtz equation 1:

$$\left[\frac{\partial(\frac{\Delta G}{T})}{\partial T}\right]_p = -\frac{\Delta H}{T^2} = -\frac{(\Delta H_0 + \Delta aT + \frac{1}{2}\Delta bT^2 + \frac{1}{3}\Delta cT^3 + \frac{1}{4}\Delta dT^4 - \Delta eT^{-1})}{T^2};$$

after integration, it can be expressed as follows:

$$\frac{\Delta G}{T} = \frac{\Delta H_0}{T} - \Delta a \ln T - \frac{1}{2}\Delta bT - \frac{1}{6}\Delta cT^2 - \frac{1}{12}\Delta dT^3 + \frac{1}{2}\Delta e \frac{1}{T^2} + I \quad (7)$$

It can also expressed as follows:

$$\Delta G = \Delta H_0 - \Delta aT \ln T - \frac{1}{2}\Delta bT^2 - \frac{1}{6}\Delta cT^3 - \frac{1}{12}\Delta dT^4 + \frac{1}{2}\Delta e \frac{1}{T} + IT \quad (8)$$

For a reaction $M_2CO_3 \leftrightarrow M_2O + CO_2 \uparrow$ where M represents the alkali metal Li/Na/K, the standard Gibbs free energy ΔG^\ominus of the reaction at temperatures other than 298 K can be expressed as follows:

$$\Delta G^\ominus_T = \Delta G^\ominus_{298} + \Delta G_{T'} = \Delta G^\ominus_{298} + \int_{298}^T \Delta C_p dT' - T \int_{298}^T \frac{\Delta C_p}{T'} dT' \quad (9)$$

Therefore, the Gibbs free energy for the reaction can be obtained from the standard Gibbs free energy:

$$\Delta_r G_T = \Delta G_T^\ominus + RT \ln K \quad (10)$$

where K is the CO₂ partial pressure.

Set $\Delta_r G_T = 0$, the equilibrium CO₂ partial pressure of the reaction can be calculated from equation 10:

$$\ln K = \frac{\Delta G_T^\ominus}{-RT} = \frac{\Delta H_0 - \Delta aT \ln T - \frac{1}{2}\Delta bT^2 - \frac{1}{6}\Delta cT^3 - \frac{1}{12}\Delta dT^4 + \frac{1}{2}\Delta e \frac{1}{T} + IT}{T} \quad (11)$$

For a ternary carbonate eutectic mixture, $\Delta_r G_e(T) = x_A \Delta_r G_A(T) + x_B \Delta_r G_B(T) + x_C \Delta_r G_C(T) + RT \ln K$; x_i is mole fraction for each component.

$$\ln K' = \frac{x_A \Delta_r G_A(T) + x_B \Delta_r G_B(T) + x_C \Delta_r G_C(T)}{-RT} \quad (12)$$

From equations 11 and 12, the relationship between equilibrium CO₂ partial pressure and temperature with a single carbonate and ternary carbonate eutectic mixture can be obtained, respectively.

Appendix B

Reaction 1



Table 1.1 Heat capacity parameters from the National Institute of Standards and Technology (NIST).

$C_p = a + bT + cT^2 + dT^3 + eT^{-2}$					
J.mol ⁻¹ k ⁻¹	Li ₂ CO ₃ (l)	Li ₂ O (s)	CO ₂ (g)	J.mol ⁻¹ k ⁻¹	Reaction 1
a	185.435	69.580	24.997	Δa	-90.857
b	-5.1×10^{-8}	1.768×10^{-2}	0.0551	Δb	0.0728
c	3×10^{-11}	0	-3.369×10^{-5}	Δc	-3.369×10^{-5}
d	-6×10^{-15}	0	7.948×10^{-9}	Δd	7.948×10^{-9}
e	3	-1.904×10^6	-136638	Δe	-2040641

Table 1.2 Thermodynamic data

kJ.mol ⁻¹	Li ₂ CO ₃	Li ₂ O	CO ₂
$\Delta_f H^0_{298}$	-1215.9	-592.9	-142.0
$\Delta_f G^0_{298}$	-1132.1	-561.2	-169.2
For reaction 1			
$\Delta_r H^0_{298} / \text{kJ.mol}^{-1}$	481.0		
$\Delta_r G^0_{298} / \text{kJ.mol}^{-1}$	401.7		

From equation 6, $\Delta H = \Delta H_0 + \Delta aT + \frac{1}{2}\Delta bT^2 + \frac{1}{3}\Delta cT^3 + \frac{1}{4}\Delta dT^4 - \Delta eT^{-1}$

The constant of integration is as follows:

$$\Delta H_0 = \Delta H - \Delta aT + \frac{1}{2}\Delta bT^2 + \frac{1}{3}\Delta cT^3 + \frac{1}{4}\Delta dT^4 - \Delta eT^{-1} \quad (6.1)$$

For reaction 1, use $\Delta_r H^0_{298}$ substitute ΔH ; then the constant $\Delta H_0 = 498273 \text{ J/mol}$.

From equation 8, the constant I can be calculated:

$$I = \frac{\Delta G - (\Delta H_0 - \Delta aT \ln T - \frac{1}{2}\Delta bT^2 - \frac{1}{6}\Delta cT^3 - \frac{1}{12}\Delta dT^4 + \frac{1}{2}\Delta e\frac{1}{T})}{T} \quad (8.1)$$

Substitute ΔH_0 with 498,273 J/mol in equation 8.1; $I = -819.83 \text{ J/mol.K}$.

Therefore, the relationship between equilibrium CO₂ partial pressure and temperature can be expressed from equation 11:

$$\ln K = \frac{\Delta G_T^\ominus}{-RT} = \frac{\Delta H_0 - \Delta aT \ln T - \frac{1}{2}\Delta bT^2 - \frac{1}{6}\Delta cT^3 - \frac{1}{12}\Delta dT^4 + \frac{1}{2}\Delta e\frac{1}{T} + IT}{-RT} =$$

$$\frac{498273.8785 + 90.857T \ln T - 0.0364T^2 + 5.615 \times 10^{-6}T^3 - 6.623 \times 10^{-10}T^4 - 1020320.5\frac{1}{T} - 820T}{-8.314T}$$

Appendix B

A scheme according to the relationship is presented in Fig. B1 below:

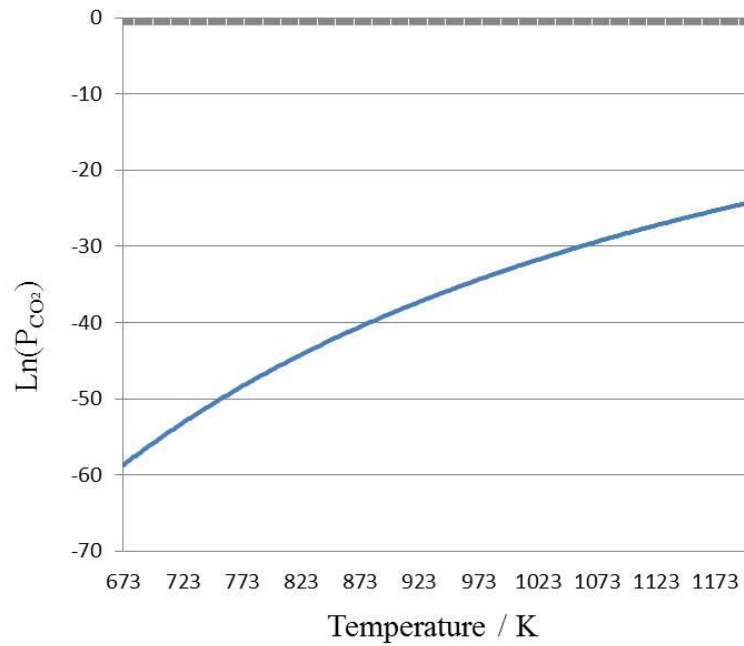


Figure B1. Equilibrium CO₂ partial pressure for Reaction 1.

Reaction 2



Table 2.1 Heat capacity parameter from the National Institute of Standards and Technology (NIST).

$C_p = a + bT + cT^2 + dT^3 + eT^{-2}$					
J.mol ⁻¹ k ⁻¹	Na ₂ CO ₃ (l)	Na ₂ O (s)	CO ₂ (g)	J.mol ⁻¹ k ⁻¹	Reaction 2
a	189.535	25.575	24.997	Δa	-138.96
b	-7×10^{-9}	0.177	0.0551	Δb	0.2328
c	2×10^{-12}	-1.663×10^{-4}	-3.369×10^{-5}	Δc	-0.0002
d	-5.205×10^{-18}	5.761×10^{-8}	7.948×10^{-9}	Δd	6.556×10^{-8}
e	-3	338149	-136638	Δe	201514

Table 2.2 Thermodynamic data.

kJ.mol ⁻¹	Na ₂ CO ₃	Na ₂ O	CO ₂
$\Delta_f H^0_{298}$	-1130.7	-414.2	-142.0
$\Delta_f G^0_{298}$	-1044.4	-375.5	-169.2
For reaction 2			
$\Delta_r H^0_{298} / \text{kJ.mol}^{-1}$	574.500		
$\Delta_r G^0_{298} / \text{kJ.mol}^{-1}$	499.700		

Equation 6.1 is solved for the constant ΔH_0 , which is 607,800 J.mol⁻¹ and substituted in equation 8.1.

Appendix B

$$I = \frac{\Delta G - \left(\Delta H_0 - \Delta a T \ln T - \frac{1}{2} \Delta b T^2 - \frac{1}{6} \Delta c T^3 - \frac{1}{12} \Delta d T^4 + \frac{1}{2} \Delta e \frac{1}{T} \right)}{T} =$$

$$\frac{499700 - \left(607800 + 138.96 \times 298 \times \ln 298 - \frac{1}{2} \times 0.2328 \times 298^2 + \frac{1}{6} \times 0.0002 \times 298^3 - \frac{1}{12} \times 6.556 \times 10^{-8} \times 298^4 + \frac{1}{2} \times 201514 \times \frac{1}{298} \right)}{298} =$$

$$-1123.937 \text{ J/mol K}$$

Therefore, the equation of CO₂ partial pressure with temperature can be expressed:

$$\ln K = \frac{\Delta G_T^\ominus}{-RT} = \frac{\Delta H_0 - \Delta a T \ln T - \frac{1}{2} \Delta b T^2 - \frac{1}{6} \Delta c T^3 - \frac{1}{12} \Delta d T^4 + \frac{1}{2} \Delta e \frac{1}{T} + IT}{-RT} =$$

$$\frac{607800 - 138.96 T \ln T - 0.1164 T^2 + 3.33 \times 10^{-5} T^3 - 5.463 \times 10^{-9} T^4 + 100757 \frac{1}{T} - 1123.937 T}{-8.314 T}$$

The schematic graph according to the above relationship is presented in Fig. B2 below:

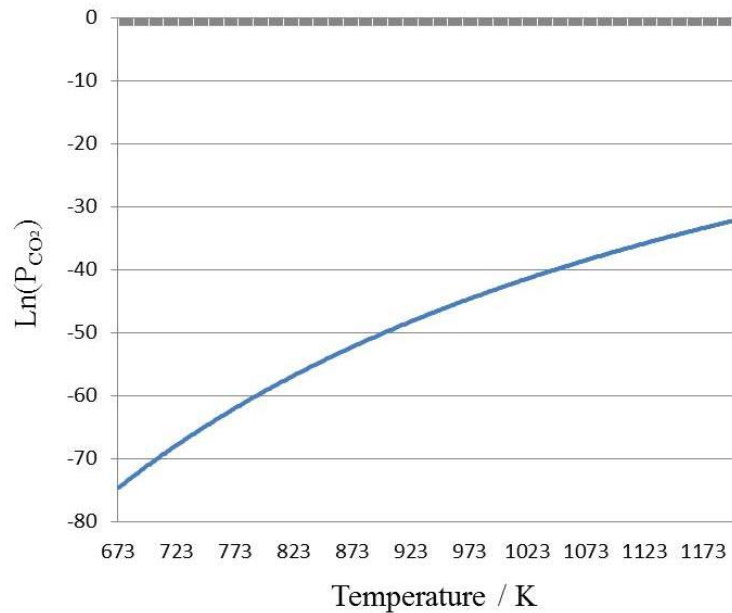


Figure B2. Equilibrium CO₂ partial pressure for Reaction 2.

Reaction 3



Table 3.1 Heat capacity parameter from the National Institute of Standards and Technology (NIST).

$C_p = a + bT + cT^2 + dT^3 + eT^{-2}$					
J.mol ⁻¹ k ⁻¹	K ₂ CO ₃ (l)	K ₂ O (s)	CO ₂ (g)	J.mol ⁻¹ k ⁻¹	Reaction 3
a	209.2	72.55	24.997	Δa	-111.65
b	-1.629×10^{-10}	0.04139	0.0551	Δb	0.09657
c	8×10^{-14}	-7.28×10^{-7}	-3.369×10^{-5}	Δc	-3.442×10^{-5}
d	-1.336×10^{-17}	2.1856×10^{-10}	7.948×10^{-9}	Δd	8.166×10^{-9}
e	-0.02105	66026	-136638	Δe	-70611.97

Appendix B

Table 3.2 Thermodynamic data

kJ.mol ⁻¹	K ₂ CO ₃	K ₂ O	CO ₂
$\Delta_f H^0_{298}$	-1151	-361.50	-142.0
$\Delta_f G^0_{298}$	-1063	-389.51	-169.2
For reaction 3			
$\Delta_r H^0_{298}$ /kJ.mol ⁻¹	647.5		
$\Delta_r G^0_{298}$ /kJ.mol ⁻¹	504.291		

$$\Delta H_0 = \Delta H - \Delta aT + \frac{1}{2}\Delta bT^2 + \frac{1}{3}\Delta cT^3 + \frac{1}{4}\Delta dT^4 - \Delta eT^{-1} = 647500 - \left(-111.65 \times 298 + 0.048285 \times 298^2 - 1.147 \times 10^{-5} \times 298^3 + 2.0415 \times 10^{-9} \times 298^4 + \frac{70611.97}{298} \right) = 676534 \text{ J.mol}^{-1}.$$

$$I = \frac{\Delta G - \left(\Delta H_0 - \Delta aT \ln T - \frac{1}{2}\Delta bT^2 - \frac{1}{6}\Delta cT^3 - \frac{1}{12}\Delta dT^4 + \frac{1}{2}\Delta e\frac{1}{T} \right)}{T} = -1199.79 \text{ J/mol K}$$

$$\ln K = \frac{\Delta G^\ominus}{-RT} = \frac{\Delta H_0 - \Delta aT \ln T - \frac{1}{2}\Delta bT^2 - \frac{1}{6}\Delta cT^3 - \frac{1}{12}\Delta dT^4 + \frac{1}{2}\Delta e\frac{1}{T} + IT}{-RT} =$$

$$\frac{676534 + 111.65T \ln T - 0.048285T^2 + 5.736 \times 10^{-6}T^3 - 6.805 \times 10^{-10}T^4 - 35305.985\frac{1}{T} - 1199.79T}{-8.314T}$$

A scheme according to the relationship is presented in Fig. B3 below:

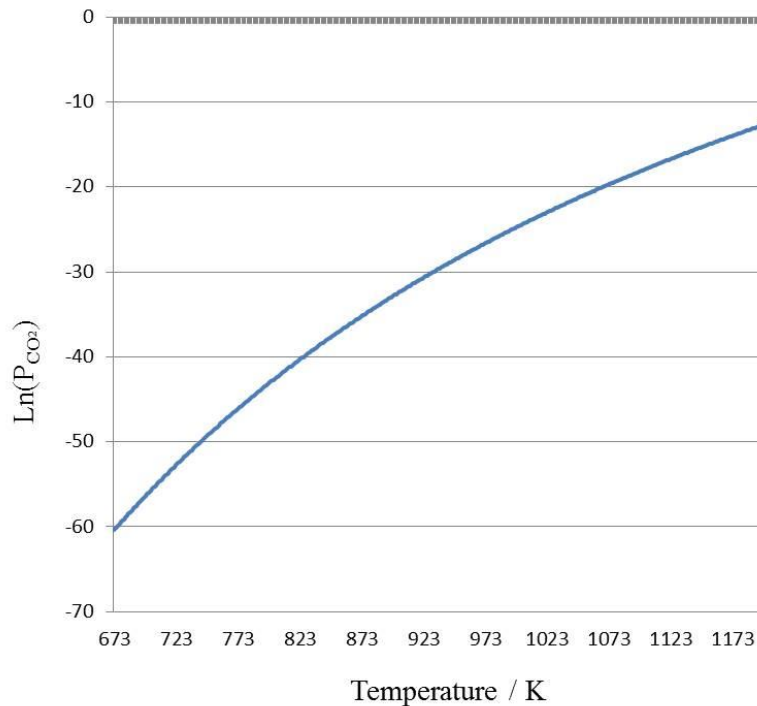


Figure B3. Equilibrium CO₂ partial pressure for Reaction 3.

Appendix B

The equilibrium line for a eutectic mixture can be expressed by equation 12 and scheme can be presented according to the ΔG for each component:

$$\ln K' = \frac{x_A \Delta_r G_A(T) + x_B \Delta_r G_B(T) + x_C \Delta_r G_C(T)}{-RT}$$

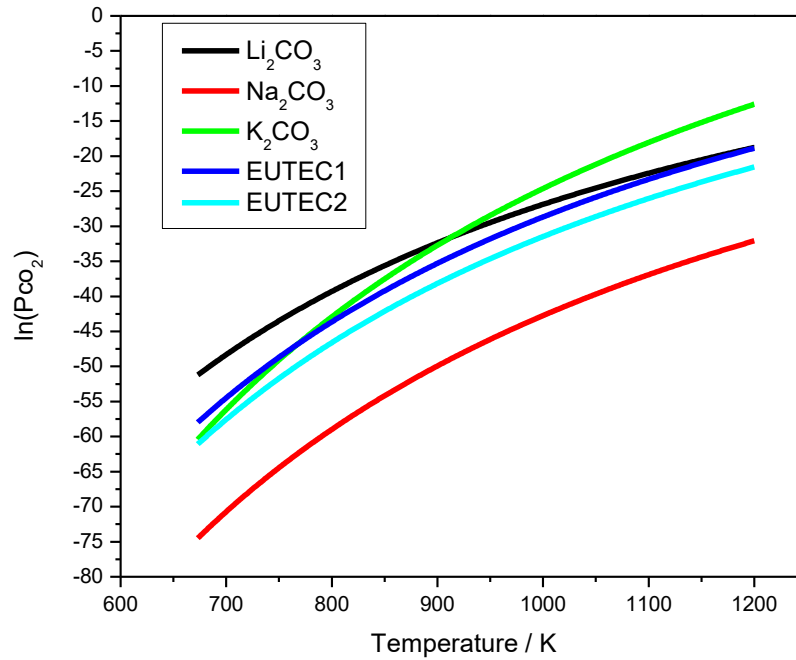


Figure B4. Equilibrium CO₂ partial pressure as a function of temperature.

Eutectic 1 is Li:Na:K = 51:16:33 mol ratio

Eutectic 2 is Li:Na:K = 42.5:32.5:25 mol ratio (Lin used [25], and MCFC use it often)

Appendix C

Appendix C

Raw data for mercury porosimetry for LSCF 6428 fabricated using cornstarch pore former

		LSCF						Porosity		0.478	
1								Mean pore diameter		667 nm	
#####								Micromeretics Autopore IV 9500 Mercury Porosimeter			
Penetrometer: 07-0023		Vol. of Pen. (ml):				6.0544					
Sample depth (m):											
Samp.Wt (g)		Samp+Pen Wt (g)		Samp+pen+Hg (g)							
1.3758		63.5051		140.0156							
Hg Density	Samp. V	Density	Gs	Porosity				* above the nearest 90% cell			
13.5438	0.405	3.395	6.000	0.434224							
	0.405	3.397		0.433839238							
Pressure (psi)	Cumulative Volume (ml/g)	Diameter (µm)	Intrusion (micron ml)	Radius (nm)	Accum. Porosity	Corrected Distribu.	mean radius (nm)	Density Distribution	Cumulative Distribution	r _{mean} nm	r ₁₀ nm
3	0.0002	72.8895	0.00027516	36444.75	0.43354469						
5	0.0002	43.7337	0.00027516	21866.85	0.43354469	0.4338392	28229.98196	0	100	733.9	
7	0.0003	31.2384	0.00041274	15619.2	0.433205224	0.4334995	18480.87399	0.002323081	99.92169992	719.5	
10	0.0003	21.8668	0.00041274	10933.4	0.433205224	0.4334995	13067.93638	0	99.92169992	719.5	
14	0.0007	15.6192	0.00096306	7809.6	0.431847361	0.4321408	9240.426432	0.009292386	99.60849961	690.5	
18	0.0007	12.1482	0.00096306	6074.1	0.431847361	0.4321408	6887.400915	0	99.60849961	690.5	
25	0.0007	8.7467	0.00096306	4373.35	0.431847361	0.4321408	5154.043581	0	99.60849961	690.5	
40	0.0009	5.4667	0.00123822	2733.35	0.43116843	0.4314614	3457.440704	0.003326156	99.45189946	685.1	*
60	0.0011	3.6445	0.00151338	1822.25	0.430489498	0.430782	2231.781136	0.003855654	99.29529931	681.6	1117.3
100	0.0038	2.1867	0.00522804	1093.35	0.421323921	0.4216102	1411.508781	0.041314532	97.18119722	651.8	1030.6
150	0.0667	1.4578	0.09176586	728.9	0.207799915	0.2079411	892.7165368	1.212575833	47.93044872	212.1	1204.1
200	0.0975	1.0933	0.1341405	546.65	0.103244441	0.1033146	631.2314829	0.836720934	23.81402497	59.9	
300	0.1115	0.7289	0.1534017	364.45	0.055719225	0.0557571	446.3480621	0.269920137	12.85201418	10.9	
400	0.1144	0.5467	0.15739152	273.35	0.045874716	0.0459059	315.6301752	0.078807217	10.58131194	3.8	
550	0.116	0.3976	0.1595928	198.8	0.040443263	0.0404707	233.1136633	0.039272215	9.32851071	0.8	
700	0.1163	0.3124	0.1600554	156.2	0.039424865	0.0394517	176.2173658	0.009723532	9.093610479	0.4	
900	0.1167	0.243	0.16055586	121.5	0.038067002	0.0380929	137.7617509	0.012445501	8.78041017	0.0	
1100	0.1167	0.1988	0.16055586	99.4	0.038067002	0.0380929	109.8958598	0	8.78041017	0.0	
1300	0.1167	0.1682	0.16055586	84.1	0.038067002	0.0380929	91.43052007	0	8.78041017	0.0	
1500	0.1167	0.1458	0.16055586	72.9	0.038067002	0.0380929	78.3	0	8.78041017	0.0	
1800	0.1167	0.1215	0.16055586	60.75	0.038067002	0.0380929	66.54829074	0	8.78041017	0.0	
2100	0.1167	0.1041	0.16055586	52.05	0.038067002	0.0380929	56.23199712	0	8.78041017	0.0	
2500	0.1167	0.0875	0.16055586	43.75	0.038067002	0.0380929	47.71988579	0	8.78041017	0.0	
2900	0.1167	0.0754	0.16055586	37.7	0.038067002	0.0380929	40.61249808	0	8.78041017	0.0	
3400	0.1167	0.0643	0.16055586	32.15	0.038067002	0.0380929	34.81458028	0	8.78041017	0.0	
3900	0.1167	0.0561	0.16055586	28.05	0.038067002	0.0380929	30.03010989	0	8.78041017	0.0	
4500	0.1167	0.0486	0.16055586	24.3	0.038067002	0.0380929	26.10775747	0	8.78041017	0.0	
5100	0.1167	0.0429	0.16055586	21.45	0.038067002	0.0380929	22.83057161	0	8.78041017	0.0	
5800	0.1167	0.0377	0.16055586	18.85	0.038067002	0.0380929	20.10802079	0	8.78041017	0.0	
6500	0.1167	0.0336	0.16055586	16.8	0.038067002	0.0380929	17.79550505	0	8.78041017	0.0	
7300	0.1167	0.03	0.16055586	15	0.038067002	0.0380929	15.87450787	0	8.78041017	0.0	
8100	0.1167	0.027	0.16055586	13.5	0.038067002	0.0380929	14.23024947	0	8.78041017	0.0	
9000	0.1167	0.0243	0.16055586	12.15	0.038067002	0.0380929	12.80722452	0	8.78041017	0.0	
9900	0.1167	0.0221	0.16055586	11.05	0.038067002	0.0380929	11.58695387	0	8.78041017	0.0	
10900	0.1167	0.0201	0.16055586	10.05	0.038067002	0.0380929	10.538145	0	8.78041017	0.0	
11900	0.1167	0.0184	0.16055586	9.2	0.038067002	0.0380929	9.615612305	0	8.78041017	0.0	
13000	0.1167	0.0168	0.16055586	8.4	0.038067002	0.0380929	8.79090439	0	8.78041017	0.0	
14000	0.1167	0.0156	0.16055586	7.8	0.038067002	0.0380929	8.094442538	0	8.78041017	0.0	
15000	0.1167	0.0146	0.16055586	7.3	0.038067002	0.0380929	7.545859792	0	8.78041017	0.0	
16000	0.1167	0.0137	0.16055586	6.85	0.038067002	0.0380929	7.071421356	0	8.78041017	0.0	
17000	0.1167	0.0129	0.16055586	6.45	0.038067002	0.0380929	6.646991801	0	8.78041017	0.0	
18000	0.1167	0.0121	0.16055586	6.05	0.038067002	0.0380929	6.24679918	0	8.78041017	0.0	
19000	0.1167	0.0115	0.16055586	5.75	0.038067002	0.0380929	5.898092912	0	8.78041017	0.0	
20000	0.1167	0.0109	0.16055586	5.45	0.038067002	0.0380929	5.597990711	0	8.78041017	0.0	
21000	0.1167	0.0104	0.16055586	5.2	0.038067002	0.0380929	5.323532662	0	8.78041017	0.0	
22000	0.1167	0.0099	0.16055586	4.95	0.038067002	0.0380929	5.073460358	0	8.78041017	0.0	
23200	0.1167	0.0094	0.16055586	4.7	0.038067002	0.0380929	4.823380557	0	8.78041017	0.0	
24500	0.1167	0.0089	0.16055586	4.45	0.038067002	0.0380929	4.573292031	0	8.78041017	0.0	
26000	0.1167	0.0084	0.16055586	4.2	0.038067002	0.0380929	4.323193264	0	8.78041017	0.0	
27500	0.1167	0.008	0.16055586	4	0.038067002	0.0380929	4.098780306	0	8.78041017	0.0	
29000	0.1167	0.0075	0.16055586	3.75	0.038067002	0.0380929	3.872983346	0	8.78041017	0.0	
30500	0.1167	0.0072	0.16055586	3.6	0.038067002	0.0380929	3.674234614	0	8.78041017	0.0	
33000	0.1167	0.0066	0.16055586	3.3	0.038067002	0.0380929	3.446737588	0	8.78041017	0.0	
34500	0.1167	0.0063	0.16055586	3.15	0.038067002	0.0380929	3.224127789	0	8.78041017	0.0	
36000	0.1167	0.0061	0.16055586	3.05	0.038067002	0.0380929	3.099596748	0	8.78041017	0.0	
37500	0.1167	0.0058	0.16055586	2.9	0.038067002	0.0380929	2.974054472	0	8.78041017	0.0	
39000	0.1167	0.0056	0.16055586	2.8	0.038067002	0.0380929	2.84956137	0	8.78041017	0.0	